2012

Variations in pore water salinities above and below allochthonous salt sheets in the deepwater Gulf of Mexico: implications for mechanisms of solute transport

Miles Alexander McCammon
Louisiana State University and Agricultural and Mechanical College

VARIATIONS IN PORE WATER SALINITIES ABOVE AND BELOW ALLOCHTHONOUS SALT SHEETS IN THE DEEPWATER GULF OF MEXICO: IMPLICATIONS FOR MECHANISMS OF SOLUTE TRANSPORT

A Thesis

Submitted to the Graduate Faculty of the
Louisiana State University and
Agricultural and Mechanical College
in partial fulfillment of the
requirements for the degree of
Master of Science

In

The Department of Geology and Geophysics

by

Miles Alexander McCammon
B.S., University of California, Los Angeles, 2008
May, 2012

ACKNOWLEDGEMENTS

I would like to thank my adviser, Dr. Jeffrey S. Hanor, for his invaluable advice and direction, and my other two committee members, Dr. Carol M. Wicks and Dr. Jeffrey A. Nunn, for their guidance throughout this project. I would also like to thank R. Hampton Peele, of the Louisiana Geological Survey, who helped with properly locating my wells. I would like acknowledge the Minerals Management Service (MMS), now the Bureau of Ocean Energy Management (BOEM) NSF Grant ERA-0557555 (Hanor and Nunn) and Louisiana State University, for partial funding of this research.

I would like to thank my parents, James A. and Joan W. McCammon, and my grandparents, Col. (ret.) Joseph R. McCammon and the late Herbert F. Weinstock, for their support which made this thesis possible. Finally, I would like to thank my fellow graduate students for their support, suggestions, and help.

TABLE OF CONTENTS

ABSTRACT

Spatial variations in salinity of pore waters in marine sediments provide useful information on processes and rates of subseafloor fluid flow and solute transport, particularly if there are evaporites in the section. Pore water salinities were determined for 18 drill holes which penetrated allochthonous salt bodies in 12 widely-scattered protraction blocks on the Louisiana offshore continental shelf and slope. Salinities were calculated from Log ASCII Standard-Logging While Drilling (LAS-LWD) logs using the Revil *et al.* (1998) dual-conductivity technique. The sites represent a wide range of field settings. Water depths range from 30 to 1990 m, depths to the top of salt from the seafloor range from 440 to 5200 m, and salt thicknesses range from 70 to 2000 m. Sediment ages above and below salt and approximate sedimentation rates were determined from Bureau of Ocean Energy Management (BOEM) paleontological data and range from Miocene to Recent. Sites in eight blocks have concave downward salinity profiles above salt, consistent with transient molecular diffusive transport with possible compaction-driven flow. The salinity profiles were modeled using two scenarios: 1) salt was emplaced at its present depth, and molecular diffusion upward from the top of salt has been the sole solute transport mechanism; 2) salt was emplaced near the seafloor, and there has been progressive burial of salt with compaction-driven advective flow upward since. The time required by molecular diffusion alone tends to exceed the age of the sediments. A better fit in space and time is obtained on the assumption that sediment compaction is also a driving force. Salinities in two blocks increase upward, possibly reflecting lateral flow of brines from shallower salt. Salinities in the two remaining blocks are elevated but constant for distances of 500 to 1000 m above salt and may reflect ponding of brines derived from shallower salt. At sites where there is subsalt information, the salinity profiles are generally convex upward, reflecting probable

diffusional transport downward. The results are consistent with an earlier LSU study which concluded that dominant mechanisms of vertical solute transport in deepwater Gulf of Mexico sediments include diffusion and compaction-driven advection.

1. INTRODUCTION

1.1. Nature of the Scientific Problem

Spatial variations in the salinity of pore waters in sedimentary basins can provide important insight into hydrogeologic processes ranging from local to basin-wide scales (e.g., Connolly *et al.,* 1990; Roberts and Nunn, 1995; Bruno and Hanor, 2003; Hanor *et al.,* 2004; McIntosh and Walter, 2005; Person *et al.*, 2007). Hanor and Mercer (2010) conducted a study of spatial variations in pore water salinities in sediments in an approximately 500-km by 200-km area of the northern deep water (water depth >500 m) Gulf of Mexico (GOM) sedimentary basin to provide insight into pathways and mechanisms of solute transport in this portion of the basin. A second objective of their study was to document salinities in the upper 500 m of the sedimentary section, the approximate depth to which methane hydrate, a potential future energy resource, may be stable. Elevated salinities would reduce the P-T stability range of hydrates. Hanor and Mercer (2010) found that even though much of the northern Gulf of Mexico is underlain by allochthonous salt, and numerous seafloor brine seeps, often associated with chemosynthetic communities (e.g. Roberts *et al.,* 2010; MacDonald, 2002), have been documented, most of the undisturbed portion of the shallow sedimentary section has not been regionally permeated by hypersaline waters. Waters with elevated salinity appear to be limited to areas near seafloor brine seeps or seafloor salt exposures, such as the Orca basin (e.g. Addy and Behrens, 1980; Plicher and Blumstein, 2007). Most of the sedimentary section, at least in the boreholes studied, is characterized by pore waters having apparently normal seawater salinities (ca. 35 g/L) to moderately elevated seawater salinities (< 60 g/L) to a subseafloor depth of approximately 1 km. Hypersaline waters having salinities in excess of 100 g/L become more

common at subseafloor depths of 2 km. Hanor and Mercer found that a characteristic feature of the deep water sediments is a progressive increase in salinity with depth.

1.2. Present Study

Many of the salinity-depth profiles generated in the Hanor and Mercer (2010) study have a concave-downward trend in salinity increasing toward the top of salt, similar to salinity profiles in post-Miocene sediments in Messenian evaporite basins of the Mediterranean Sea, although over greater depth intervals (McDuff and Gieskes 1976). The Mediterranean profiles have been shown by McDuff and Gieskes to reflect upward solute transport dominated by molecular diffusion and compaction-driven advection. Theoretical calculations done by Ranganathan and Hanor (1987) to try to explain salinity variations with depth in sediments overlying the Jurassic Louann Salt in the northern Gulf of Mexico rim in southern Arkansas, using a combination of diffusion and compaction produced similar concave-downward trends in salinity with depth. However, the actual salinity profiles they observed in the field were linear.

Wilson and Ruppel (2007) published the results of a numerical modeling study of subseafloor fluid convection driven by spatial variations in temperature and salinity in deep water GOM sediments. The physical framework of their model is based on an E-W seismic line across Garden Banks block 425, which is immediately west of the Auger field. In their model, a 1.5 to 2.0 km thick sedimentary sequence overlies a tabular salt structure which has a subsurface high which corresponds in position to a seafloor mound. Wilson and Ruppel chose a baseline sediment intrinsic permeability, k, of 10^{-15} m^2, equivalent to one millidarcy, in their modeling study. A number of simulations were performed, including increasing and decreasing the baseline k by an order of magnitude and by including fault zones of high permeability. Where salt is not present, the highest flow rates obtained with a k of 10^{-15} m^2 were on the order of 1 mm/y with

flow driven by thermal overturn. The addition of salt and salt dissolution produced flow rates up to 2 mm/y. Increasing and decreasing *k* by an order of magnitude increased and decreased flow rates by approximately an order of magnitude.

Sarkar *et al.* (1995) modeled the possible thermohaline convection of formation waters driven by the dissolution of salt at the base of allochthonous salt sheets in the GOM, and found that the nature of the solute transport was time dependent, with salt dissolution by molecular diffusion occurring for the first four million years until Rayleigh-Bernard instabilities cause downwelling high-salinity plumes to develop. Hanor and Mercer (2010) suggested that detailed kilometer-scale studies of the salinity fields around salt would help to better define transport processes at and away from the sediment-salt interface and the origin of high salinities in GOM sediments.

The purpose of the research presented here was to document spatial variations in salinity in close proximity to salt. The Hanor and Mercer (2010) study relied on calculating salinity from data obtained from images of borehole log responses. None of the Hanor and Mercer boreholes penetrated salt, and they were not able to find a general relation between the salinity of pore waters at a given depth below the seafloor and the distance to the top of salt. If some systematic relation exists, it would have aided in hydrate stability predictions. The salinity calculations made here have utilized continuous digital LAS-LWD (logging while drilling) logs from boreholes that penetrated salt. The basic hypotheses tested in this research were that spatial variations in salinity can be used to better constrain the interpretation of mechanisms and rates of fluid flow and solute transport in GOM sediments, constrain the timing of salt emplacement of salt, and determine if there were systematic variations between the salinity of pore waters at a given depth below the seafloor and the distance to the top of salt.

2. FIELD SETTING

2.1. Plate Tectonic Origin of the Gulf of Mexico Sedimentary Basin

The Louann salt of the northern Gulf of Mexico and the related Campeche salt of the Yucatán formed when the paleo-Pacific Ocean embayment crossed Mexico and reached the spreading margin in the late Bathonian and Callovian (164.7-161.2 Ma). Salt was deposited in shallow slowly subsiding basins on either side of the topographically high spreading center, with probable intermittent recharge from the west (Salvador, 1987).

After the Callovian (161.2 Ma), the basin deepened due to cooling of the oceanic crust and sediment loading. Gulf of Mexico rifting ended in the early Cretaceous (140-135Ma), with post-rifting tectonics primarily controlled by salt movement. The Gulf of Mexico likely became connected to the Atlantic Ocean in the late Jurassic or early Cretaceous.

Cenozoic structural style varies in the northern Gulf of Mexico tectono-stratigraphic provinces (Fig. 2.1; Diegel et al., 1995) describes the local structural behavior. Sites in this study are in the Plio-Pleistocene detachment province, and Tabular Salt / Mini Basin province.

2.2. Sediment Deposition and Salt Tectonics

Sediment deposition in the northern Gulf of Mexico is related to uplift of various parts of the Laurentian craton, with early deposition primarily located in the western Gulf (Galloway *et al.*, 2000). Northern Gulf of Mexico sedimentation drastically increased during the Pliocene in response to uplift of the Great Plains and Rocky Mountains and following Plio-Pleistocene glaciation (Harrison and Summa, 1991). Harrison and Summa (1991) invoked this sedimentation as a mechanism for squeezing salt seaward as well as an explanation for current Gulf of Mexico

geopressuring. The change in the position of the sediment depocenters is tracked by isopach thicknesses (Fig. 2.2) from Feng and Buffler (1996).

Maximum average sedimentation rates in the field area from the Feng and Buffler (1996) isopach maps were calculated by dividing the sediment thickness by the amount of time for the associated geologic Epoch (Fig. 2.2; Witrock *et al*., 2003). Average sedimentation rates in the depocenters increased from 190 m/My in the Paleocene and Eocene to 610 m/My in Oligocene, then decreased to 320 m/My in the Miocene, and increased to 1270 m/My in the Pliocene and to 1690 m/My for the Pleistocene.

Previous authors such as Hudec and Jackson (2006) have proposed several general models for salt sheet formation. Each of these models has different implications for relations between salt bodies and the surrounding sediments, resulting in two end-member models: extrusive advance, and salt-wing intrusion (Fig. 2.4).

The salt glacier or extrusive advance model describes the advance of a salt glacier at or near the ocean bottom until late-stage deposition. Ranganathan and Hanor (1987) modeled salinities resulting from varying rates of sediment deposition and compaction above a flat-lying and subsiding NaCl evaporite. The Ranganathan and Hanor (1987) model is similar to shallow emplacement of salt followed by subsidence from Plio-Pleistocene sedimentation.

The salt-wing intrusion or intrusive model describes emplacement of salt into preexisting sediment layers, with minimal deposition and compaction above. If this intrusion occurred rapidly, dissolution of salt would create a plane of salinity at the salt-sediment interface which would then diffuse into the sediments. General numerical solutions for diffusion away from a plane of constant solution have been found by Ogata (1970) and Crank (1975).

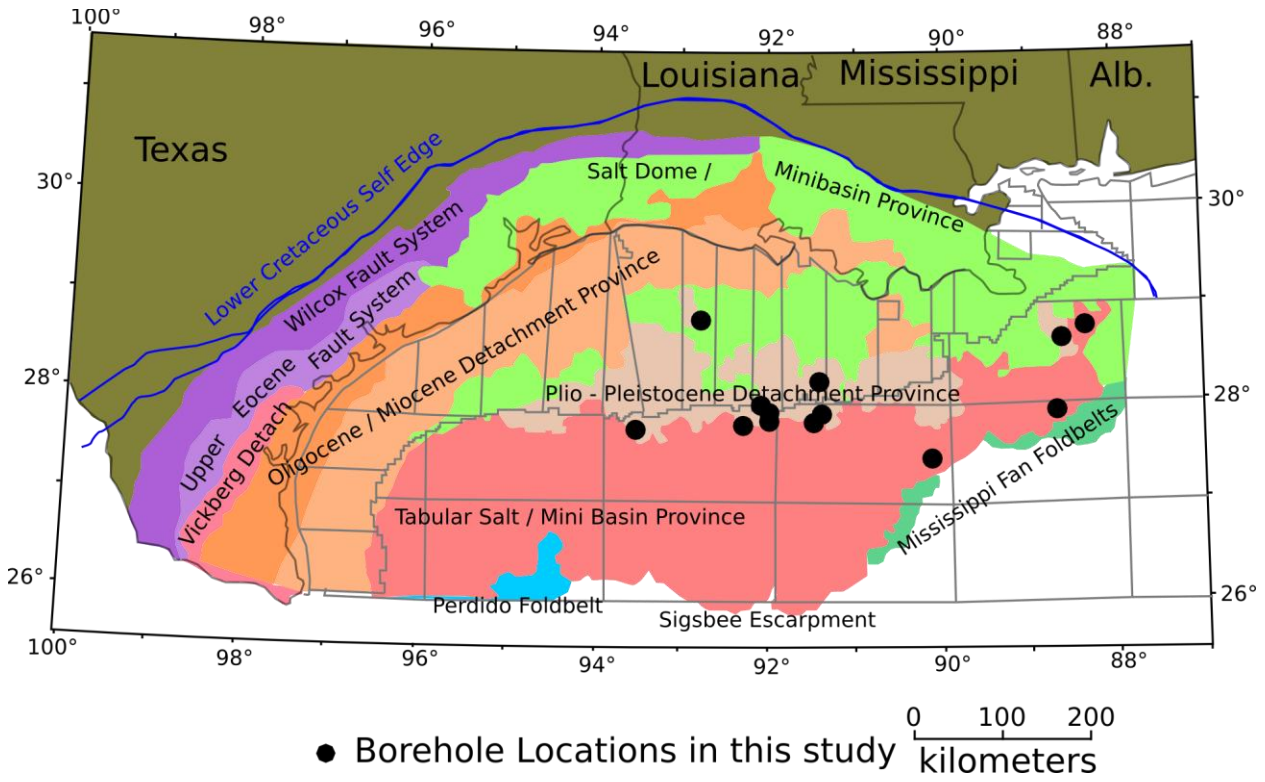

Figure 2.1. Map of tectono-stratigraphic provinces of the northern Gulf of Mexico basin after Diegel *et al.* (1995). Locations of boreholes in this study are shown, and are in the Plio-Pleistocene and Tabular Salt / Mini Basin Provinces.

Figure 2.2. Isopach maps in meters for the field area adopted from Feng and Buffler (1996) showing thickness of different aged sediments in the field area. Maps from upper left: Pleistocene (P_s), Pliocene (P_o), Miocene (M_I), Oligocene (O_G), Eocene (Eo), Paleocene (Pε), Upper Cretaceous (K). Dashed lines indicate conjecture in the original paper, and dots represent sites in this study. Protraction areas: AT – Atwater Valley; EC – East Cameron; EI – Eugene Island; GB – Garden Banks; GC – Green Canyon; MC – Mississippi Canyon; SM – South Marsh Island.

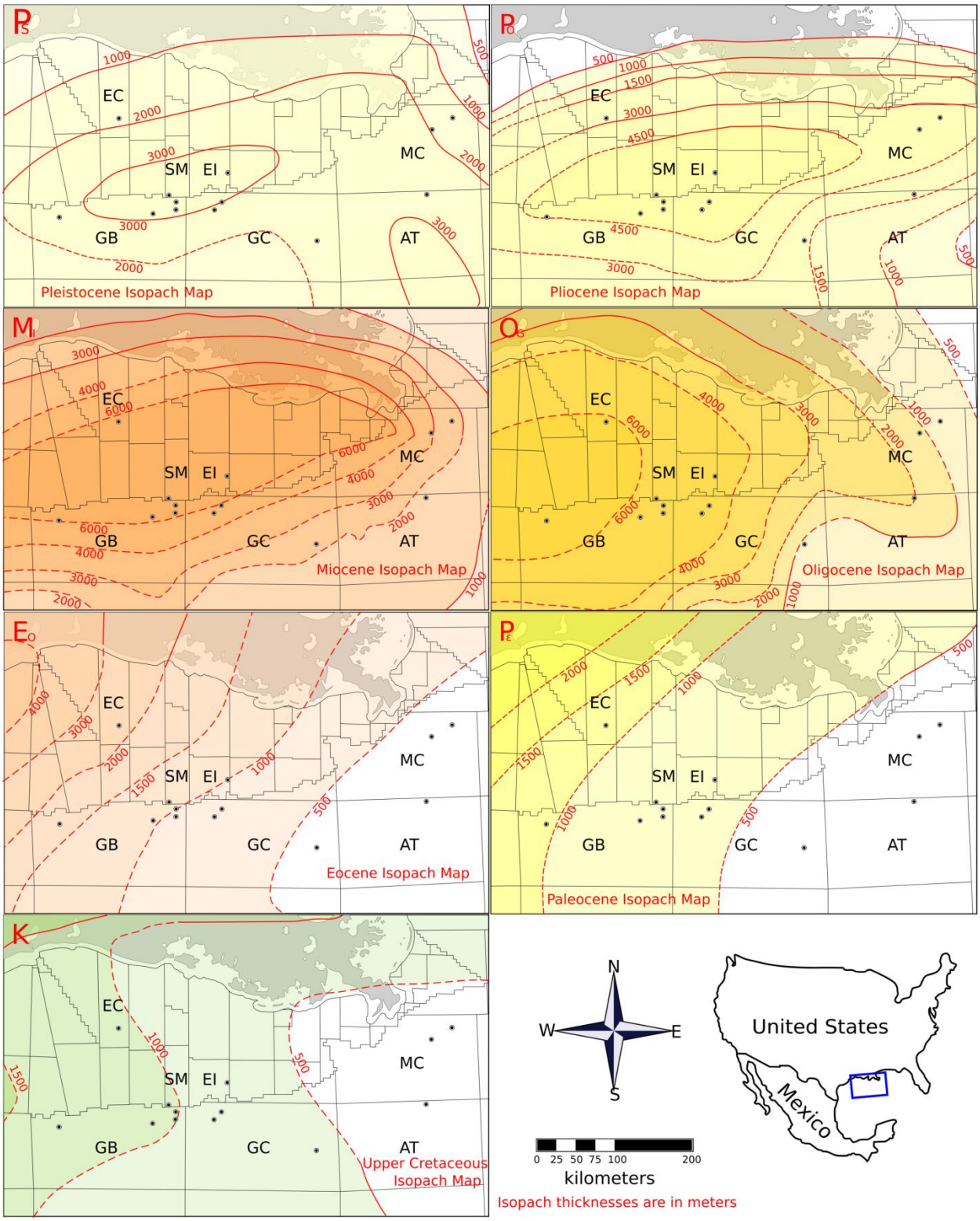
Pleistocene Isopach Map
Pliocene Isopach Map
Miocene Isopach Map
Oligocene Isopach Map
Eocene Isopach Map
Paleocene Isopach Map
Upper Cretaceous Isopach Map
EC
SM
EI
MC
GB
GC
AT
N
W
E
S
United States
Mexico
0 25 50 75 100 200
kilometers
Isopach thicknesses are in meters

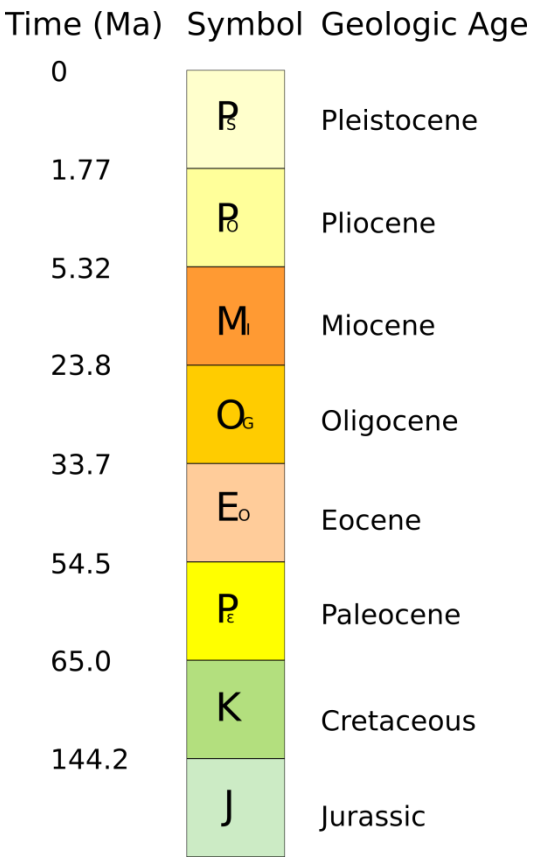

Figure 2.3. Colors and symbols used in displaying the age of sediments. Ages, in millions of years, are after Witrock *et al.* (2003). Symbols are from Soller *et al.* (2000).

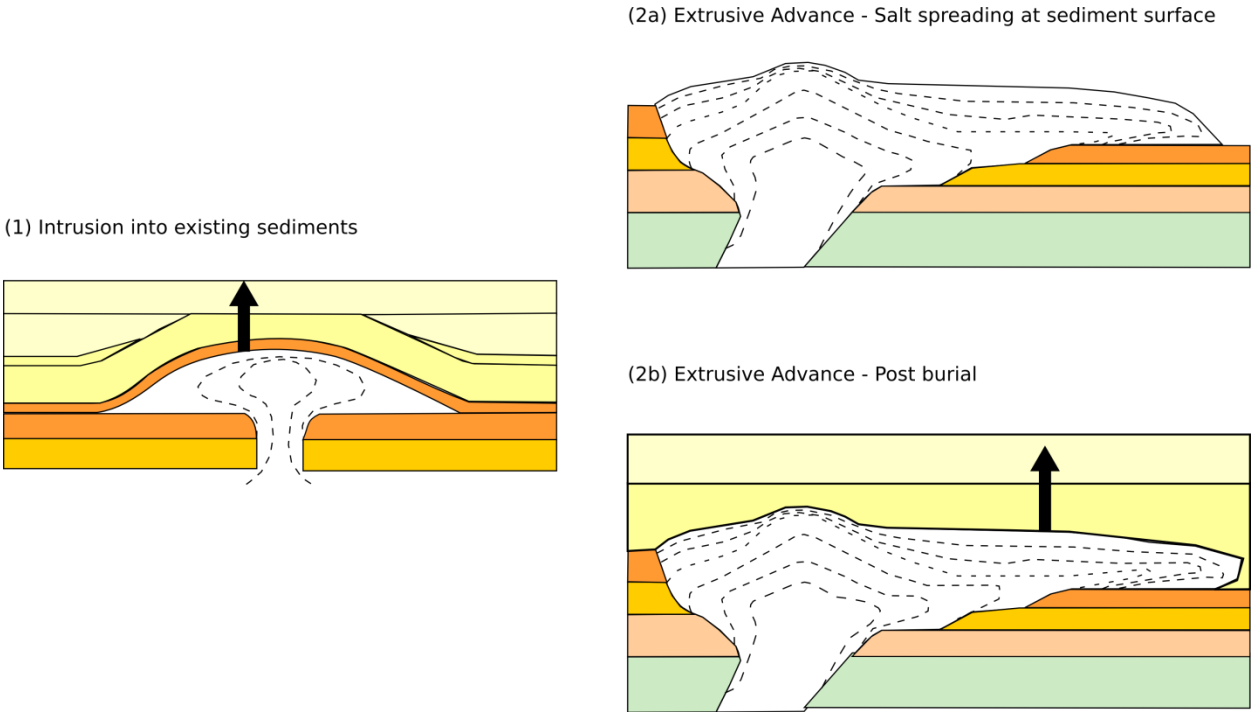

Figure 2.4. End member conceptual models of salt sheet emplacement simplified and modified to show modern salinities from Hudec and Jackson (2006) showing (1) salt wing emplacement and (2) salt glacier model. (1) Salt was intruded into present sediments, followed by solute transport by simple molecular diffusion. (2a) Salt spread at or near the seafloor followed by (2b) sedimentation and solute transport by sediment compaction and diffusion. Black arrows indicate solute transport though the pore waters. Figure 2.5 shows an intermediate model between the two end members.

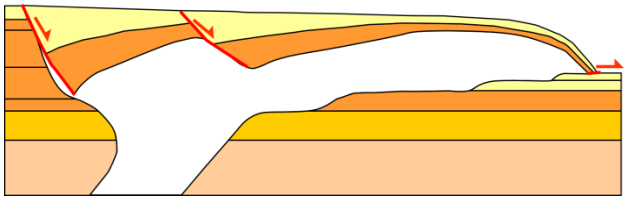

Figure 2.5. Intermediate model of salt emplacement from Hudec and Jackson (2006) showing older sediments thrust above younger sediments with salt in the middle. Faults and slip directions are indicated in red.

3. METHODS AND SOURCES OF DATA

3.1. Introduction

There were three main parts to this project: 1) estimating salinities above and below salt bodies for a series of sites in the central Gulf of Mexico, 2) interpreting possible spatial variations in salinity in terms of the timing and mechanisms of fluid flow and solute transport above and below salt, and 3) determining if there is a relation between salinity at a given depth and distance to the top of salt.

3.2. Drill Holes Studied

Pore water salinities were determined from logs for 18 drill holes which penetrated allochthonous salt bodies in 12 widely-scattered protraction blocks on the Louisiana offshore continental shelf and slope (Fig. 3.1). Logs were in Log ASCII Standard (LAS) format, and recorded using the logging while drilling (LWD) technique. Salinities were calculated from logs using the Revil *et al.* (1998) dual-conductivity techniques described below. The sites represent a wide range of field settings. Water depths range from 30 to 1990 m, depths to the top of salt from the seafloor range from 440 to 5200 m, and salt thicknesses range from 70 to 2000 m (Table 3.1).

3.3. Sediment Ages

Sediment ages were used for evaluation of the diffusion modeling and as an input parameter to the Basin2 modeling, both described below. Three data sets were used to determine sediment ages for each of the sites: Bureau of Ocean Energy Management (BOEM) paleodata, National Oceanic Service (NOS) bathymetric maps (Table 3.2), and sediment isopach maps for the Gulf of Mexico from Feng and Buffler (1996). These sediment ages were also used to

calculate sedimentation rates for use in the Basin2 modeling described below and for comparison with the Ranganathan and Hanor (1987) subsiding basin salinity model.

The BOEM paleodata used in this study is publicly released paleontologic summary reports from January 1947 to May 2011 in the Gulf of Mexico. These summary reports list the shallowest depth at which a foraminiferal planktonic, benthic, or calcareous nannoplanktonic index fossil is found. These fossils are associated with geological Stages, and the boundary between two geological Stages was converted into an age in millions of years using the chart of Witrock *et al.* (2003). For this study, the Gelasian stage is interpreted as Pliocene although the IUGS Executive committee has since voted it Pleistocene (Riccardi, 2009). The BOEM reports generally include an additional depth, which is corrected for well deviation. However since the well logs were not corrected for well deviation, the uncorrected depths were used in this study (Fig. 3.2).

The BOEM data set had biostratigraphic data for 12 of the 19 boreholes in this study. To include boreholes with no biostratigraphic data, and better understand boreholes with limited biostratigraphic data, all BOEM paleodata from within each block and the eight immediately surrounding blocks (approximately a 15 km by 15 km area) were compiled. NOS bathymetric maps for each block in this study (Table 3.2) were consulted to verify if there was seafloor relief indicative of the presence of salt domes. Well locations from the well log header file, as well as protraction area definitions (Table 3.3) were used along with the Corpscon coordinate conversion program, version 6.0, (US Army Corps of Engineers, 2004) to plot locations of wells (Appendix C).

Sediment thicknesses for each geologic stage were calculated using the differences between the depths of each geologic stage. To calculate the sedimentation rates, the sediment

thicknesses were divided by the length of time in the associated geological stage. Since these thicknesses are compacted modern sediment, rather than the uncompacted sediments during deposition, these rates are lower bounds on the true sedimentation rates.

These sediment rates and thicknesses were compared against the isopach maps of the Gulf of Mexico (Fig. 2.2) from Feng and Buffler (1996). For each site, sediment thicknesses were linearly interpolated between the isopach lines to calculate approximate thicknesses. These thicknesses were combined with the water depth, to get the approximate age with depth at each site.

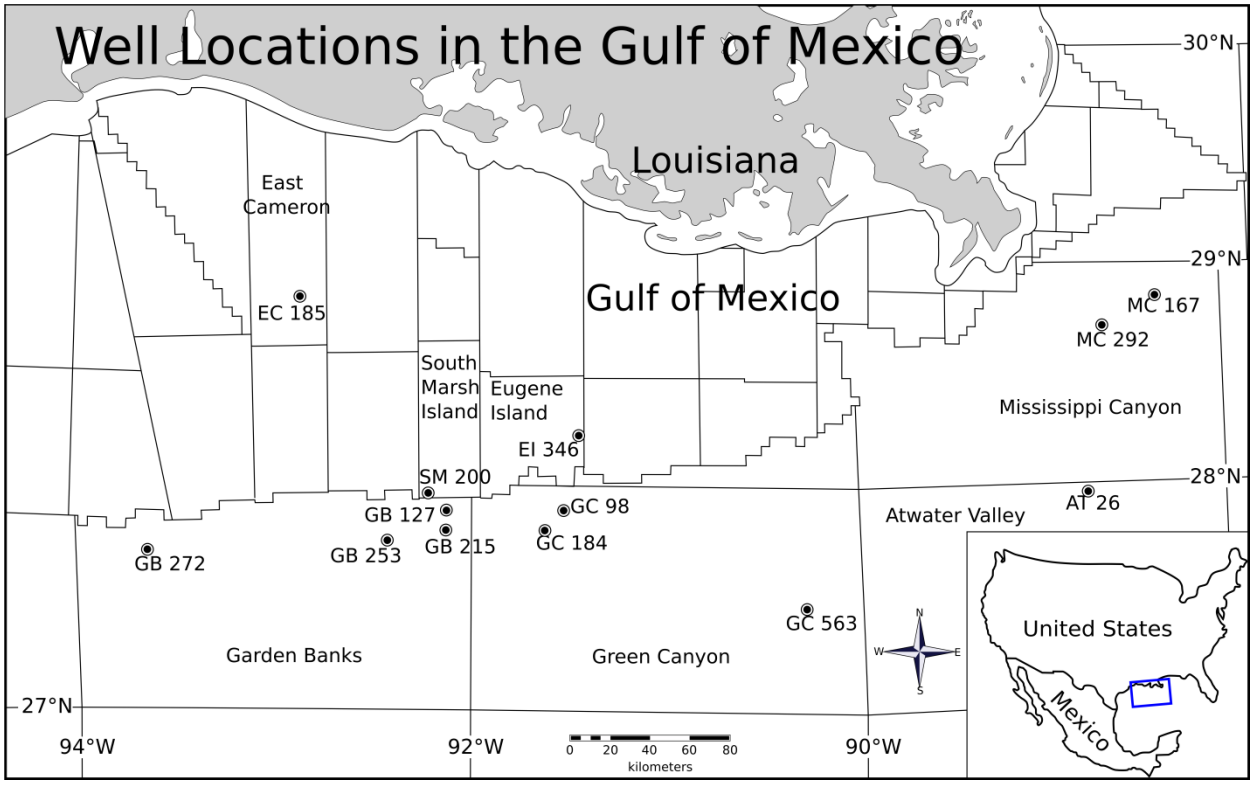

Figure 3.1. Well locations for all of the 19 wells in the central Gulf of Mexico, south of the Louisiana coast. Locations are labeled by the protraction area and the block number within the protraction area .Wells are identified using the block number and two-character protraction area identifier: AT (Atwater Valley), EC (East Cameron), EI (Eugene Island), GB (Garden Banks), GC (Green Canyon), MC (Mississippi Canyon), and SM (South Marsh Island). The following blocks have multiple wells: GB 215, GB 272, GC 98, GC 563, and MC 292.

Table 3.1. Summary of drill holes in this study. A more complete listing is in Appendix C. When multiple layers of salt were present (e.g. GC563-1), only the top layer is listed here. Block numbers listed here are the ones provided by the header file. Occasionally the borehole coordinates from the header file lay just outside of the specified protraction block. Additionally, using the API numbers, the paleontological data set also provided protraction block numbers, which sometimes were adjacent to the header file protraction blocks.

API	Protraction Area	Block	Borehole Location	Water depth (m)	Salt Depth from Seafloor (m)	Salt Thickness (m)
608184001100	Atwater Valley	26	27°57′57.2″N 88°40′41.1″W	1983	1035	455
177034091300	East Cameron	185	28°50′1.2″N 92°43′14.1″W	28	174	174
177104159200	Eugene Island	346		147.8	2972	
608074170200	Garden Banks	127	27°52′31.1″N 91°59′11.6″W	90	3820	438
608074020100	Garden Banks	215	27°47′34.2″N 92°1′56.7″W	446	5182	402
608074020101	Garden Banks	215	27°47′34.0″N 92°1′56.7″W	446	5182	418
608074022502	Garden Banks	253	27°42′56.8″N 92°18′9.9″W	564	4511	571
608074065600	Garden Banks	272	27°41′4.1″N 93°32′9.5″W	170	608	
608074065601	Garden Banks	272		170	604	2194
608115001500	Green Canyon	98		260	2090	
608115001501	Green Canyon	98		260	2900	421
608115006200	Green Canyon	184		536	1876	71
608114024900	Green Canyon	563	27°25′14.0″N 90°13′18.8″W	1263	4379	41
608114024901	Green Canyon	563	27°25′14.4″N 90°13′18.8″W	1263	4922	472
608114024902	Green Canyon	563	27°25′14.5″N 90°13′18.8″W	1263	4866	
608174056900	Mississippi Canyon	167	28°47′42.4″N 88°13′53.5″W	1328	440	1152
608174083200	Mississippi Canyon	292	28°42′12.6″N 88°35′44.2″W	1060	1032	924
608174083201	Mississippi Canyon	292		1060		
177084064600	South Marsh Island (Southern Addition)	200		145	2525	441

Table 3.2. Table listing National Ocean Service (NOS) bathymetric maps by protraction area used in this study.

Abbreviation	Protraction Area	Report Number	Year
AT	Atwater Valley	NG16-01	1983
EC	East Cameron	NH15-11	1978
EI	Eugene Island	NH15-12	1978
GB and SM	Garden Banks and South Marsh Island	NG15-02	1975
GC	Green Canyon	NG15-03	1975
MC	Mississippi Canyon	NH16-10	1975

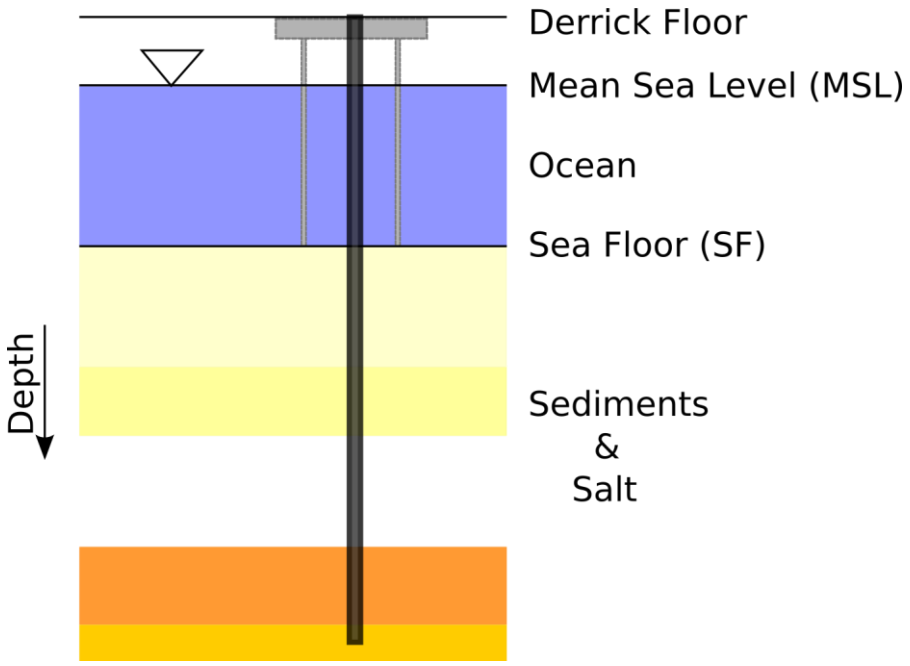

Figure 3.2. This is a schematic image showing relationship between logged depth (black), mean sea level (MSL, 0 m for this study), and the depth of the seafloor. Porosity and temperature relationships are calculated as depth below the seafloor. Borehole deviation was assumed to be minor, so logged distances were assumed to be depths.

Table 3.3. List of coordinate systems used in this study. All protraction area diagrams are described in feet not meters.

Abbreviation	Protraction Area	Coordinate System
AT	Atwater Valley	UTM zone 16N
EC	East Cameron	Louisiana (Lambert) State Coordinate System, South
EI	Eugene Island	Louisiana (Lambert) State Coordinate System, South
GB	Garden Banks	UTM zone 15N
GC	Green Canyon	UTM zone 15N
MC	Mississippi Canyon	UTM zone 16N
SM	South Marsh Island	Louisiana (Lambert) State Coordinate System, South

3.4. Revil Method Salinities

The Revil *et al.* (1998) dual-conductivity salinity technique was used to calculate salinities from the LAS-LWD logs. The technique partitions bulk electrical conductivity, as determined from the resistivity log, between charged species absorbed on clay mineral surfaces and charged species in aqueous solution. The resultant calculated conductivity of the charged species in solution is converted to salinity. The calculations are described in detail in Appendix A, and the possible sources of error are described in detail in Appendix B.

Some of the wells in this study had multiple tools logging similar information, such as the array resistivity tool. When this occurred, two criteria were used to select which tools to use when making salinity calculations: 1) the length of sedimentary section the tool recorded, and 2) the depth of lateral tool penetration into the formation. For example, when resistivity was logged using an array resistivity tool, the deep (or 90”) spacing resistivity log was preferentially used over the shallow (or 10”) spacing resistivity log, to minimize the effects of drilling fluid intrusion on the bulk formation resistivity.

Temperature and porosity values were derived from relations for depth from the seafloor (Fig. 3.2) established by other workers (Revil *et al.*, 1998; Hanor and Mumphrey, 2008; Hanor and Mercer, 2010). Neither neutron porosity nor density porosity logs provided adequate coverage, so porosity (φ) was calculated using an empirical fit to the Rubey and Hubbert (1957) equation:

$$\varphi = \varphi_0 \exp(-bZ_e) \tag{3.1}$$

Where φ_0 is the porosity at deposition, b is an empirical parameter, and Z_e is the effective depth from sea floor in meters, which is calculated from the actual depth from sea floor in meters (Z). Using the Integrated Oceanic Drilling Program hole U1324 for deep water GOM sediments Hanor and Mercer (2010) found the following relationship:

$$\varphi = 0.29 \times \exp(-0.0018 \times Z) + 0.295 \tag{3.2}$$

Some temperature logs and bottom-hole temperatures were included in the present data set, but, because these logs were recorded while drilling, temperatures were perturbed by circulating drilling fluids. Temperature at depth was calculated from depth-temperature relationships found by Hanor and Mumphry (2008) from equilibrated and bottom-hole temperatures, which vary by the protraction area (Table 3.4)**.**

The formation cation exchange capacity (CEC_{fmt}) was calculated from the gamma ray log (γ_{log}) following the Revil Method. The gamma ray log is converted to a ratio between gamma ray values corresponding to pure shale (γ_{sh}), and pure sand (γ_{ss}), with both of these values selected on a per-borehole basis. Using the mineral composition of the shale and sand end-members, cation exchange capacities for pure shale (CEC_{sh}) and pure sand (CEC_{ss}) are calculated, and then,

assuming that the gamma ray ratio is a linear function of the clay content, the CEC_{fmt} is calculated:

$$CEC_{fmt} = CEC_{ss} + \left(\frac{\gamma_{log} - \gamma_{ss}}{\gamma_{sh} - \gamma_{ss}}\right)(CEC_{sh} - CEC_{ss}) \quad (3.3)$$

The cation exchange capacities of clay minerals (illite, smectite, kaolinite, chlorite, etc.) are orders of magnitudes larger than that of quartz and feldspar (e.g. Carroll, 1959), thus the cation exchange capacity can be treated as a sum of the clay mineral components. In the Gulf of Mexico the clay mineral components show spatial (e.g. Taggard and Kaiser, 1960; Berti, 2003) and temporal (Freed, 1981) variation. Additionally, there is a well-documented diagenetic transition of smectite to illite, from 20% illite at depths shallower than 1500m to 80% illite by 3500m (e.g. Ahn and Peacor, 1989; Huang *et al.*, 1993; Elliot and Mastioff, 1996), associated with overpressured sediments (Kim *et al.*, 2001).

The mineralogy used in this study was that of the Revil *et al.* (1998) which was consistent with shallow sediments. This means that pure sand (at γ_{ss}) represented 15% clay, and pure shale (at γ_{sh}) represented 80% clay. Since the wells in this study were deeper than the Revil *et al.* (1998) study, and over-pressuring is in shallower sediments in this area (Dugan and Germaine, 2008), the clay component was corrected with the assumption that inter-layered smectite-illite transitioned from 20% to 80% illite, to reflect the smectite-illite transition.

Table 3.4. Table lists temperature-depth relations used in this study. General equation is of the form temperature = A + B×Z where temperature is in °C, and Z is depth from the seafloor in kilometers (see Fig. 3.2). Revil *et al.* (1998) initially used the bottom temperature of 25°C found by Cathles and Nunns (1991) for shallow (60-90m) water, however this study uses 4°C because the water is generally deeper.

Protraction Area	**Abbreviation**	**A (°C)**	**B (°C/km)**	**Source**
Garden Banks	GB	30.3	0.0127	Hanor and Mumphrey (2008)
Green Canyon	GC	20.8	0.0181	Hanor and Mumphrey (2008)
Mississippi Canyon	MC	22.1	0.0204	Hanor and Mumphrey (2008)
All others	AT, EC, EI, SM	4	0.0207	Revil *et al.* (1998)

3.5. Molecular Diffusion Solute Transport Model

Vertical salinity profiles above salt and below salt were selected for curves fitting with calculated molecular diffusion curves using the solute transport model of Ogata (1970). The Ogata (1970) model describes diffusion and advection through a homogeneous isotropic medium, with a constant temperature, and a uniform initial salinity, over some time period from a plane of constant salinity inserted into preexisting sediments at time zero. The planes of constant salinity here are the sediment-salt interfaces above and below salt.

The Ogata (1970) equation is:

$$C_m = \left(erfc\left(\frac{L - V_x t}{\sqrt[2]{D_L t}}\right) + exp\left(\frac{V_x L}{D_L}\right) erfc\left(\frac{L + V_x t}{\sqrt[2]{D_L t}}\right)\right) + C_i \quad (3.4)$$

Where erfc is the complementary error function, C_m (g/L) is the modeled salinity at the given distance from the salinity plane, C_s (g/L) is the concentration at a plane of constant salinity, C_i (g/L) is the initial salinity, L (m) is the distance from the plane, V_x (m/s) is the average linear velocity, t (s) is the time, and D_L (m^2/s) is the longitudinal dispersion coefficient. Xu and Eckstein (1995) give D_L (m^2/s) as:

$$D_L = 0.83(\log(L))^{2.414}\ V_x + D_{sed} \quad (3.5)$$

The above equations were simplified by setting advection (V_x) to zero, and placing the plane of constant salinity at the base of the vertical diffusion curve. The resulting equation using the error function (erf), is the same as the one-dimensional transient diffusion (Fig. 3.3) from Crank (1975) and was used to model the salinity curves:

$$C_m = (C_s - C_i)\,\mathrm{erf}\left(\frac{L}{2\sqrt{D_{sed}t}}\right) + C_i \quad (3.6)$$

Calculating the diffusion coefficient of the sediments, D_{sed} (m^2/s), takes several steps. First the (D°) diffusion coefficient for NaCl in free solution at 25°C is determined. This ranges from 1.48×10^{-9} to 1.59×10^{-9} (m^2/s) and is a function of the concentration (Rard and Miller, 1979; Lasaga, 1997). Since the concentration is unknown at this point, the lowest diffusion coefficient value of 1.48×10^{-9} m^2/s is used.

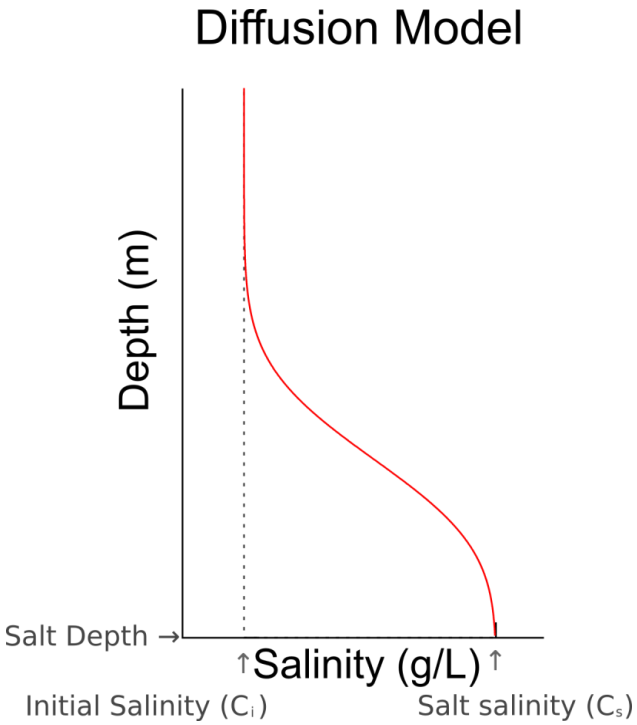

Figure 3.3. Example diffusion curve from a plane of constant salinity calculated from Equation 3.4 (Crank, 1975). Shown are initial salinity (C_i), salt salinity (C_s), and salt depth.

The diffusion coefficient was corrected for temperature (D_T) using the Einstein (1905) relation as cited by Lasaga (1997):

$$D_T = D^\circ \left(\frac{\eta}{298} / \frac{\eta}{T + 272} \right) \quad (3.7)$$

Where T (°C) is absolute temperature and η is fluid viscosity (assumed to be 0.01). To correct for tortuosity (θ) and porosity (φ), the following relationship was used:

$$D = D_T \frac{\varphi}{\theta^2} \quad (3.8)$$

Where tortuosity (θ) is calculated from porosity (φ) by using the empirical relationship of Boudreau (1996), which closely approximates the theoretical model of Boudreau and Meysman (2006):

$$\theta^2 = 1 - \ln(\varphi^2) \quad (3.9)$$

3.6. Quantitative Solute Transport Model Evaluation

Quantitative evaluation used the residual sum of squares (RSS) (Wild and Seber, 2000) as a proxy to describe how well the model fit the observed salinities. The RSS was calculated as the sum of the squares of the differences between the observed salinity (C_o) and the modeled salinity (C_m) for each distance (from 0 to n) from the plane of constant salinity:

$$RSS = \sum_{L=0}^{n} (C_m - C_o)^2 \quad (3.10)$$

The RSS was used as it is a single number which describes how well the model describes the data: a lower RSS value indicates the model fit the data better than a higher RSS value. By using different input values into the solute transport equation (Equation 3.4), the RSS generally varies systematically (Fig. 3.4).

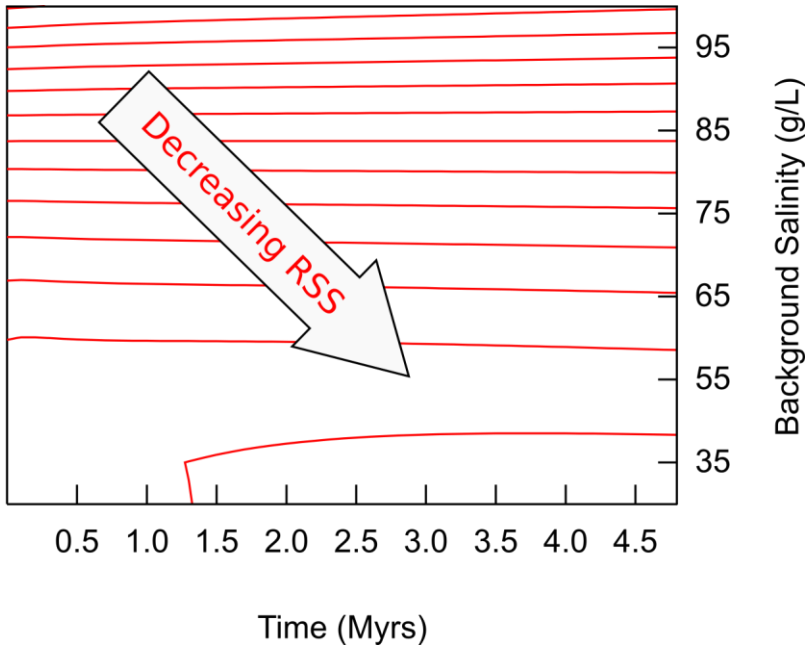

Figure 3.4. Residual Sum of Squares (RSS) is contoured for variations in two variables, time (T), and background salinity (C_S), are shown, with the other variables held constant. Sit shown is AT26 above salt. Contours represent equally valid descriptions of the data set. The lowest RSS values are for low background salinity (~35 g/L) and a long time (~4.5 Myr).

All observed salinity values were used, even though, as will be shown in the Results section, there is a high-frequency, high-amplitude, variation in calculated salinity. A possible problem with using RSS values to measure fit is that RSS assumes a normal distribution between the two variables that are being matched. If there was skewness in the high-amplitude variation, this would be reflected in the RSS value.

3.7. Gradient Descent Solver

1) A gradient descent solver is an iterative way of determining the minimum value in a multivariable concave space (Fig. 3.4) (Willis and Yeh, 1987). It requires the selection of a decision variable which will be minimized. In this study, the decision variable used is the residual sum of squares (RSS), the minimum value of which indicates the variables

which numerically fit the data the best. The gradient descent solve is summarized as follows:Using an assumed set of independent variables, the model is run, and the value to be minimized (RSS) is calculated.

2) For each of the independent variables (n), the model is run again with some small perturbations of the variable. This is done in order to estimate the change in the RSS with respect to changes in the value of the variable ($\delta RSS/\delta n$). In practice this means the model is run 2n + 1 times.

3) The variable which resulted in the largest decrease in RSS is then updated, and the sequence is run again. An example of steps 1-3 with two variables is shown in Fig. 3.5.

4)If there is no decrease in RSS, the sequence is re-run with smaller perturbations.

5) If the perturbations are less than some cut-off value, the best set of independent variables is assumed to be identified.

To use this method, each variable was initially perturbed by 10%. After the perturbations were updated, the perturbation amount was decreased to 1%, then 0.1% and so on, until there was no change in the RSS with perturbations equal to 10^{-10}.

A downside of this method for fitting a model to a set of data, is that the method assumes the set of values to be minimized forms a convex set. This, in turn, assumes there is one and only one minimum value, not local minimum values (Fig. 3.6).

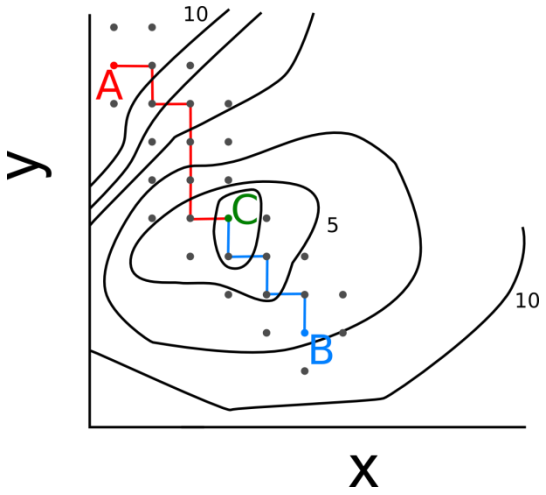

Figure 3.5. Gradient descent solver demonstration for two variables X and Y with some contoured decision variable. Both starting locations A and B result in a convergence at the lowest point C. Grey points show tested locations.

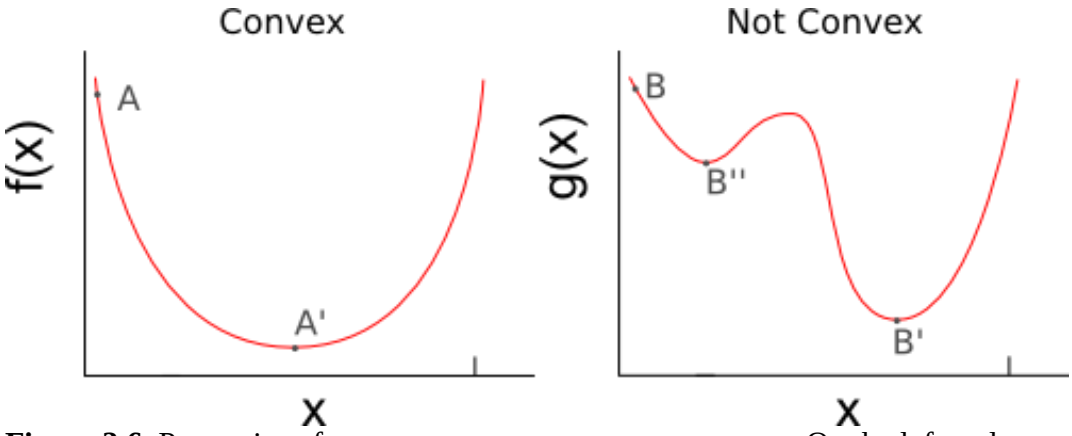

Figure 3.6. Properties of a convex set verse a non-convex set. On the left, values can progress down from A to the absolute minimum A'. On the right, values will go from B to the local minimum B'', but cannot make it to the absolute minimum B'.

The diffusion model with four independent variables to estimate: 1) initial salinity prior to diffusion (C_i); 2) concentration at the plane of constant salinity (C_s); 3) time (t); and 4) the diffusion coefficient (D) which is directly related to temperature. The depth of the plane of constant salinity was selected from the logs. The method uses a single porosity for the section (φ_{avg}) which is the average of the porosities at the top and bottom of the section of interest, each

of which were calculated using the Hanor and Mercer (2010) porosity-depth relationship described earlier:

$$\varphi_{avg} = \frac{\left(\varphi_{top} + \varphi_{bottom}\right)}{2} \tag{3.11}$$

Starting values for the gradient descent solver were an initial salinity of 35 g/L, a concentration constant plane salinity of 275 g/L, and a diffusion coefficient calculated for 80°C. To avoid non-convexity, each section was run with varying initial starting times of 100 kyrs, 1 Myrs, 2 Myrs, 5 Myrs, and 10 Myrs. Another set of variations was calculated at 1 Myrs, with starting temperatures every 20°C between 20°C and 140°C, and again at 10 Myrs with starting temperatures every 20°C between 20°C and 140°C.

Since these calculations uniformly resulted in a diffusion coefficient corresponding to a higher temperature than expected in the subsurface, the gradient descent solver was rerun, using various starting times as before, but holding diffusion (D), and therefore temperature constant. This was run using two assumptions: 1) the constant temperature used was the average temperature (T_{avg}) for the section of borehole, or 2) the temperature was that at the salt interface.

The average temperature (T_{avg}) for the section of borehole, was calculated as follows between the top (Z_0) and bottom (Z_1) where the borehole depths are given in feet, and the temperature at each depth (T_x) was calculated using the equations described in Table 3.2.

$$T_{avg} = \left(\sum_{x=Z_0}^{Z_1} T_x\right) \Big/ (Z_0 - Z_1) \tag{3.12}$$

The temperature at the salt interface was the temperature calculated using the equations in Table 3.2. This was an upper boundary for temperature above salt, and a lower boundary for temperature below salt.

3.8. Visual Fitting of Calculated Diffusion Curves to Observed Salinity Profiles

A simple visual fitting of calculated diffusion curves to observed salinity profiles was done to complement the RRS calculations described above (Hanor, personal communication, 2011). The molecular diffusion solute transport model describe above was used. The porosity (φ) and temperature (T) were held constant and calculated for the salt-sediment interface using the respective equations (Eqtn. 3.2; Table 3.4) from Hanor and Mercer (2010).

Instead of using all of the calculated salinity values generated by the Revil calculations, which show high-frequency and high-amplitude variations with depth, average salinity values at discrete small depth intervals above and below salt were visually determined. An Excel spreadsheet was created which permitted comparison of computed salinity profiles with observed profiles. The time (t), initial salinity (C_i), and high salinity (C_s) variables were adjusted until a reasonable visual fit of the computed salinity profiles to the observed profiles was obtained.

3.9. Basin2 Modeling

To model near seafloor emplacement of salt followed by continuous sediment deposition and compaction and advection-driven fluid flow (see Fig. 2.4; Hudec and Jackson, 2006), the Basin2 software modeling package was used. The Basin2 software package is a finite difference modeling program that can be used to model many steady-state and time-dependent hydrogeologic transport processes in either 1 or 2 dimensions (Bethke *et al.*, 2007). For this project, a series of one-dimensional transient models were run with one model run for each site

showing concave downward salinity profiles. These calculations considered the effects of sediment deposition, sediment compaction, molecular diffusion, and compaction-induced advection. An example of an annotated Basin2 input file for AT26 is provided in Appendix F.

Each run was divided into vertical biostratigraphic units with sediment thicknesses based on the BOEM paleontological data, with at least 10 finite elements for each unit. Since the Basin2 program input is the thickness at deposition not including compaction, the input thicknesses were modified until the modeled modern day compacted sediments thicknesses were within ±1 m of the thicknesses from the palentological data. However, repeated sections such as at GB272 were ignored. The salt layer itself was assumed to have been deposited one geologic stage earlier than the oldest paleontological marker above it. For example, in GB127, above salt biostratigraphy shows where the Messinian-Zanclian boundary (5.32 Ma) is; however, the age at the salt is not known, so it is assumed to be at the beginning of the Messinian stage (7.12). This overestimates the amount of time for the deposition of the first layer above salt.

The lithology for each biostratigraphic unit was assumed to be a sum of two components: 1) the average shale component ($\overline{sh}$), and 2) an average sand component ($\overline{ss}$). The average shale component ($\overline{sh}$) was calculated over the thickness of the biostratigraphic unit (Z_0 - Z_1) from the gamma ray log (γ_n) and the shale (γ_{sh}) and sand points (γ_{ss}):

$$\overline{sh} = \sum_{n=Z_0}^{Z_1} \left(\frac{\gamma_n - \gamma_{ss}}{\gamma_{sh} - \gamma_{ss}}\right) \Big/ n \tag{3.13}$$

The rest of the lithology was assumed to be the average sand component ($\overline{ss}$):

$$\overline{ss} = 100\% - \overline{sh} \tag{3.14}$$

To exclude abnormal gamma ray readings, only depths where the logged gamma ray fell between the shale and sand points were used. When a biostratigraphic unit did not have a gamma ray log because it was situated above the logged section, the lithology calculated for the nearest section of well with a known lithology was used. These lithologies set Basin2's rock properties which are empirical values found for North American interior basins (Bethke *et al.*, 2007).

The thermal regime used in the model assumed a was a surface temperature for all wells to be 8°C, as found by MacDonald (2002) at Bush Hill, located at Green Canyon block 185. While presumably this value was warmer due to fluid upwelling, calculations with 4°C were not significantly different. The temperature with depth model used the default conductive model with the heat flow of 1.5 heat flow units. Basin2 calculated thermal conductivities of each biostratigraphic unit which depended on the lithology and default rock properties.

Oceanic water depth was set to the constant modern-day value, neglecting sea level changes. Oceanic salinity was assumed to be a constant 35 g/L (0.599 molal), which is within 3 g/L of the mean oceanic salinity during the Cenozoic (Hay *et al.*, 2006). The sediment-salt interface was assumed to be constantly at halite saturation, meaning that Basin2 calculated the TDS using the temperature and Phillips *et al.* (1981) data for NaCl solubility. After the model successfully ran, salinities were converted from the molar units used by Basin2 to g/L.

4. RESULTS

4.1. Salt-Sediment Age Relations

The sedimentary sequence was interpreted for every borehole log using the isopach data from Feng and Buffler (1996) (Fig. 2.2) as well as the BOEM paleontologic data sets. On the basis of this paleostratigraphy, all but three of the boreholes (AT26, GB252, and GC563-0) penetrated sediments of Miocene age or younger.

The paleontologic data set also provided structural information. Of the 18 borehole logs penetrating salt, salt was clearly associated with thrust faulting in eight of the 13 blocks studied (Fig. 4.1; Appendix C). Of the remaining five blocks, MC167 lacked paleontological data above salt, GB272 had faulting shallower than the main salt body; the three other blocks, GC98, GC184, and EC185, may not have thrusts associated with the salt. In the wells without obvious thrusting, it is possible that the thrusting may have occurred, but was not significant enough to offset biostratigraphic markers. The prevalence of thrusting associated with salt means that interpretations based upon isopach thickness alone would underestimate the age of sediments above salt, and possibly overestimates the age of sediments below salt.

Using the biostratigraphic data and the isopach maps from Feng and Buffler (1996), two tables were compiled to compare the age of the sediments both above salt (Table 4.1) and below salt (Table 4.2). As the tables show, the two two data sets correspond fairly well, however the biostratigraphy provides better age constraints.

4.2. Sedimentation Rates

Average sedimentation rates above salt through time (Fig. 4.2) were calculated for most of the sites from the observed thickness of each unit as determined from the biostratigraphy.

Only units that spanned the entire geologic stage were used. Units that were bounded by salt were not included in these calculations since salt is allochthonous, and therefore the amount of time represented in those units is less than in the associated geologic stage. These modern thicknesses were divided by the time elapsed in each biostraigraphic unit from Witrock et al. (2003). Since these are observed thicknesses, and compacted, these rates represent minimum estimates of average sedimentation over each biostraigraphic unit. Two sites, GB272 and MC167, lacked enough data to be included.

Sedimentation rates ranged from 7 to 5070 m/My with median Pleistocene sedimentation (1598 m/My) significantly more rapid than median Pliocene sedimentation (200 m/My) and median Miocene sedimentation (75 m/My). In all cases the sedimentation rate peaked after the Calabrian-Ionian boundary at 0.78 Ma.

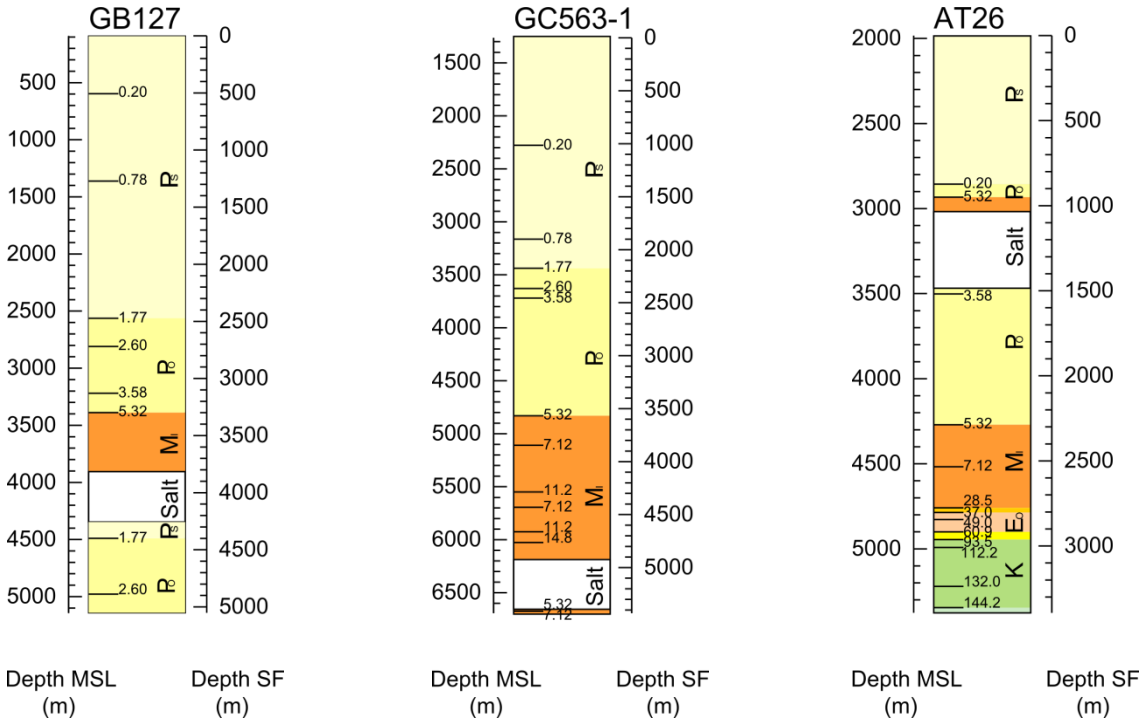

Figure 4.1. Three examples of results from biostratigraphy work, showing salt situated between older sediments on top and younger sediments below. Ages, in millions of years, are at boundaries between geologic stages determined from biostratigraphy. Images from left to right are from GB127, GC563-1, and AT26. Biostratigraphy for all sites is in Appendix C.

Table 4.1. Table shows sediment age above salt for the Group 1 sites, interpreted from biostratigraphy (Appendix C) and Figure 2.2 (Feng and Buffler, 1996). Site AT26 has a thin layer of Messinian (Miocene) sediments immediately above salt, and GB272 has shallower older sediments of Serravallian (Miocene) age. MC167 lacks biostratigraphy constraints below salt.

Well	Salt Depth (m)	Biostratigraphic Age			Isopach Age
		Stage	Series	Ma	
AT26	3018	Ionian *	Pleistocene	0.20-0.78	Pleistocene
GB253	5075	Zanclian	Pliocene	3.58-5.34	Pliocene
GB272-0	778	Ionian*	Pleistocene	0.20-0.78	Pleistocene
GB272-1	774	Ionian*	Pleistocene	0.20-0.79	Pleistocene
GC98-0	2350	Calabrian	Pleistocene	0.78-1.77	Pleistocene
GC563-0	5493	Zanclian	Pliocene	3.58-5.32	Pliocene
MC167	1741	?	Pliocene		Pleistocene
SM200	2670	Calabrian	Pleistocene	0.78-1.77	Pleistocene

Table 4.2. Table shows the sediment age below salt for sites which had logs below salt, interpreted from biostratigraphy (Appendix C) and Figure 2.2 (Feng and Buffler, 1996). Note the isopach thickness here does not account for salt thickness.

Well	Salt Depth (m)	Biostratigraphic Age			Isopach Age
		Stage	Series	Ma	
AT26	3473	Piacenzian	Pliocene	2.60-3.58	Pleistocene
GB127	4348	Gelasian	Pliocene	2.60-1.77	Pliocene
GB272-1	2968	Calabrian	Pleistocene	0.78-1.77	Pliocene
MC167	2893	Zanclian	Pliocene	3.58-5.32	Pleistocene
MC292-0	3016	Piacenzian	Pliocene	2.60-1.77	Pliocene
SM200	3111	Calabrian	Pleistocene	0.78-1.77	Pliocene

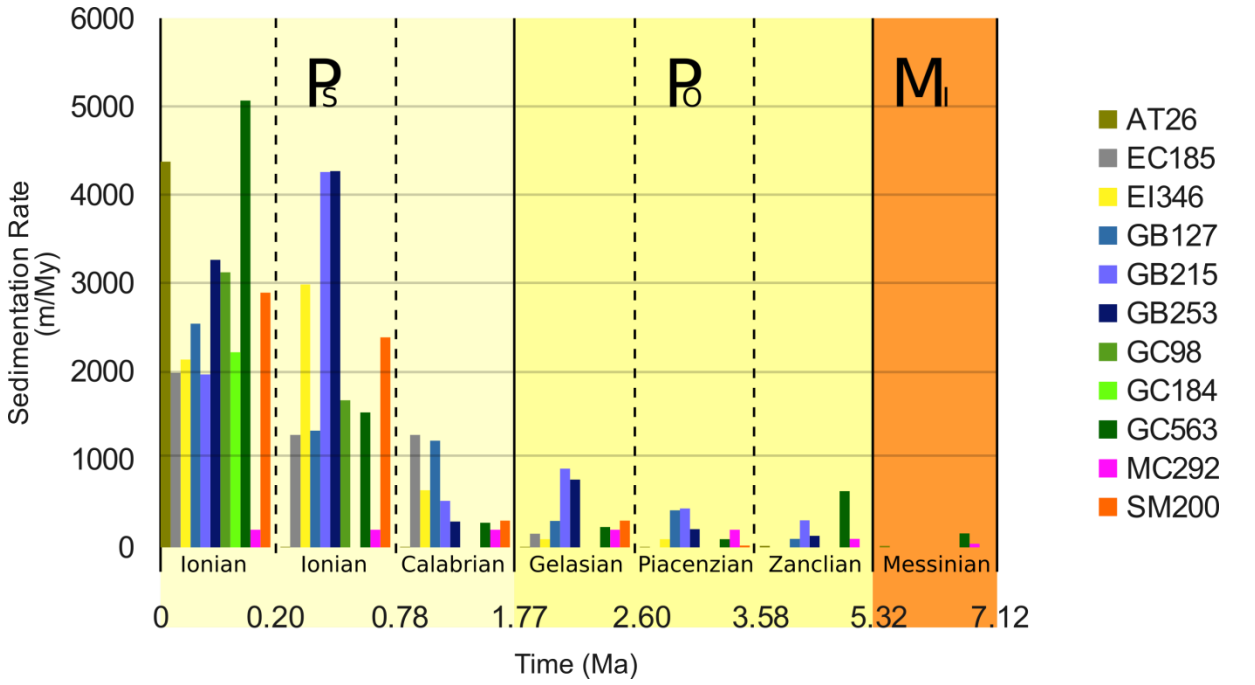

Figure 4.2. Sedimentation rates above salt by block, calculated from the current thicknesses of geologic stages from BOEM paleontological data, divided by the length of each geologic stage from Witrock *et al.* (2003). Results are reported only for biostratigraphic units not bounded by salt. The GB272 and MC167 sites are not shown because of a lack of data above salt. Sediment compaction may mean that deeper sediments have had a more rapid sedimentation rate than shown.

4.3. Salinity Trends Above Salt

Three distinctly different salinity trends (Fig. 4.3) exist in sediments above salt at the sites studied (Fig. 4.4). Sites in eight blocks (AT26, GB253, GB 272, GC 98, GC 563, MC167, MC292, SM200) have concave downward salinity profiles above salt, salinities in two blocks (EC185, GC184) increase upward and salinities in the two remaining blocks (GB127, GB215) are elevated but decreases slightly upward for distances of 500 to 1000 m above salt. The borehole at EI346 did not penetrate salt.

Since the concave downward salinity profiles showed salinities that generally trended to seawater salinities near the surface and approached halite saturation, this indicates that the Revil method was well calibrated.

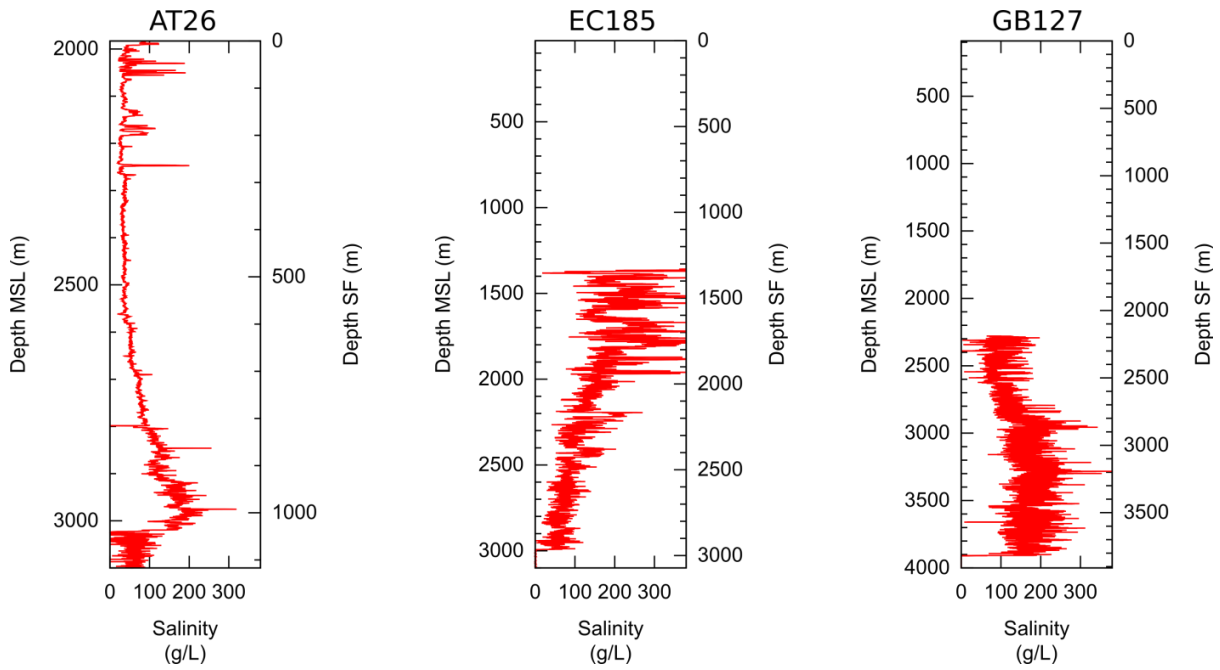

Figure 4.3. Examples of the three salinity trends above salt observed in this study, from left: concave downward (AT26), increase upward (EC185), and relatively constant (GB127). Figure 4.4 shows the geographic spread of the three trends. Salinities for all sites are given in Appendix C. High frequency noise in these trends is from the measurement technique, as seen in the results of Revil et al. (1998) and Hanor and Mercer (2010).

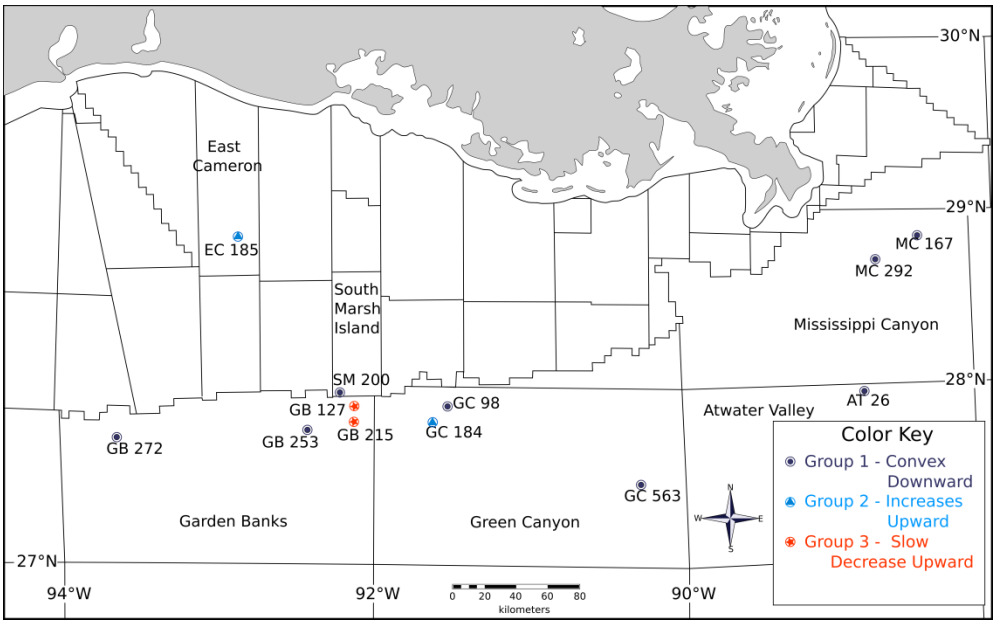

Figure 4.4. Map showing locations of sites organized by the salinity pattern above salt (Fig. 4.3). Group 1 sites show convex downward trends, group 2 sites show salinity increasing upward, and group 3 sites show a slow decrease upward. One site (EI346) had no boreholes with usable data for this analysis.

4.4. Diffusion Modeling of Salinity Trends Above Salt

The concave downward salinity profiles closely resemble transient molecular diffusion profiles or transient compaction-driven advection and diffusion profiles, such as modeled by McDuff and Gieskes (1976) and Ranganathan and Hanor (1987). The diffusion calculations performed here simulate what the salinity trends above salt would be if salt were emplaced at depth in the sediment column and subsequent upward molecular diffusion of dissolved NaCl from the salt-sediment interface were the only mechanism of solute transport.

There are two ways that a diffusion model was evaluated: 1) by how accurately it described the salinity data, and 2) whether the required amount of time for diffusion was geologically possible, based upon paleontology age constraints. If the model did not describe the salinity data well, or if the required time was too long for the age of the sediments, then the model is incorrect.

The gradient descent solver provided the best numerical fit to the salinity data, which finds the average of the high-frequency, high-amplitude variations (Fig. 4.5). The solver was run under two conditions: 1) allowing the diffusion coefficient (e.g. temperature) to vary, and 2) constraining the diffusion coefficient to a calculated average temperature. The simple visual fitting of the data deals with the issue of the high-frequency, high-amplitude variations by averaging.

As can be seen in Tables 4.3-6, which compare the results of the three diffusion models for above salt with the ages from the biostratigraphy, both the RSS and the simple diffusion calculations yielded times required for diffusion which exceed the average ages of the sediments

above salt. In general, the RSS technique yielded longer times for diffusion than the simple diffusion calculation method.

There are two sources of error which may cause the temperature to be overestimated. Since the diffusion coefficient (D° in Equation 3.7) slightly increases due to increased NaCl concentration (Rard and Miller, 1979) but is held constant here, this means at higher salinities, the temperature is less than the reported value by up to 7%. If advective flow were taken into account, the diffusion coefficient would be increased as a result of dispersion (Eqtn. 3.5), which would also be reported as temperatures higher than they should be.

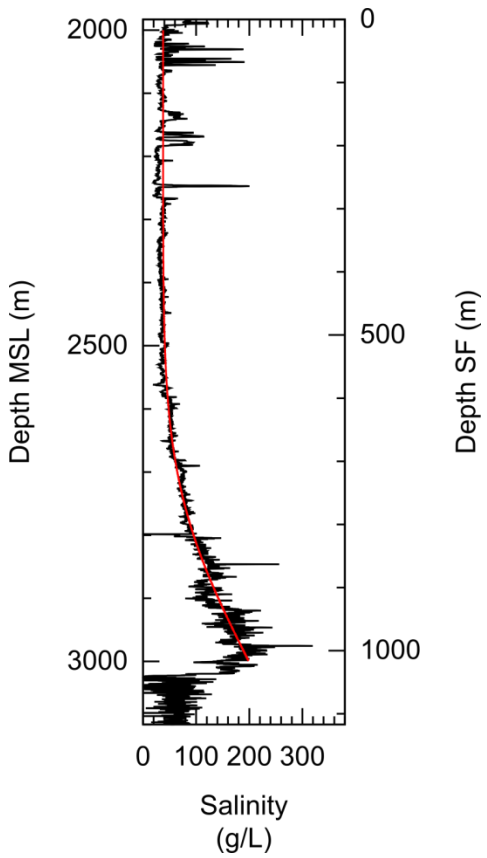

Figure 4.5. Example of the gradient descent solver best fit between the diffusion equation (in red), and the measured salinity (in black) above salt for AT26. Images of best fits for all the sites are in Appendix D.

Table 4.3. Resulting best fit parameters for diffusion modeling using the gradient solver above salt, with temperature allowed to change. Parameters are described in Equation 3.4, and Figure 3.3. Time is compared against the age of the sediment in Table 4.1. Most uncertainty is between temperature and age. Associated curves are shown in Appendix D.

Site	Time (My)	Temperature (°C)	Initial Salinity (g/L)	Salt Salinity (g/L)	Salt Depth MSL (m)
AT26	4.8	78.9	37.7	199.1	3000
GB253	50.2	87.1	51.2	138.7	5000
GB272-0	2.3	80.0	35.0	174.9	775
GB272-1	2.1	80.0	35.0	184.7	775
GC98-0	16.7	119.2	90.8	227.7	2300
GC563-0	27.5	80.0	35.0	129.4	4000
MC167	1.9	80.0	35.0	145.7	1650
SM200	19.7	94.9	90.8	159.0	2430

Table 4.4. Resulting best fit parameters for diffusion modeling using the gradient solver above salt, with temperature as a constant, calculated as the average above salt temperature (Eqtn. 3.10). Parameters are described in Equation 3.4, and Figure 3.3. Time is compared against the age of the sediment in Table 4.1.

Site	Time (My)	Temperature (°C)	Initial Salinity (g/L)	Salt Salinity (g/L)	Salt Depth MSL (m)
AT26	5.8	14.7	38.5	199.4	3000
GB253	35.3	58.5	58.5	144.6	5000
GB272-0	2.7	34.2	35.0	174.9	775
GB272-1	2.4	36.7	35.0	184.7	775
GC98-0	16.9	39.3	99.9	228.4	2300
GC563-0	22.9	45.6	42.4	130.7	4000
MC167	1.5	177.6	35.0	145.7	1650
SM200	17.0	31.8	92.6	163.5	2430

Table 4.5. Resulting best fit parameters for diffusion modeling using the gradient solver above salt, with temperature as a constant, calculated as temperature at the salt depth. Parameters are described in Equation 3.4, and Figure 3.3. Time is compared against the age of the sediment in Table 4.1.

Site	Time (My)	Temperature (°C)	Initial Salinity (g/L)	High Salinity (g/L)	Salt Depth MSL (m)
AT26	5.6	25.0	38.5	199.4	3000
GB253	50.3	86.6	51.2	138.7	5000
GB272-0	2.6	38.1	35.0	174.9	775
GB272-1	2.3	38.0	35.0	184.7	775
GC98-0	15.9	57.7	99.9	228.5	2300
GC563-0	21.3	70.3	42.4	130.7	4000
MC167	2.1	28.7	35.0	145.7	1650
SM200	11.2	51.3	93.5	169.3	2430

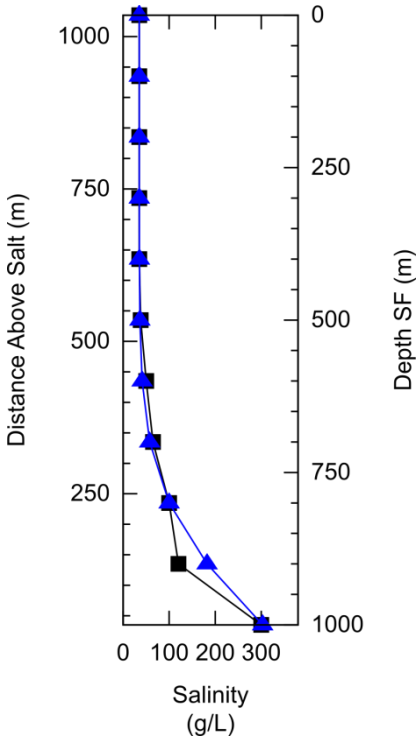

Figure 4.6. Graph showing visual fitting of diffusion above salt for AT26, between average salinity values (black squares) and diffusion curve (blue triangles). Graphs for all wells are located in Appendix E.

Table 4.6. Best fit using the visual fitting of diffusion above salt. Parameters are described in Equation 3.4, and Figure 3.3. Time is compared against the age of the sediment in Table 4.1. Graphs are shown in Appendix E.

Site	Time (My)	Temperature (°C)	Initial Salinity (g/L)	High Salinity (g/L)
AT026	2.5	39.8	35	350
GB253	10	78.2	35	350
GB272	0.6	38.0	35	350
GC098	10	51.7	70	350
GC563	100	86.6	35	350
GC563	10	86.6	35	350
MC167	1.5	28.6	35	350
MC292	9.0	39.7	35	350
SM200	8.0	76.2	60	350

4.5. Compaction-Modeling of Trends Above Salt

The Basin2 model was run to calculate what the vertical variations in salinity would be if salt were emplaced near the seafloor and then buried by subsequent sediment deposition to its present depth below the seafloor (Fig. 4.7). The driving forces for upward solute transport from the salt-sediment interface now include compaction-driven advection as well as molecular diffusion. This model uses the presumed sedimentation rates above salt, and, in a sense, represents the temporal evolution of sedimentation in the basin. Basin2 was run on all wells with biostratigraphic data above salt, and results are included in Appendix D.

Near salt sheets, the salinities calculated using Basin2 were higher at the salt-sediment interface than the observed salinities, indicating that the salt sediment interface is a lower than halite saturation. Farther from the salt-sediment interface, Basin2 results were generally lower than the observed salinities.

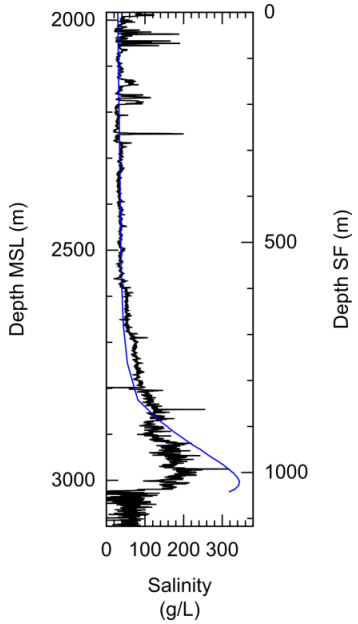

Figure 4.7. Example of the Basin2 modeling, based on the biostratigraphy and gamma ray log, compared against the observed salinity trends above salt for AT26. Figures for all of the sites are in Appendix D.

4.6. Salinity Trends Below Salt

At several sites where there is sub-salt logging data, there is a convex upward increase in salinity to the salt-sediment interface. Modeling of molecular diffusion downward from the salt-sediment interface in a similar way to the above salt cases (e.g. Fig. 4.8) yields ages that are younger than the sediments (Table 4.7-10).

Calculations below salt using Basin2 were not made, because it was assumed that the sediments below salt were close to their present degree of compaction at the time salt was emplaced. Further compaction as a result of increasing burial would most likely drive fluid flow laterally rather than vertically upward because of the presence of salt, similar to what Oliver (1986) described resulting from compression due to thrust sheets overriding sediments in

orogenic belts in a foreland basin. Salt has very tight porosity, so vertical fluid flow through salt would be very low compared to the higher porosity accretionary wedge sediments in an orogenic belt, meaning lateral flow should be greater underneath salt sheets than it is underneath an accretionary wedge.

Table 4.7. Resulting best fit parameters for diffusion modeling using the gradient solver below salt, with temperature allowed to change. Parameters are described in Equation 3.4, and Figure 3.3. Time is compared against the age of the sediment in Table 4.2. Most uncertainty is between temperature and age. Associated curves are shown in Appendix D.

Site	Time (My)	Temperature (°C)	Initial Salinity (g/L)	Salt Salinity (g/L)	Depth MSL (m)
AT26	6.3	80.0	35.0	78.8	4700
GB127	3.3	75.4	68.7	131.1	4500
GB272-1	29.0	80.0	42.4	116.3	3000
MC167	12.8	80.4	46.6	102.7	2900
MC292-0	10.8	119.2	60.3	122.7	3211
SM200	8.7	76.0	82.0	217.0	3211

Table 4.8. Resulting best fit parameters for diffusion modeling using the gradient solver below salt, with temperature as a constant, calculated as the average below salt temperature (Eqtn. 3.10). Parameters are described in Equation 3.4, and Figure 3.3. Time is compared against the age of the sediment in Table 4.2.

Site	Time (My)	Temperature (°C)	Initial Salinity (g/L)	Salt Salinity (g/L)	Depth MSL (m)
AT26	6.4	73.7	35	78.8	4700
GB127	3.1	95.8	68.7	131.1	4500
GB272-1	21.2	78.9	46.6	119.1	3000
MC167	8.2	65.4	51.2	106.2	2900
MC292-0	7.5	73	68.2	124.5	3211
SM200	6.7	75	90.8	219.8	3211

Table 4.9. Resulting best fit parameters for diffusion modeling using the gradient solver below salt, with temperature as a constant, calculated as temperature at the salt depth. Parameters are described in Equation 3.4, and Figure 3.3. Time is compared against the age of the sediment in Table 4.2.

Site	Time (My)	Temperature (°C)	Initial Salinity (g/L)	Salt Salinity (g/L)	Salt Depth MSL (m)
AT26	6.7	60.2	35.0	78.8	4700
GB127	3.2	86.3	68.7	131.1	4500
GB272-1	22.0	66.2	46.6	119.1	3000
MC167	8.5	54.2	51.2	106.2	2900
MC292-0	7.7	66.0	68.2	124.5	3211
SM200	6.9	65.4	90.8	219.8	3211

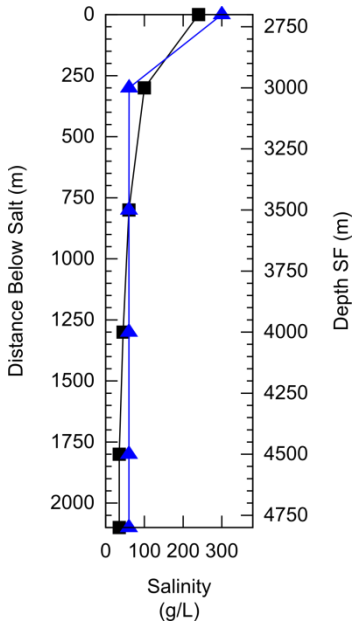

Figure 4.8. Graph showing visual fitting of diffusion below salt for GB272-1, between average salinity values (black squares) and diffusion curve (blue triangles). Graphs for all wells are located in Appendix E.

Table 4.10. Best fit using the visual fitting of diffusion below salt. Parameters are described in Equation 3.4, and Figure 3.3. Time is compared against the age of the sediment in Table 4.2. Graphs are shown in Appendix E.

Site	Time (My)	Temperature (°C)	Initial Salinity (g/L)	Salt Salinity (g/L)
GB127-1	0.65	75.6	60	350
GB127-1	0.9	75.6	60	300
GB272-0	7.0	58.5	35	350
GB272-1	10	58.5	40	240
MC167	10	50.2	35	300
MC167	11	50.2	40	220
MC292-1	3.0	57.0	35	220
SM200	3.5	68.5	60	350

5. DISCUSSION

5.1. Salinity Trends Above Salt

Three distinctly different salinity trends exist in sediments above salt at the sites studied (Fig. 4.4, Fig. 4.5): 1) concave downward, 2) an increase upward, and 3) elevated but decreasing slightly upward. The concave downward trends resemble transient molecular diffusion profiles. However, the results of diffusion calculations using two different approaches show that diffusion alone is too slow to generate these profiles. A better fit in terms of time was achieved by the Basin2 calculations, which take into account sedimentation and compaction-driven advection as an additional transport mechanism. However, the Basin2 calculations assumed halite saturation at the salt-sediment interface, which results in salinities higher than calculated.

At two of the sites, GC184 and EC185, there is an increase in salinity upward (from 50-100 g/L to 250-300 g/L) rather than a systematic decrease (Appendix C). These increases may reflect lateral transport of dissolved salt into the site. The GC 184 site is located in one protraction block, approximately three miles west of the Bush Hill chemosynthetic community located at Green Canyon block 185, which is associated with faulting, gas hydrate outcrops, and diffusion of gas through sediment (MacDonald, 2002). The NR-1 brine pool site associated with Bush Hill, located southeast of Bush Hill in Green Canyon block 233, has salinities equivalent to 121 g/L (MacDonald *et al.*, 1990) and could also be a source for lateral transport. The EC185 site is located on the Louisiana shelf, and the high shallow salinities there may be related to lateral migration of brine down-dip from the south Louisiana salt dome province. Nikiel and Hanor (1999) found that significant down-dip lateral transport of brine to the south has occurred in the South Timbalier protraction area over a similar distance from the present coastline (Fig. 5.1).

This mechanism could explain the high shallow salinities in this site as well. Similar to the South Timbalier section, the lower Pliocene (Piacenzian) had the highest average shale percentage (65%), the upper Pliocene (Gelasian) had the lowest average shale percentage (51%), with the lower Pleistocene (Calabrian) slightly higher (53%).

Two of the well blocks, GB 127 and GB 215, have salinities that decrease slightly upward. These two blocks are relatively near each other. The salinity results found here could be the result of brine ponding in a mini-basin, such as seen in the Bullwinkle field at GC 64 (Hanor and Mercer, 2010; Fig. 5.2). Wilson and Ruppel (2007) modeling study found brine ponding occurred if there were variations in the depth of the salt sheet, as early flow cells would be haline-dominated resulting in brines generated from the salt flowing into the basin until it is filled with brine.

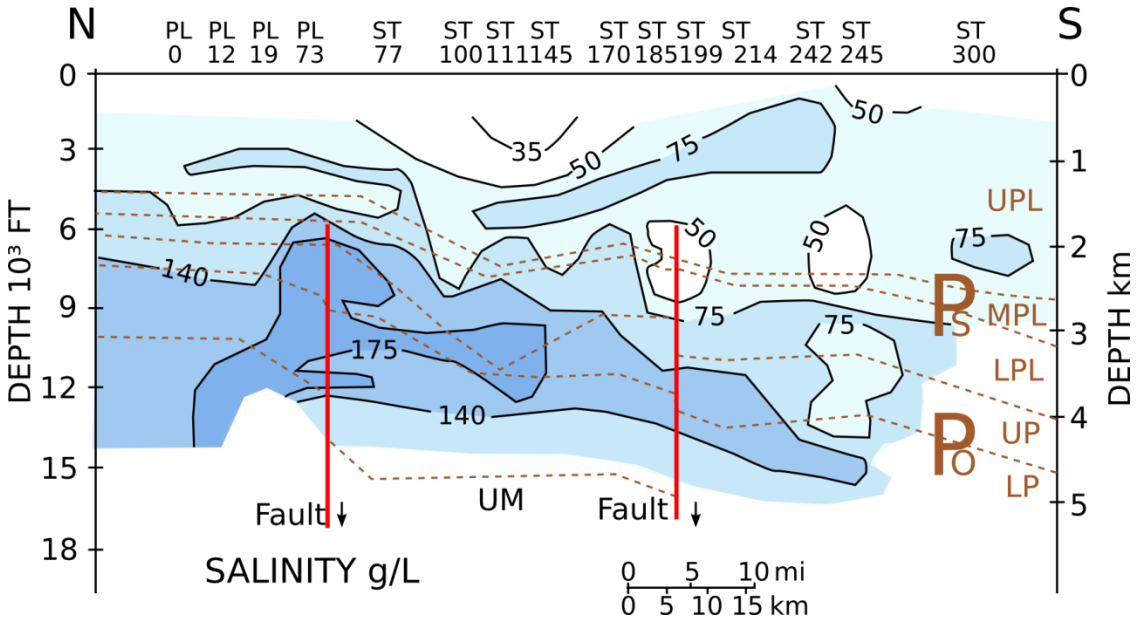

Figure 5.1. Lateral migration of a brine downdip to the south from the S.E. Louisiana shelf into the Gulf of Mexico through the South Pelto and South Timbalier protraction areas. Figure after Nikiel and Hanor (1999). Sediments range in age from Lower Pliocene (LP) through Upper Pleistocene (UPL). Salinity is sourced from shallow salt structures such as the Bay St. Elaine salt dome. Similar lateral migration from shallow salt may explain the salinities in the EC185 site.

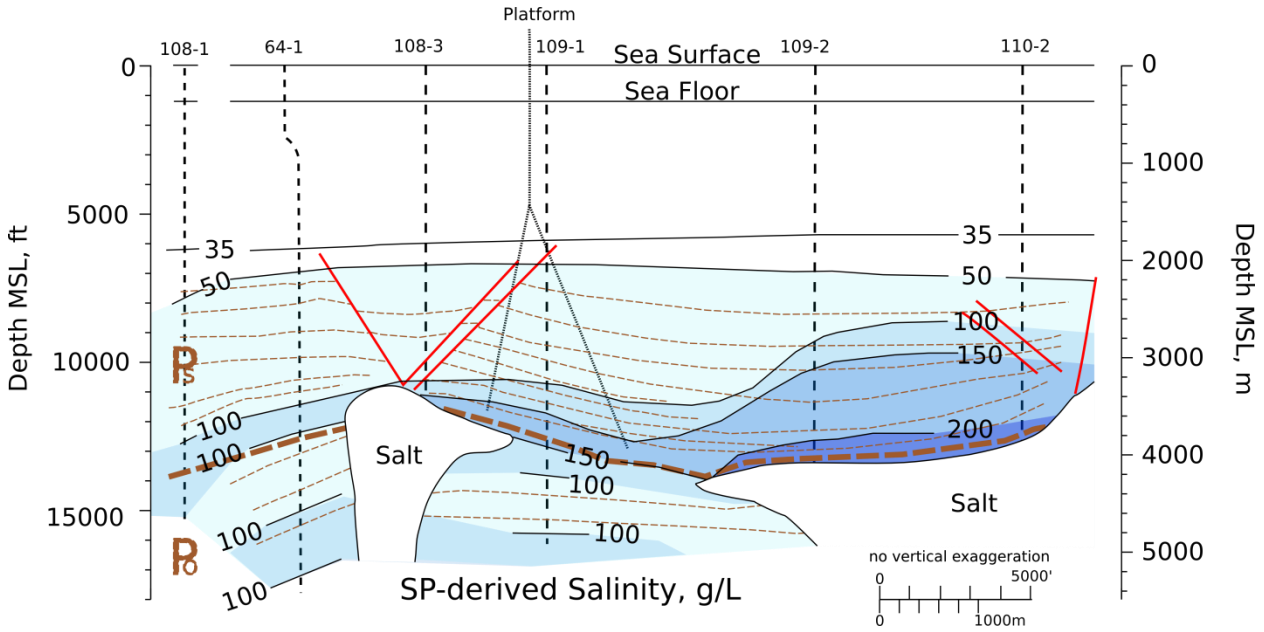

Figure 5.2. Image after Hanor and Mercer (2010) showing brine ponding in Bullwinkle field (Green Canyon 64) mini-basin. Brine ponding in a mini-basin may explain the slow salinity decrease upward in the GB 127 and GB 215 sites. Marker beds are indicated in thin dashed lines, and the Pliocene and Pleistocene interface is a condensed section represented by the thick dashed line.

5.2. Salinity Trends Below Salt

Sarkar *et al.* (1995) modeled the possible thermohaline convection of formation waters driven by the dissolution of salt at the base of allochthonous salt sheets in the Gulf of Mexico, for several salt geometries. These models assume an impervious basement layer at six kilometers, which corresponds to the Middle Jurassic of Weimer and Buffler (1992). Sarker found that it takes over a million years after the emplacement of a salt sheet for Rayleigh–Bénard instabilities to develop into down-welling plumes. Prior to this, molecular diffusion was expected to dominate solute transport. Down-welling plumes were expected to take roughly four million years to reach the basement, and to become more chaotic with time.

Observed sub-salt trends are concave-downward, and diffusion modeling generally indicates that the time required to set up these trends is less than the age of the sediments. Diffusion as the primary solute transport mechanism underneath salt is consistent with the Sarkar *et al.* (1995) model for less than a million years after the emplacement of a salt sheet. However, Sarker's conclusions assumed there had been 20 million years since the emplacement of salt, which is much older than the Miocene or younger aged sediments observed in this study.

5.3. Apparent Salinities at the Salt-Sediment Interfaces

The calculated salinities at the salt-sediment interfaces were often lower than halite saturation. There are several explanations for this: errors in the calculations, or some physical processes.

As discussed in Appendix B, there are multiple assumptions made that could explain the lower-than-halite saturation. Of these, the most likely is the use of assumed porosities that were too high. As seen in Fig. 5.3, a difference in the porosity of one percentage point would result in a change in the calculated salinity by 100 g/L. The porosity relations used in this study were from shallow sediments that were not permeated by hypersaline brines (Hanor and Mercer, 2010). Some clay minerals, such as smectite, swell in concentrated NaCl brines (Slade *et al.*, 1991); brines swelling the clays could make the porosity lower than expected, which in turn would make the calculated salinity lower. There is over-pressuring in the Gulf of Mexico, both observed by other authors (e.g. Mello and Karner, 1996; Kim *et al.*, 2001; Dugan and Germaine, 2008), and predicted in the Basin2 modeling in this study. However, only a small decrease in porosity is required to account for the observed difference between halite saturation and the calculated salinity values.

There also are three physical processes that could explain the lower-than-halite saturation calculated salinities: 1) the presence of shale sheaths, 2) caprock, or 3) water produced from dehydration reactions. The presence of a low porosity, high tortuosity shale sheath directly above allochthonous salt sheets could limit fluid interaction with the salt, would slow solute transport, although above this a normal salinity gradient would develop. Salt caprock minerals, which form from the partial dissolution and re-precipitation of non-halite salt minerals (e.g. Walker, 1976; Warren, 2005), could similarly act as a charged barrier to solute movement. Dehydration reactions, such as the smectite-illite conversion and gas and oil maturation, have been invoked as possible methods of pore water freshening (e.g. House and Pritchett, 1995; Szalkowski and Hanor, 2003; Saffer and McKiernan, 2009), and would result in lower salinities than otherwise expected. Due to the depths of the salt-sediment interface in this study, the thermally-controlled smectite-illite transition could have released water at the interface due to increase in temperature at the high thermal conductivity of salt. This was not modeled due to the lack of logs.

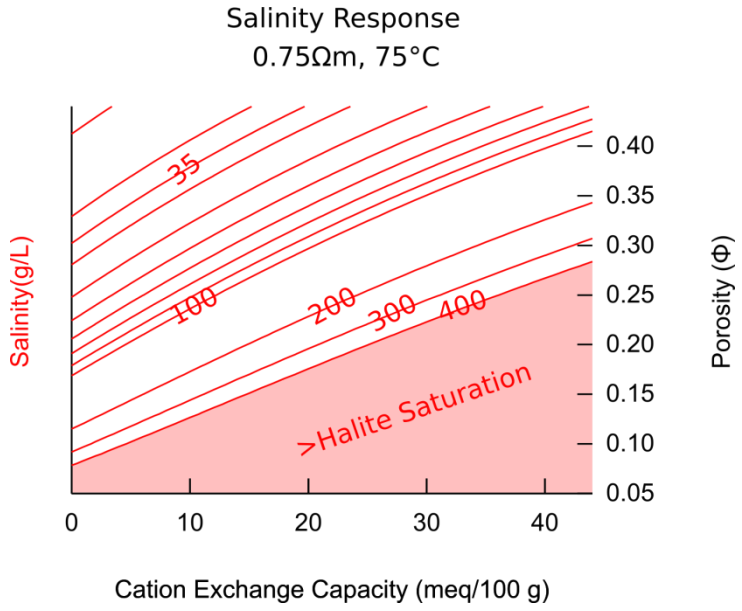

Figure 5.3. Iso-salinities were calculated and contoured as a function of porosity and CEC with average resistivity (0.75Ωm) and temperature (75°C). Qualitative analysis of error from the Revil *et al.* (1998) method is presented in Appendix B.

5.4. Evaluation of Basin2 Modeling Results

The differences between the Basin2 models and the measured salinities can be a combination of several factors. There could be errors in the calculated salinities resulting from the variables used in their calculations or there could be errors resulting in estimating the proper inputs into the Basin2. In calculating salinity, errors in porosity (Fig. 5.3) are the most significant variable, see Appendix B for details.

The Basin2 model may use sand and shale properties which differ from the actual Gulf of Mexico. In addition, the Basin2 model assumes halite is saturated at the salt-sediment interface and uses a time-dependent heat flow model (Bethke *et al.*, 2007). Since the concentration of saturated NaCl solutions is temperature dependent (Phillips *et al.*, 1981), a geothermal gradient higher than occur in the Gulf of Mexico would predict higher salinities than observed. All of the models do not account for horizontal movement of fluids, which may occur. Likewise the models do not account for horizontal movement of sediment, which probably occurred in several of the wells, most obviously in GB272-0, where there are Miocene age sediments overlying Pleistocene sediments.

Finally, the methods used to estimate the sediment composition for the hydrologic properties assumed that each biostratigraphic section would act like a single layer of mixed sand and shale. However, Gulf of Mexico fluids have been shown to periodically discharge (Roberts and Nunn, 1995), which indicates GOM shale layers may have a disproportionate effect on the properties of the bulk sediment.

6. CONCLUSIONS AND FUTURE WORK

Solute transport above allochthonous salt appears to be related to three different solute transport regimes in the sites studied.

In the group 1, sites which had the expected increase of salinity with depth, molecular diffusion alone was too slow to account for the observed curves. A more likely mechanism is diffusion and compaction driven advection, as modeled with Basin2. Because the diffusion and compaction model assumes that salt sheets spread out at or near the seafloor, this suggests that, prior to the Miocene-Pleistocene sedimentation, near floor sediments had significantly higher salinities and that resources sensitive to salinities, such as methane hydrates, would have had a significantly smaller stability range. Likewise, if there was shallow salt, the high thermal conductivity of salt (Petersen and Lerche, 1995; Mello *et al.*, 1995), may also result in sharper geothermal gradient, and shallower methane hydrate stability region. Two possible effects are: 1) in a greater flux of methane to fuel chemosynthetic communities, and 2) more salt outcroppings, creating more anoxic halocline-delimited brine pools.

In the group 2 sites, salinity increased upward, probably a result of lateral transport from shallow sources of salinity, such as from the south Louisiana coast (Nikiel and Hanor, 1999), or related nearby seafloor brine pools. In the group 3 sites, salinity slowly decreased upward indicating that the brine was pooling like in the Bulwinkle Field (Hanor and Mercer, 2010). Both of these salinity patterns imply lateral transport of solute, and constraining this requires future work with two or three dimensional information.

In most every borehole in this study, salt is located between older sediments on top and younger sediments below, indicating that the salt seems to have spread in a fault in a thrust

setting. This does not fit with the simplest models of allochthonous salt sheet formation: the salt-wing intrusion into preexisting sediments, and the salt glacier model of salt spreading on top of the sediment package. However, this is consistent with other near seafloor models for the spread of salt (Hudec and Jackson, 2006; Hudec and Jackson, 2007).

Solute transport below salt may constrain the timing of emplacement of salt where molecular diffusion alone is operating. Because the age of the sediment is greater than the time required for diffusion at the sites studied, this means diffusion cannot be ruled out as the only method of generating subsalt salinities. Diffusion as the sole method of subsalt solute transport is consistent with the Sarkar *et al.* (1995) model for emplacement of a salt sheet less than four million years before present day.

The results of this study, that there are several mechanisms of solute transport, help to explain why Hanor and Mercer (2010) were not able to find a single general relation between the salinity of pore waters at a given depth below the seafloor with and the distance to the top of salt.

Further exploration could utilize additional age constraints to investigate the timing of salt movement. If methane hydrate stability is found to be lower than predicted, it is likely that there are more, and more productive, chemosynthetic communities that could be identified and dated.

Future work would also include better characterization of the rock properties in the field area. This study approximated the cation exchange capacity using the Revil *et al.* (1998) mineralogy adopted for deeper sediments. Better thermal data would allow the use of the Huang *et al.* (1993) kinetic model to predict the smectite-illite transition at depth, or core samples could

be used to observe the electrical and permeability properties of the actual shale and sand compositions, which then could be used to better estimate temperature.

Finally, investigation into the sediment immediately in contact with the salt, possibly through core samples, could help explain the difference between the observed salinities directly above salt, and the expected halite saturation at the salt-sediment interface. As discussed, there are several explanations for this difference, including possible problems with the assumed porosity, or undetected physical properties such as the presence of high-tortousity shale sheaths, caprock, or excessive amounts of dehydration reactions.

REFERENCES CITED

Addy, S. K., and Behrens, E. W. (1980) Time of accumulation of hypersaline anoxic brine in Orca basin (Gulf of Mexico). Marine Geology 37 (3-4), 241-252 doi:10.1016/0025-3227(80)90104-8.

Ahn, J. H., and Peacor, D. R. (1989) Illite/Smectite from Gulf Coast shales: A reappraisal of transmission electron microscope images. Clays and Clay Minerals 37 (6), 542-546 doi:10.1346/CCMN.1989.0370606.

Alexiades, C. A., and Jackson, M. L. (1966) Quantitative clay mineralogical analysis of soils and sediments. Clays and Clay Minerals 14 (1), 35-52 doi:10.1346/CCMN.1966.0140104.

Archie, G. E. (1942) The electrical resistivity log as an aid in determining some reservoir characteristics. Petroleum Transactions of AIME 146, 54-62.

Bassiouni, Z. (1994) Theory, measurement, and interpretation of well logs. Society of Petroleum Engineers.

Bethke, C. M., Lee, M., and Park, J. (2007) Basin Modeling with Basin2. Hydrogeology Program University of Illinois.

Berti, D. (2003) Clay mineralogy and its effect on on physical properties in the Gulf of Mexico northwestern continental slope. MS Thesis: Texas A&M University.

Boudreau, B. P. (1996) The diffusive tortuosity of fine-grained unlithified sediments. Geochimica et Cosmochimica Acta 60 (16), 3139-3142 doi:10.1016/0016-7037(96)00158-5.

Boudreau, B. P., and Meysman, F. J. R. (2006) Predicted tortuosity of muds. Geology 34 (8), 693-696 doi:10.1130/G22771.1.

Bruno, R. S., and Hanor, J. S. (2003) Large-Scale Fluid Migration Driven by Salt Dissolution, Bay Marchand Dome, Offshore Louisiana. Gulf Coast Association of Geological Societies Transactions 53, 97-107.

Cathles, L. M., and Nunns, A. G. (1991) A Temperature Probe Survey on the Louisiana Shelf: Effects of Bottom-Water Temperature Variations: Geologic Note. AAPG Bull 75 (1), 180-186.

Connolly, C. A., Walter, L. M., Baadsgaard, H., and Longstaffe, F. J. (1990) Origin and evolution of formation waters, Alberta Basin, Western Canada sedimentary Basin. I. Chemistry. Applied Geochemistry 5 (4), 375-395 doi:10.1016/0883-2927(90)90016-X.

Crank, J. (1975) The Mathematics of Diffusion. 2nd Edition. Oxford University Press.

Diegel, F. A., Schuster, D. C., Karlo, J. F., Shoup, R. C., and Tauvers, P. R. (1995) Cenozoic structural evolution and tectono-stratigraphic framework of the Northern Gulf Coast continental margin. In M. P. A. Jackson and D. G. Roberts and S. Snelson (eds.) Salt tectonics: a global perspective , 109-151.

Dugan, B., and Germaine, J. T. (2008) Near-seafloor overpressure in the deepwater Mississippi Canyon, northern Gulf of Mexico. Geophysical Research Letters 35 (L02304), 1-5 doi:10.1029/2007GL032275.

Einstein, A. (1905) Uber die von der molekularkinetischen Theorie der Wärme geforderte Bewegung von in ruhenden Flüssigkeiten suspendierten Teilchen. Annalen der Physik 322 (8), 549-560 doi:10.1002/andp.19053220806.

Elliott, W. C., and Matisoff, G. (1996) Evaluation of kinetic models for the smectite to illite transformation. Clays and Clay Minerals 44 (1), 77-87 doi:10.1346/CCMN.1996.0440107.

Feng, J., and Buffler, R. T. (1996) Post Mid-Cretaceous Depositional History, Gulf of Mexico Basin. In J. O. Jones and R. L. Freed (eds.) Structural framework of the northern Gulf of Mexico 46, 9-25.

Fredrich, J. T., Fossum, A. F., and Hickman, R. J. (2007) Mineralogy of deepwater Gulf of Mexico salt formations and implications for constitutive behavior. Journal of Petroleum Science and Engineering 57 (3–4), 354-374 doi:10.1016/j.petrol.2006.11.006.

Freed, R. L. (1981) Shale Mineralogy and Burial Diagenesis of Frio and Vicksburg Formations in Two Geopressured Wells, Mcallen Ranch Area, Hidalgo County, Texas. GCAGSC 31, 289-293.

Galloway, W. E., Ganey-Curry, P. E., Li, X., and Buffler, R. T. (2000) Cenozoic depositional history of the Gulf of Mexico basin. AAPG Bulletin 84 (11), 1743-1774 doi:10.1306/8626C37F-173B-11D7-8645000102C1865D.

Griffin, G. M. (1962) Regional Clay-Mineral Facies–Products of Weathering Intensity and Current Distribution in the Northeastern Gulf of Mexico. Geological Society of America Bulletin 73, 737-767 doi:10.1130/0016-7606(1962)73[737:RCFOWI]2.0.CO;2.

Hanor, J. S., and Mercer, J. A. (2010) Spatial variations in the salinity of pore waters in northern deep water Gulf of Mexico sediments: implications for pathways and mechanisms of solute transport. Geofluids 10 (1-2), 83-93 doi:10.1111/j.1468-8123.2009.00271.x.

Hanor, J. S., and Mumphrey, J. A. (2008) Temperature-Depth Relations in Deep Water Gulf of Mexico Sediments: An Assessment from Equilibrated Bottom Hole Temperatures Obtained During Bottom Hole Pressure Surveys. 1-35.

Hanor, J. S., Nunn, J. A., and Lee, Y. (2004) Salinity structure of the central North Slope foreland basin, Alaska, USA: implications for pathways of past and present topographically driven regional fluid flow. Geofluids 4 (2), 152-168 doi:10.1111/j.1468-8115.2004.00079.x.

Harrison, W. J., and Summa, L. L. (1991) Paleohydrology of the Gulf of Mexico basin. American Journal of Science 291 (2), 109-176 doi:10.2475/ajs.291.2.109.

Hermanrud, C., Cao, S., and Lerche, I. (1990) Estimates of virgin rock temperature derived from BHT measurements: Bias and error. Geophysics 55 (7), 924-931 doi:10.1190/1.1442908.

Hay, W. W., Migdisov, A., Balukhovsky, A. N., Wold, C. N., Flögel, S., and Söding, E. (2006) Evaporites and the salinity of the ocean during the Phanerozoic: Implications for climate, ocean circulation and life. Palaeogeography, Palaeoclimatology, Palaeoecology 240 (1-2), 3-46 doi:10.1016/j.palaeo.2006.03.044.

House, W. M., and Pritchett, J. A. (1995) Fluid Migration and formation pressures associated with allochthonous salt sheets in the northern Gulf of Mexico. In Sixteenth Annual Research Conference , 121-124. Gulf Coast Section SEPM Foundation.

Huang, W., Longo, J. M., and Pevear, D. R. (1993) An experimentally derived kinetic model for smectite-to-illite conversion and its use as a geothermometer. Clay and Clay Minerals 41 (2), 167-177.

Hudec, M. R., and Jackson, M. P. A. (2006) Advance of allochthonous salt sheets in passive margins and orogens. AAPG Bulletin 90 (10), 1535-1564 doi:10.1306/05080605143.

Hudec, M. R., and Jackson, M. P. A. (2007) Terra infirma: Understanding salt tectonics. Earth-Science Reviews 82 (1–2), 1-28 doi:10.1016/j.earscirev.2007.01.001.

Kim, J., Berg, R. R., Watkins, J., and Tieh, T. T. (2001) Texture, Mineralogy, and Petrophysical Properties of Geopressured Shales, Gulf of Mexico. Gulf Coast Association of Geological Societies Transactions 51, 161-172.

Lasaga, A. C. (1998) Kinetic Theory in the Earth Sciences. Princeton University Press.

Ma, C., and Eggleton, R. A. (1999) Cation exchange capacity of kaolinite. Clays and Clay Minerals 47 (2), 174-180 doi:10.1346/CCMN.1999.0470207.

MacDonald, I. R. (2002) Stability and Change in Gulf of Mexico Chemosynthetic Communities. Minerals Management Service, U.S. Department of the Interior.

MacDonald, I. R., Reilly, II, J. F., Guinasso, Jr., N. L., Brooks, J. M., Carney, R. S., Bryant, W. A., and Bright, T. J. (1990) Chemosynthetic Mussels at a Brine-Filled Pockmark in the Northern Gulf of Mexico. Science 248 (4959), 1096-1099 doi:10.1126/science.248.4959.1096.

McDuff, R. E., and Gieskes, J. M. (1976) Calcium and magnesium profiles in DSDP interstitial waters: Diffusion or reaction?. Earth and Planetary Science Letters 33 (1), 1-10 doi:10.1016/0012-821X(76)90151-5.

McIntosh, J. C., and Walter, L. M. (2005) Volumetrically significant recharge of Pleistocene glacial meltwaters into epicratonic basins: Constraints imposed by solute mass balances. Chemical Geology 222 (3-2), 292-309 doi:10.1016/j.chemgeo.2005.07.010.

Mello, U. T., and Karner, G. D. (1996) Development of Sediment Overpressure and Its Effect on Thermal Maturation: Application to the Gulf of Mexico Basin. AAPG Bulletin 80 (9), 1367-1396.

Mello, U. T., Karner, G. D., and Anderson, R. N. (1995) Role of salt in restraining the maturation of subsalt source rocks. Marine and Petroleum Geology 12 (7), 697-716 doi:10.1016/0264-8172(95)93596-V.

Nikiel, A. M., and Hanor, J. S. (1999) Spatial Variations in Formation Water Salinities, South Pelto and South Timbalier Areas, Eastern Louisiana Continental Shelf. Gulf Coast Association of Geological Societies Transactions 49, 396-403.

Ogata, A. (1970) Theory of Dispersion in a Granular Medium. Geological Survey Professional Paper 411-I, I1-I34.

Oliver, J. (1986) Fluids expelled tectonically from orogenic belts: Their role in hydrocarbon migration and other geologic phenomena. Geology 14 (2), 99-102 doi:10.1130/0091-7613(1986)14<99:FETFOB>2.0.CO;2.

Person, M., McIntosh, J., Bense, V., and Remenda, V. H. (2007) Pleistocene hydrology of North America: The role of ice sheets in reorganizing groundwater flow systems. Reviews of Geophysics 45 (RG3007), 1-28 doi:10.1029/2006RG000206.

Petersen, K., and Lerche, I. (1995) Quantification of thermal anomalies in sediments around salt structures. Geothermics 24 (2), 253-268 doi:10.1016/0375-6505(94)00051-D.

Phillips, S. L., Igbeen, A., Fair, J. A., Ozbek, H., and Tavana, M. (1981) A Technical Databook for Geothermal Energy Utilization. LBL-12810, 1-60 doi:10.2172/6301274.

Pilcher, R. S., and Blumstein, R. D. (2007) Brine volume and salt dissolution rates in Orca Basin, northeast Gulf of Mexico. AAPG Bulletin 91 (6), 823-833 doi:10.1306/12180606049.

Ranganathan, V., and Hanor, J. S. (1987) A numerical model for the formation of saline waters due to diffusion of dissolved NaCl in subsiding sedimentary basins with evaporites. Journal of Hydrogeology 92 (1-2), 97-120 doi:10.1016/0022-1694(87)90091-6.

Rard, J. A., and Miller, D. G. (1979) The mutual diffusion coefficients of NaCl–H2O and CaCl2–H2O at 25°C from Rayleigh interferometry. Journal of Solution Chemistry 8 (10), 701-716 doi:10.1007/BF00648776.

Revil, A., Cathles, L. M., Losh, S., and Nunn, J. S. (1998) Electrical conductivity in shaly sands with geophysical applications. Journal of Geophysical Research 103 (B10), 23925-23936 doi:10.1029/98JB02125.

Riccardi, A. C. (2009) RE: Ratification of the definition of the base of Quaternary System/Period (and top of the Neogene System/Period), and redefinition of the base of the Pleistocene Series/Epoch (and top of the Pliocene Series/Epoch). http://www.stratigraphy.org/upload/IUGS%20Ratification_Q%20&%20Pleistocene.pdf .

Roberts, H. H., Feng, D., and Joye, S. B. (2010) Cold-seep carbonates of the middle and lower continental slope, northern Gulf of Mexico. Deep Sea Research Part II: Topical Studies in Oceanography 57 (21–23), 2040-2054 doi:10.1016/j.dsr2.2010.09.003.

Roberts, S. J., and Nunn, J. A. (1995) Episodic fluid expulsion from geopressured sediments. Marine and Petroleum Geology 12 (2), 195-204 doi:10.1016/0264-8172(95)92839-O.

Rubey, W. W., and Hubbert, M. K. (1959) Role of fluid pressure in mechanics of overthurst faulting I. Mechanics of fluid-filled porous solids and its application to overthurst faulting. GSA Bulletin 70 (2), 167-206 doi:10.1130/0016-7606(1959)70[115:ROFPIM]2.0.CO;2.

Saffer, D. M., and McKiernan, A. W. (2009) Evaluation of in situ smectite dehydration as a pore water freshening mechanism in the Nankai Trough, offshore southwest Japan. Geochemistry Geophysics Geosystems 10 (Q02010), doi:10.1029/2008GC002226.

Salvador, A. (1987) Late Triassic-Jurassic Paleogeography and Origin of Gulf of Mexico Basin. AAPG Bulletin 71 (4), 419-451.

Sarkar, A., Nunn, J. A., and Hanor, J. S. (1995) Free thermohaline convection beneath allochthonous salt sheets: An agent for salt dissolution and fluid flow in Gulf Coast Sediments. Journal of Geophysical Research 100 (B9), 18085-18092 doi:10.1029/95JB01857.

Slade, P. G., Quirk, J. P., and Norrish, K. (1991) Crystalline swelling of smectite samples in concentrated NaCl solutions in relation to layer charge. Clays and Clay Minerals 39 (3), 234-238 doi:10.1346/CCMN.1991.0390302.

Spears, R. W. (2000) Relationship between over pressured compartments and spatial variations in pore fluid salinity in sediments of South Marsh Island, OCS 310 Offshore Louisiana. MS Thesis: Louisiana State University.

Soller, D. R., Lindquist, T. A., Boore, S., Brunstein, F. C., Donatich, A. J., Ghequiere, K., Koch, R. D., Lane, D. E., Mayfield, S. E., Nimz, K., Schumacher, G., Scott, S. L., Stettner, W., Vigil, J. F., and Zigler, J. L. (2000) Geologic Age Symbol Font (StratagemAge). In Public Review Draft – Digital Cartographic Standard for Geologic Map Symbolization.

Szalkowski, D. S., and Hanor, J. S. (2003) Spatial variations in the salinity of produced waters from southwestern Louisiana. GCAGS/GCSSEPM Transactions 53, 798-806.

Taggard, Jr, M. S., and Kaiser, Jr, A. D. (1960) Clay mineralogy of Mississippi River deltaic sediments. Geological Society of America Bulletin 71 (5), 521-530 doi:10.1130/0016-7606(1960)71[521:CMOMRD]2.0.CO;2.

US Army Corps of Engineers (2004) Corpscon Version 6.x Technical Documentation and Operating Instructions.

Walker, C. W. (1973) Nature and origin of caprock overlying Gulf Coast Salt domes. In The Fourth International Symposium on Salt, 169-195.

Warren, J. (2005) Evaporates: Sediments, Resources and Hydrocarbons. In Salt Tectonics, 447-449.

Weimer, P., and Buffler, R. T. (1992) Structural Geology and Evolution of the Mississippi Fan Fold Belt, Deep Gulf of Mexico. AAPG Bulletin 76 (2), 225-251.

Wild, C. J., and Seber, G. A. F. (2000) Chance Encounters: A first Course in Data Analysis and Inference. John Wiley & Sons, Inc.

Willis, R., and Yeh, W. W. (1987) Groundwater Systems Planning & Management. Prentice-Hall, Inc.

Wilson, A., and Ruppel, C. (2007) Salt tectonics and shallow subseafloor fluid convection: models of coupled fluid-heat-salt transport. Geofluids 7 (4), 377-386 doi:10.1111/j.1468-8123.2007.00191.x.

Witrock, R. B., Friedmann, A. R., Galluzzo, J. J., Nixon, L. D., Post, P. J., and Ross, K. M. (2003) Biostratigraphic chart of the Gulf of Mexico offshore region, Jurassic to Quaternary.

Xu, M., and Eckstein, Y. (1995) Use of Weighted Least-Squares Method in Evaluation of the Relationship Between Dispersivity and Field Scale. Ground Water 33 (6), 905-908 doi:10.1111/j.1745-6584.1995.tb00035.x.

APPENDIX A: REVIL METHOD VARIABLES AND EQUATIONS

A.1 Constants and Equations for Revil Method

The Revil *et al.* (1998) method, simplified by Spears (2000), has a number of constants which are used in the calculations. Formation density (ρ_g) for siliclastic rocks is 2650 kg/m^3. Assuming a NaCl dominated fluid, as expected from GOM salt (Fredrich *et al.*, 2007), the cation, Na, has one free electron ($Z_s = 1$). The surface mobility (β_s), at standard temperature ($T_0 = 25°C$) for Na is $\beta_s(T_0) = 5.14 \times 10^{-9}$. The ion coefficient of surface conductivity is $V_s = 0.040\ °C^{-1}$, the formation sensitivity factor is $V_f = 0.023\ °C^{-1}$. The cementation exponent of a clean sand is $m_0 = 1.80$, and the cementation coefficient ($\alpha = 1.58$ mL/meq) relates cementation to CEC.

The excess surface charge per unit pore volume (Q_v) is calculated from the formation CEC, porosity (φ), and formation density (ρ_g) as:

$$Q_v = \frac{\rho_g \, CEC_{fmt}(1-\varphi)}{\varphi} \tag{A.1}$$

Fluid surface mobility (β_s) needs to be corrected for temperature:

$$\beta_S = \beta_S(T_0)\big(1 + V_s\,(T - T_0)\big) \tag{A.2}$$

Using the results of the above two equations, calculate the surface conductivity of the formation (σ_s) for the assumed Na-dominated fluid is calculated:

$$\sigma_s = \frac{\frac{2}{3}\varphi}{1-\varphi}\beta_s Z_s Q_v \tag{A.3}$$

To find the fluid conductivity, we need to first find the cementation exponent (m) for the temperature, surface charge, and porosity:

$$m = m_0 + \left(\frac{\alpha\, Q_v\, \varphi}{1 - \varphi}\right) \tag{A.4}$$

From this we calculate the formation factor (F) of Archie (1942):

$$F = \frac{1}{\varphi^m} \tag{A.5}$$

With this we can calculate the fluid conductivity at formation temperature (σ_f):

$$\sigma_f = \left(\frac{F}{rest}\right) - (2\, F\, \sigma_s) + (2\sigma_s) \tag{A.6}$$

Which is converted to fluid conductivity at standard temperature ($\sigma_f(T_0)$) by the following relation:

$$\sigma_f(T_0) = \frac{\sigma_f}{1 + \left(V_f\, (T - T_0)\right)} \tag{A.7}$$

This is converted to the electrolyte conductivity (C_f) which is in mols/L using the salinity and electrolyte conductivity of seawater. Seawater has a conductivity of 5 S/m at standard temperature, and the salinity of a NaCl electrically equivalent to seawater is 0.56 mol/L.

$$C_f = 0.56\, \frac{\sigma_f(T_0)}{5} \tag{A.8}$$

To convert to salinity, multiply by the atomic mass of NaCl (58.4428 g/mol) to get the salinity in g/L.

$$Salinity = C_f \times 58.4428 \tag{A.9}$$

Table A.1. List of all of the variables used in calculating the Revil *et al.* (1998) duel electronic method for calculating pore water salinitiy.

Symbol	Range	Units	Meaning	Source
Master Parameters				
φ	<0.5		Porosity	Depth relationships from Hanor and Mumphrey (2008), $\varphi = 0.29 \times \exp(-0.0018 \times depth(m)) + 0.295$
T	17.8-115.5	°C	Formation Temperature	Depth relationships from Hanor and Mumphrey (2008), see Table A.2
Rest	0.3-3	Ωm	Resistivity	90" Array Resistivity Log; Deep Resistivity Log; Resistivity Log; or, inverse of Conductivity Log (listed in Appendix C)
CEC_{fmt}	$\leq CEC_{sh}$	mol g^{-1}	Formation Cation Exchange Capacity	Calculated: $CEC_{fmt} = CEC_{sh} \times \varphi_{sh}$
Calculating Master Parameters				
γ_{log}	10-130	GAPI	Gamma Ray Log Response	Gamma Ray Log
γ_{sh}	110-130	GAPI	Pure Shale	Max Gamma Ray Log response in siciclastic rocks (see Appendix C)
γ_{ss}	40-60	GAPI	Pure Sand	Min Gamma Ray Log response in siciclastic rocks (see Appendix C)
φ_{sh}	0-100%		Shale percentage	Calculated: $\varphi_{sh} = \frac{\gamma_{log} - \gamma_{ss}}{\gamma_{sh} - \gamma_{ss}}$
CEC_{sh}	0.0223	mol g^{-1}	Cation Exchange Capacity of the clay component	Calculated from clay ratio (Revil *et al.*, 1998), max and min smectite/illite rato (Ahn *et al.*, 1989; Huang *et al.*, 1993), and mineral CEC values (Ma and Eggleton, 1999; Berti, 2003; Alexiades and Jackson, 1966)
Revil Method Constants				
T_0	25	°C	Standard Temperature	Revil *et al.* (1998)
$\beta_s(T_0)$	5.14×10^{-9}		Na surface mobility at 25°C	Revil *et al.* (1998)
v_s	0.04	$°C^{-1}$	Ion coefficient of	Revil *et al.* (1998)

			surface conductivity	
Z_s	1		Free Na electrons	Revil *et al.* (1998)
α	1.58	mL meq^{-1}	Cementation coefficient to CEC	Revil *et al.* (1998)
m_0	1.8		Cementation exponent of a clean sand	Revil *et al.* (1998)
Revil Method Calculated Variables				
Q_v		mol/m^3	Excess Surface Charge per unit pore volume	Calculated: $Q_v = \frac{\rho_g \, CEC_{fmt}(1-\varphi)}{\varphi}$
β_s			Fluid Surface Mobility	Calculated: $\beta_S = \beta_S(T_0)\left(1 + V_s\,(T - T_0)\right)$
σ_s			Formation Surface Conductivity	Calculated: $\sigma_s = \frac{\frac{2}{3}\varphi}{1-\varphi}\beta_s Z_s Q_v$
m			Cementation Exponent	Calculated: $m = m_0 + \left(\frac{\alpha\, Q_v\, \varphi}{1-\varphi}\right)$
F			Formation Factor	Calculated: $F = \frac{1}{\varphi^m}$
σ_f			Fluid Conductivity	Calculated: $\sigma_f = \left(\frac{F}{rest}\right) - (2\,F\,\sigma_s) + (2\sigma_s)$
$\sigma_f(T_0)$			Fluid Conductivity at 25°C	Calculated: $\sigma_f(T_0) = \frac{\sigma_f}{1 + \left(V_f\,(T - T_0)\right)}$
C_f	<6.85	mols/L	Electrolyte Conductivity	Calculated: $C_f = 0.56\,\frac{\sigma_f(T_0)}{5}$
Salinity	<400	g/L	Salinity	Calculated: $Salinity = C_f \times 58.4428$

APPENDIX B: REVIL METHOD ERROR ANALYSIS

The Revil *et al.* (1998) method, as outlined in Appendix A, allows for the calculation of salinity from five lithologic properties: porosity, resistivity, cation exchange capacity (CEC), temperature, and density. This study used well logs as a data source, so a number of assumptions were used to estimate these lithologic properties. An attempt was made to understand the causes of error in these assumptions, as well as the effect this error would propagate into resulting salinities for the worst case scenarios and the differences from shallower wells.

The CEC value has several assumptions, as cores were not available for direct measurements of CEC, or clay composition. CEC was estimated by estimating a clay CEC, as well as a percent shale derived from the gamma ray log. The clay composition found by Revil *et al.* (1998) for the Gulf of Mexico (GOM) was corrected for the transition of inter-layered smectite-illite from 20% illite at shallow depths to 80% illite below 2500m in the GOM (Kim *et al.*, 2001; Huang *et al.*, 1993; Elliot and Mastioff, 1996). Fig.5.3, B.1, and B.2 show how variations in CEC relate to variations in the salinity result. Additionally, clay composition at depth can vary (Freed, 1981). Sources of this variation include variations in sediment sources, such as modern Mississippi clay composition which varies with tributary configuration (Taggard and Kaiser, 1960; Berti, 2003), and weathering changes (Griffin, 1962).

Percent shale was determined by selecting “pure” sand point and shale point on the gamma ray log. The shale and sand points are estimated separately for each well, and these are listed in Appendix C. In this study, pure shale was assumed to be 80% clay, and pure sand was assumed to be 15% clay.

Formation temperature used published depth relationships. Available temperature data was mostly in the form of bottomhole temperatures, which would require corrections to account for drilling fluids (Hermanrud *et al.,* 1990), and interpolation. Several wells in this study had temperature logs, but these were likewise uncorrected. The temperature-depth curves used in this study only use depth, and do not include salt-thickness, and therefore do not model the positive and negative geothermal anomalies above and below salt (Petersen and Lerche, 1995). As shown in Fig. B.1, errors in temperatures are less important at higher temperatures, and at lower CEC, indicating that salinities at greater depths are less sensitive to errors in temperature than at shallow depths.

Porosity also used published depth relationships rather than logged values, as the porosity logs did not cover all the wells as logged. Additionally, neutron porosity is sensitive to chloride ions, which is proportional to salinity in NaCl-dominated brines such as in this study, and needs corrections based upon salinity (Bassiouni, 1994). Density-derived porosity requires an estimation of fluid density, which is also salinity dependent. Fig. 5.3 shows errors in porosity are more important than CEC, however this decreases with the CEC and increases with porosity.

Resistivity logs selected for use in this study were ideally widely-spaced or deep resistivity, to minimize the effect of low resistivity drilling mud invasion, when these were not present, other logs, such as conductivity logs, were used. Log type used in this study is listed in Appendix C. Figure B.2 shows that errors in resistivity are less important at higher resistivity, but more important at lower CEC.

This indicates that the lower clay CEC in deep wells below the smectitie-illite transition means that the estimation of the sand and shale points in these wells is relatively more important than in shallower wells.

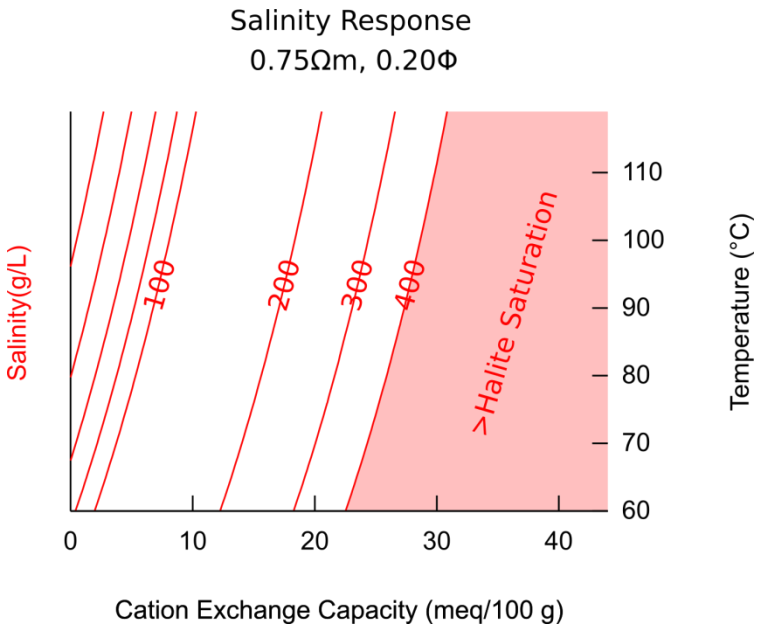

Figure B.1. Iso-salinities are contoured as a function of temperature and CEC with for a resistivity (0.75Ωm) and porosity (0.2).

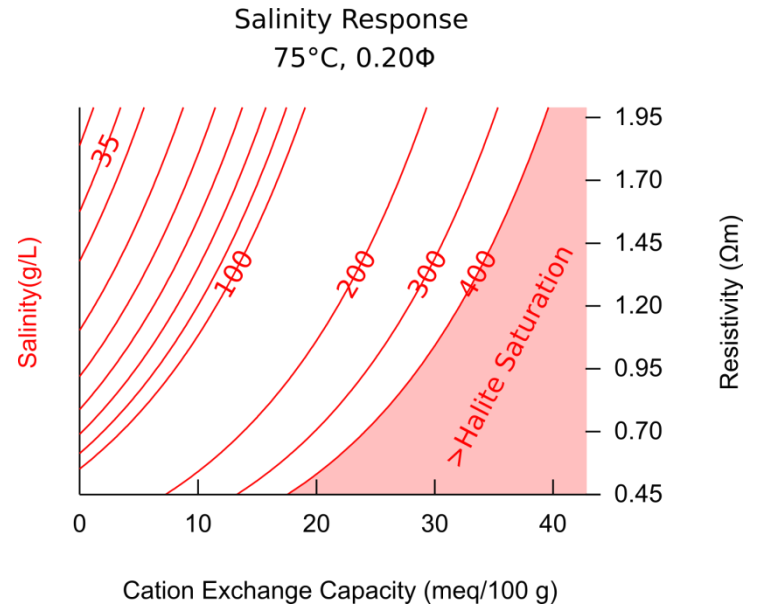

Figure B.2. Iso-salinities are contoured as a function of resistivity and CEC with for a temperature (75°C) and porosity (0.2).

APPENDIX C: WELL ATLAS

Included here is a listing of information from each well in this study, including block number, API number, protraction area, location, and drill date from the well log header file. Also listed are constants used in this study, such as the water depth, shale, and sand points. The source and type of the resistivity log used for calculating salinity with the Revil Method is also listed, as well as the locations of wells with paleodata used in this study. Salt thicknesses, determined from the well logs, are also listed.

In addition to listed information, maps for each well block in this study were generated using bathymetric maps from NOAA. Block numbers are in red, protraction area boundaries are in gray, and water depths are in blue. Where available, well locations according to the header file, are plotted as green circles using the BOEM protraction area definitions.

Finally for each well, the gamma ray, resistivity, interpreted paleontological data, and calculated salinities are shown, as depth from mean sea level (MSL) and as depth from seafloor (SF).

Atwater Valley 26 (AT26)
Well API Number: 608184001100
Location: 27°57′57.2″N 88°40′41.1″W
Partners: BP
Drill Date: 8/17/1999
Water Depth: 1983 m
Shale point: 120 GAPI
Sand point: 50 GAPI
Resistivity: ILD (Deep Resistivity)
Age: Paleontological age data only from this well, as there were no other nearby wells.
Salt Depth: 3018-3473m from MSL

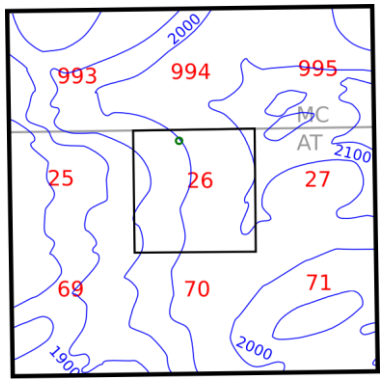

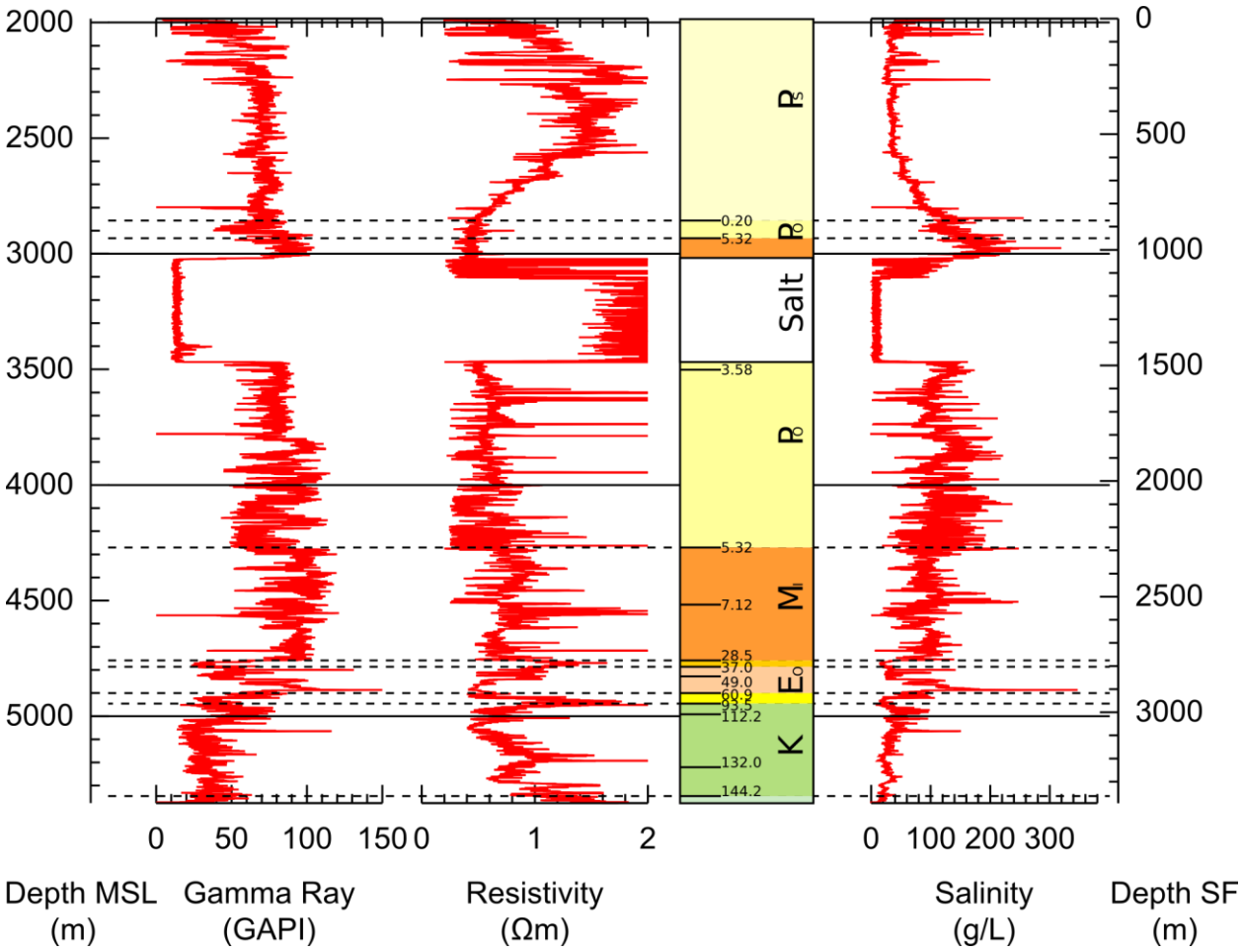

East Cameron 185 (EC185)
Well API Number: 177034091300
Location: 28°50′1.2″N 92°43′14.1″W
Partners: Remington Oil & Gas
Drill Date: 7/12/2001
Water Depth: 28 m
Shale point: 105 GAPI
Sand point: 40 GAPI
Resistivity: AT90 (90in Array Resistivity)
Age: 14 nearby wells with paleodata: 2 from EC178, 1 from EC179, 7 from EC185, 3 in EC195, and 1 in EC196.
Salt Depth: 2990-3164m from MSL

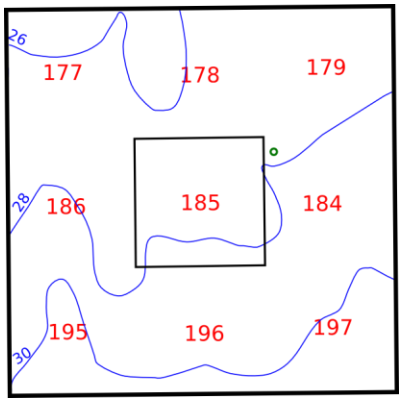

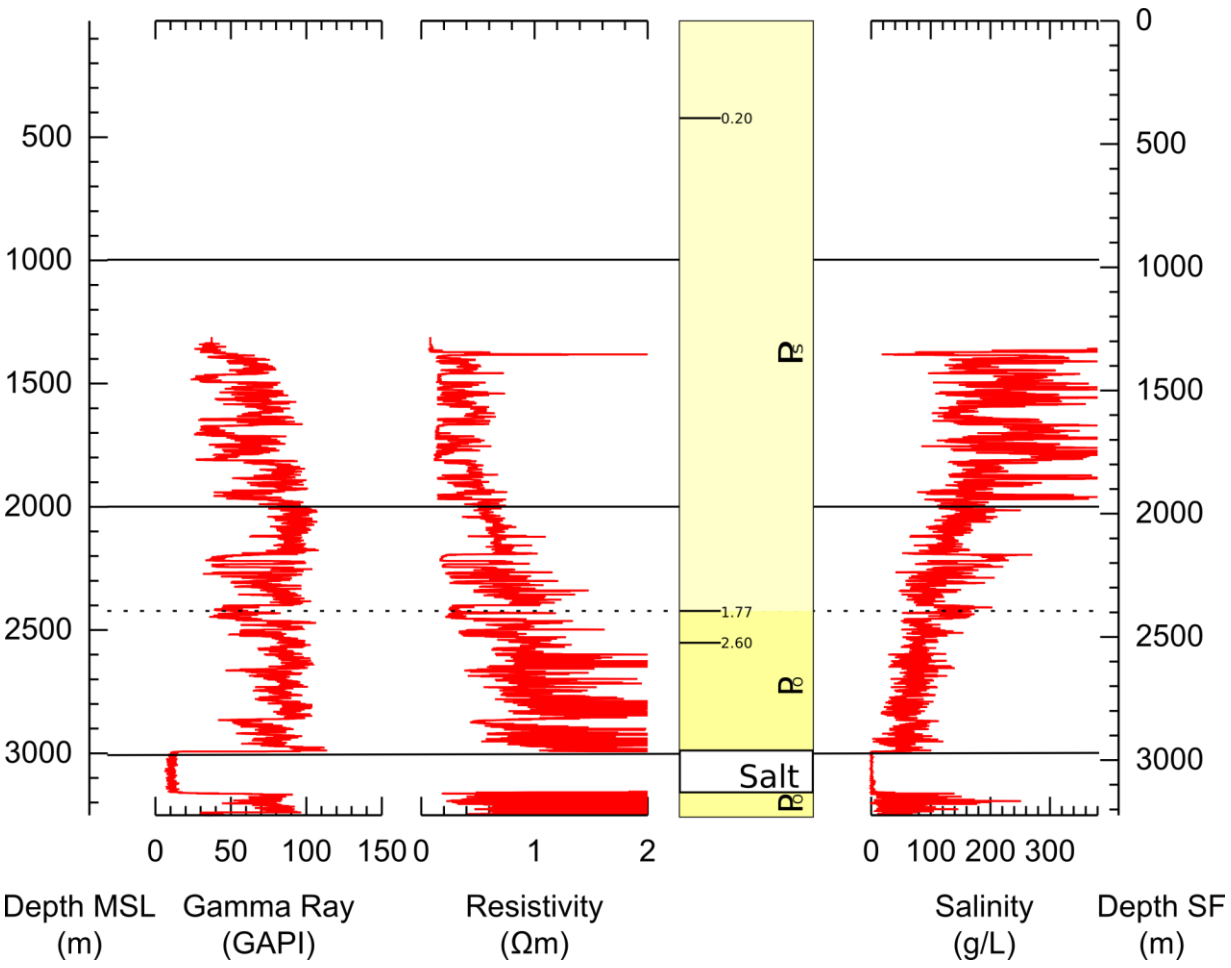

Eugene Island 346 (EI346)
Well API Number: 177104159200
Water Depth: 147.8 m
Shale point: 100 GAPI
Sand point: 40 GAPI
Resistivity: DRESWS (Resistivity 400 kHz Compensated Borehole Corrected)
Age: 37 nearby wells with paleodata: 1 from EI344, 9 from EI345, 1 from SS319, 18 from EI346, 1 from SS320, 4 from EI366, 2 from EI367, 2 from SS343. Most age data is from 177104151900 (EI346).
Salt Depth: probably between 3120-3140 m from MSL, assumed from nearby paleontologcal-data

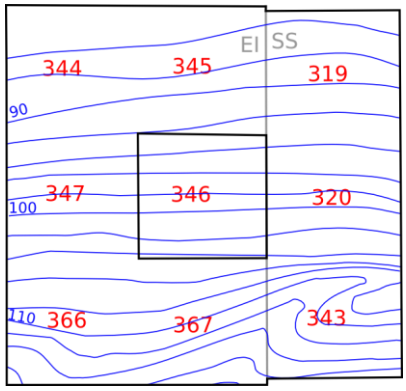

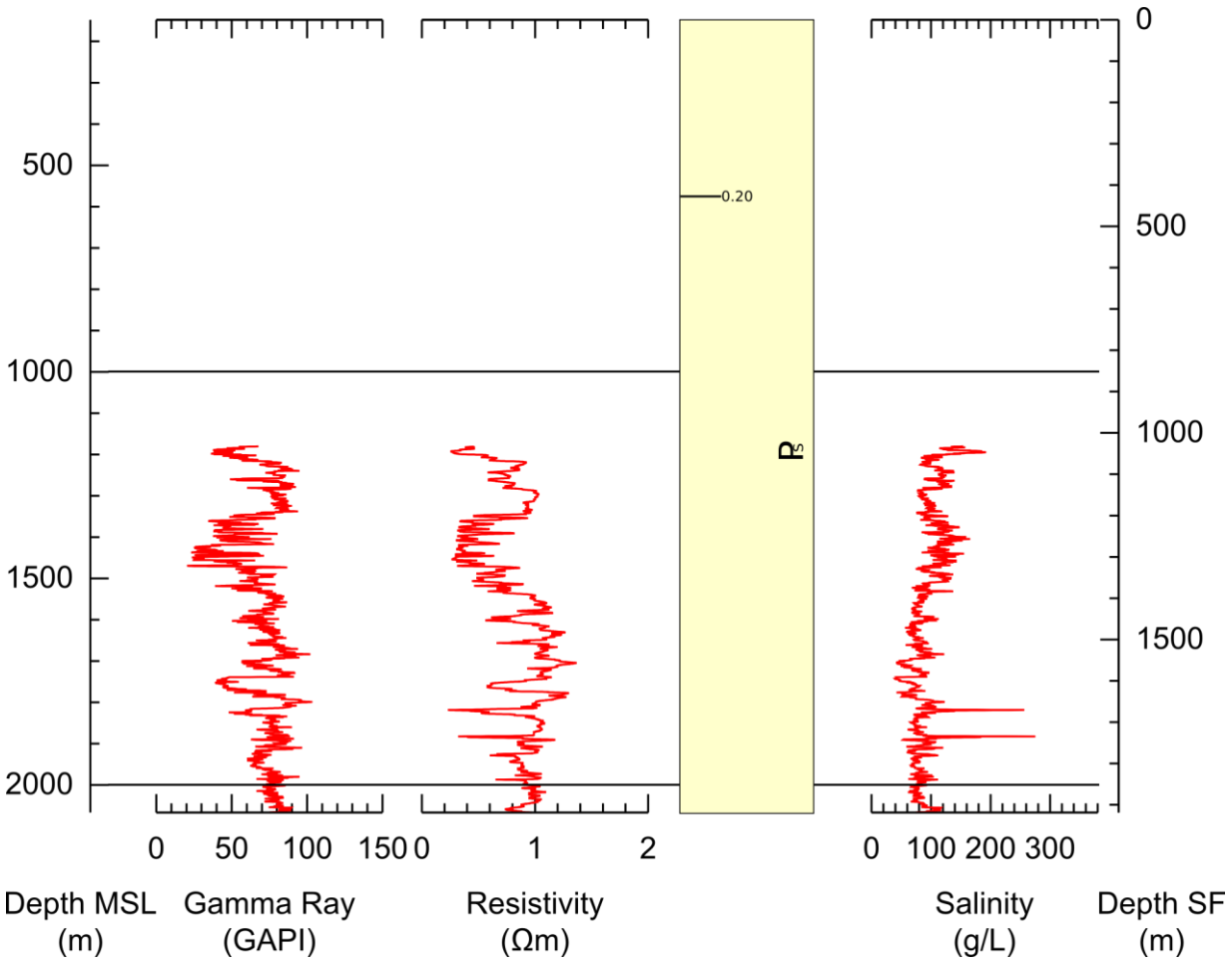

Garden Banks 127 (GB127)
Well API Number: 608074170200
Location: 27°52′31.1″N 91°59′11.6″W
Well Field: Chimichanga
Partners: Shell Offshore
Water Depth: 90 m
Shale Point: 140 GAPI
Sand Point: 60 GAPI
Resistivity: COND (Conductivity) inverted
Age: 17 nearby wells with paleodata: 1 from GB82, 1 from GB83, 7 from GB128, 4 from GB171, and 4 from GB172. Most age data adapted from 6807408200 (GB128).
Salt Depth: 3910-4348m from MSL

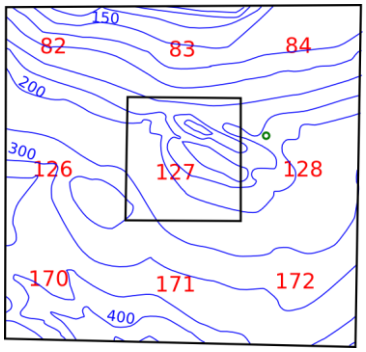

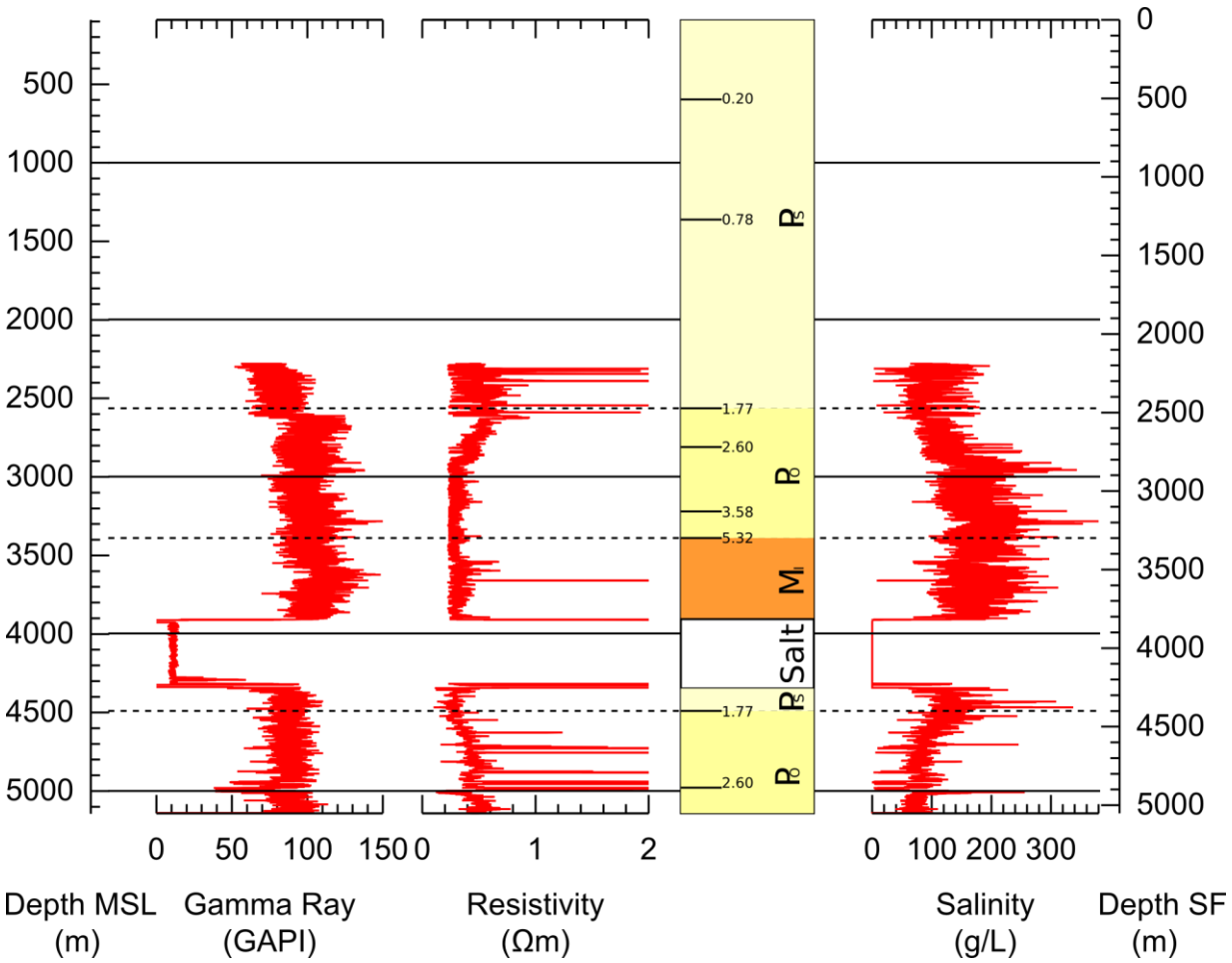

Garden Banks 215
Well Field: Conger
Partners: Amerada Hess
Two wells in this study
Age: 28 nearby wells with paleodata: 4 from 171, 3 from 172, 8 from 215, 3 from 216, 10 from 260. Most age data adapted from 608074081500 from GB215.

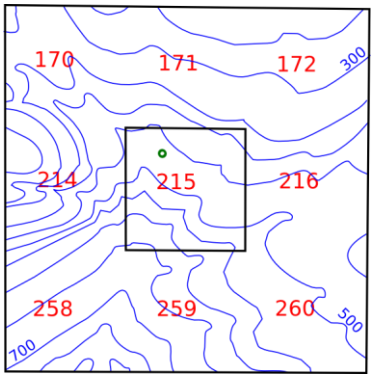

Shortname: GB215-0
Well API Number: 608074020100
Location: 27°47′34.2″N 92°1′56.7″W
Drill Date: 5/6/1999
Water Depth: 446 m
Shale Point: 130 GAPI
Sand Point: 60 GAPI
Resistivity: AT60ED (60in Array Resistivity)
Salt Depth: 5628-6030m from MSL

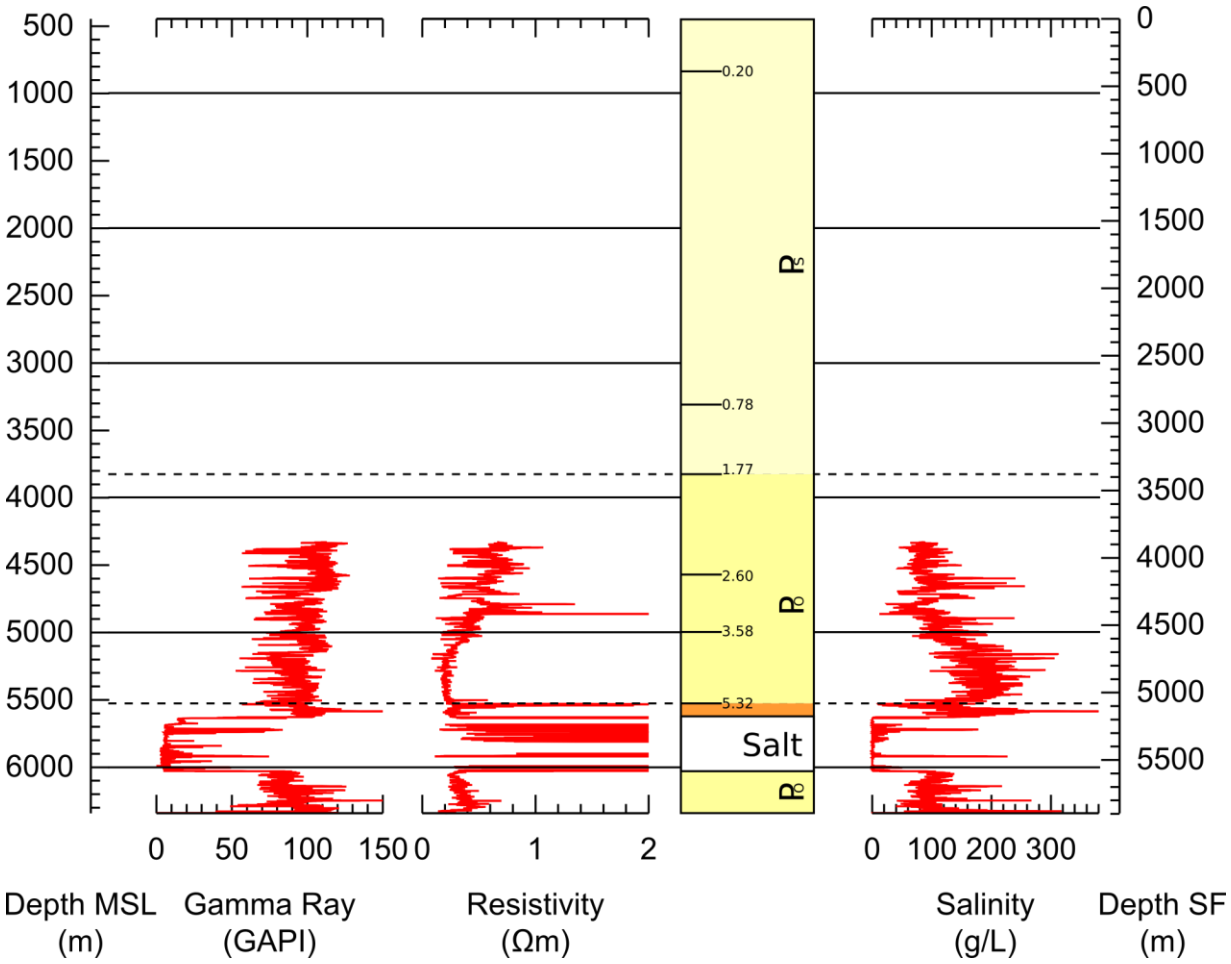

Shortname: GB215-1
Well API Number: 608074020101
Location: 27°47′34.0″N 92°1′56.7″W
Drill Date: 5/6/1999
Water Depth: 446 m
Shale Point: 105 GAPI
Sand Point: 40 GAPI
Resistivity: CILD (Conductivity) inverted
Salt Depth: 5628-6046m from MSL

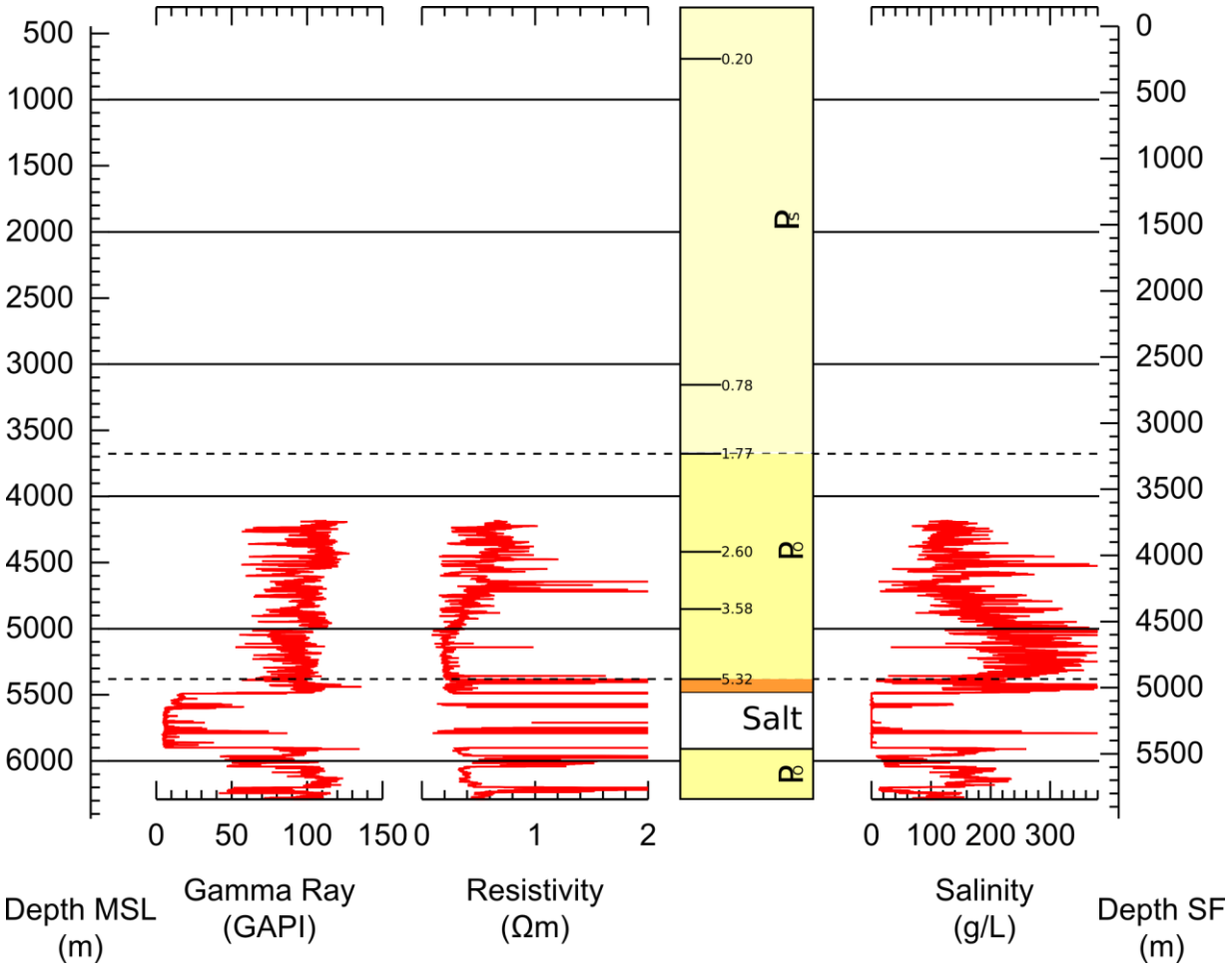

Garden Banks 253 (GB253)
Well API Number: 608074022502
Location: 27°42′56.8″N 92°18′9.9″W
Partners: Shell Offshore
Drill Date: 2/14/2001
Water Depth: 564 m
Shale Point: 125 GAPI
Sand Point: 45 GAPI
Resistivity: ILD (Deep resistivity)
Age: 8 nearby wells: 3 from GB208, 1 from GB253, 1 from GB254, and 3 from GB297. Most paleodata is from this well, but it was listed as in GB297.
Salt Depth: 5075-5646m from MSL, 5864-5985m from MSL

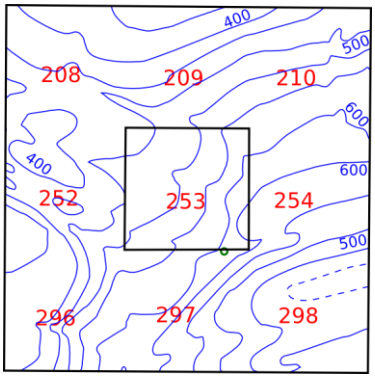

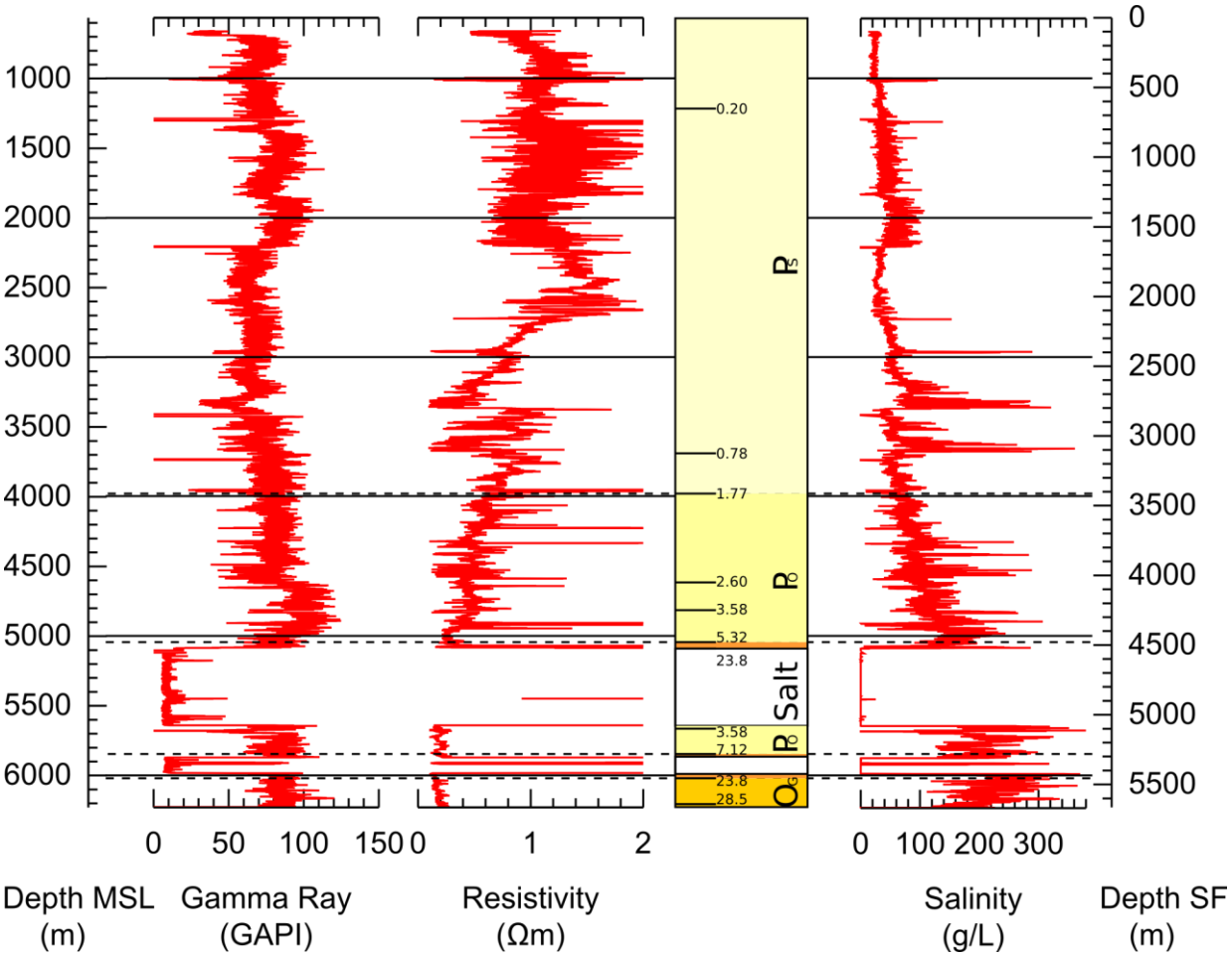

Garden Banks 272
Two wells in this study
Age: 3 nearby wells: 2 from 272, 1 from 273.

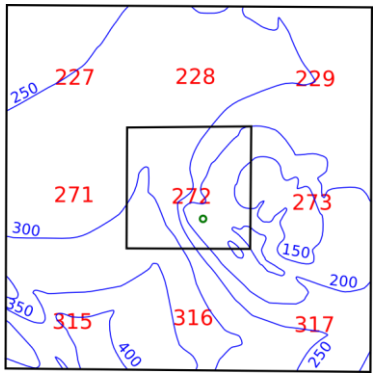

Shortname: GB272-0
Well API Number: 608074065600
Location: 27°41′4.1″N 93°32′9.5″W
Water Depth: 170m
Shale point: 110 GAPI
Sand point: 50 GAPI
Resistivity: ILD (Deep resistivity)
Age: From this well.
Salt Depth: 778m from MSL

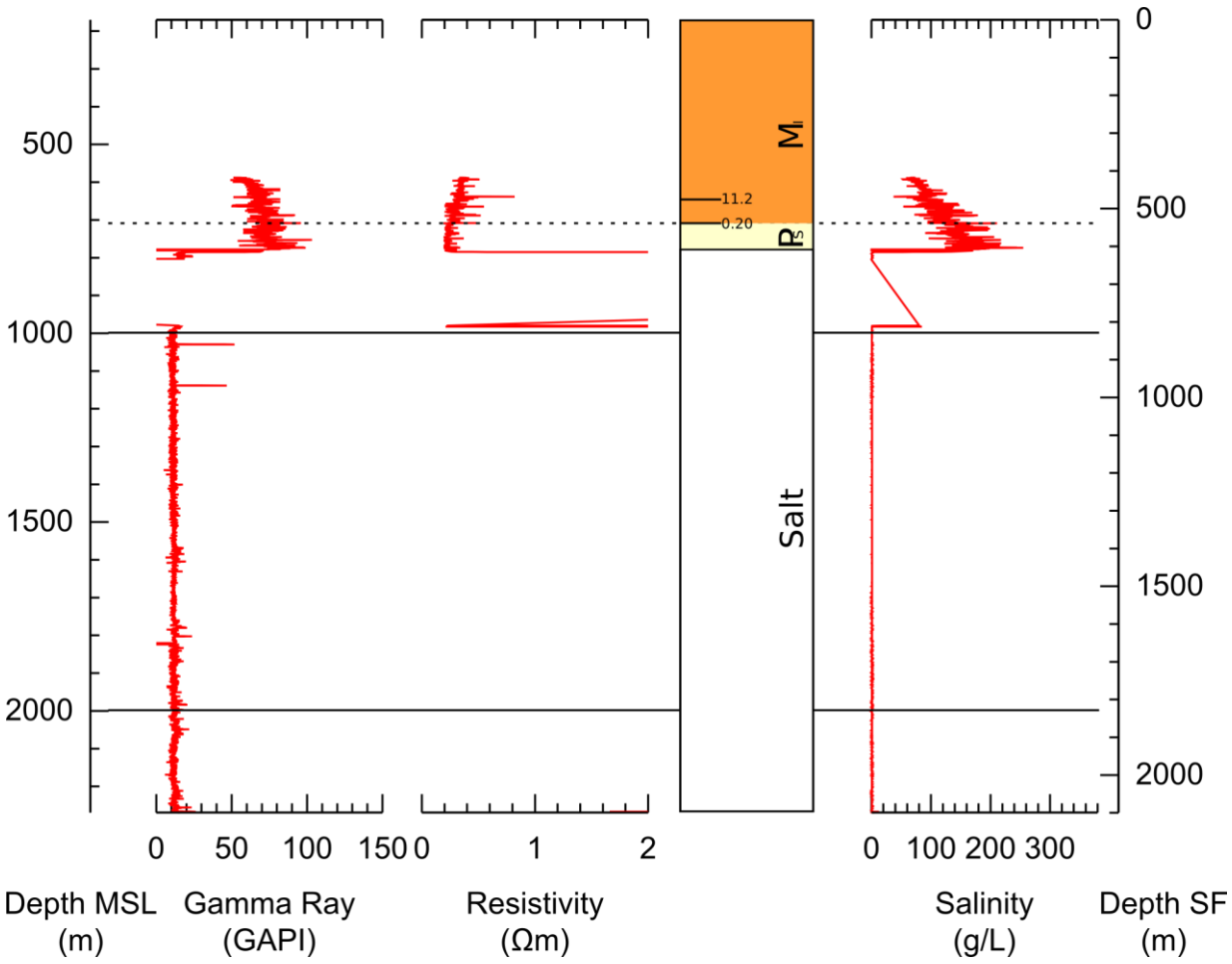

Shortname: GB272-1
Well API Number: 608074065601
Water Depth: 170m
Shale Point: 120 GAPI
Sand Point: 40 GAPI
Resistivity: ILD (Deep resistivity)
Age: From this well and GB272-0.
Salt Depth: 774-2968m from MSL

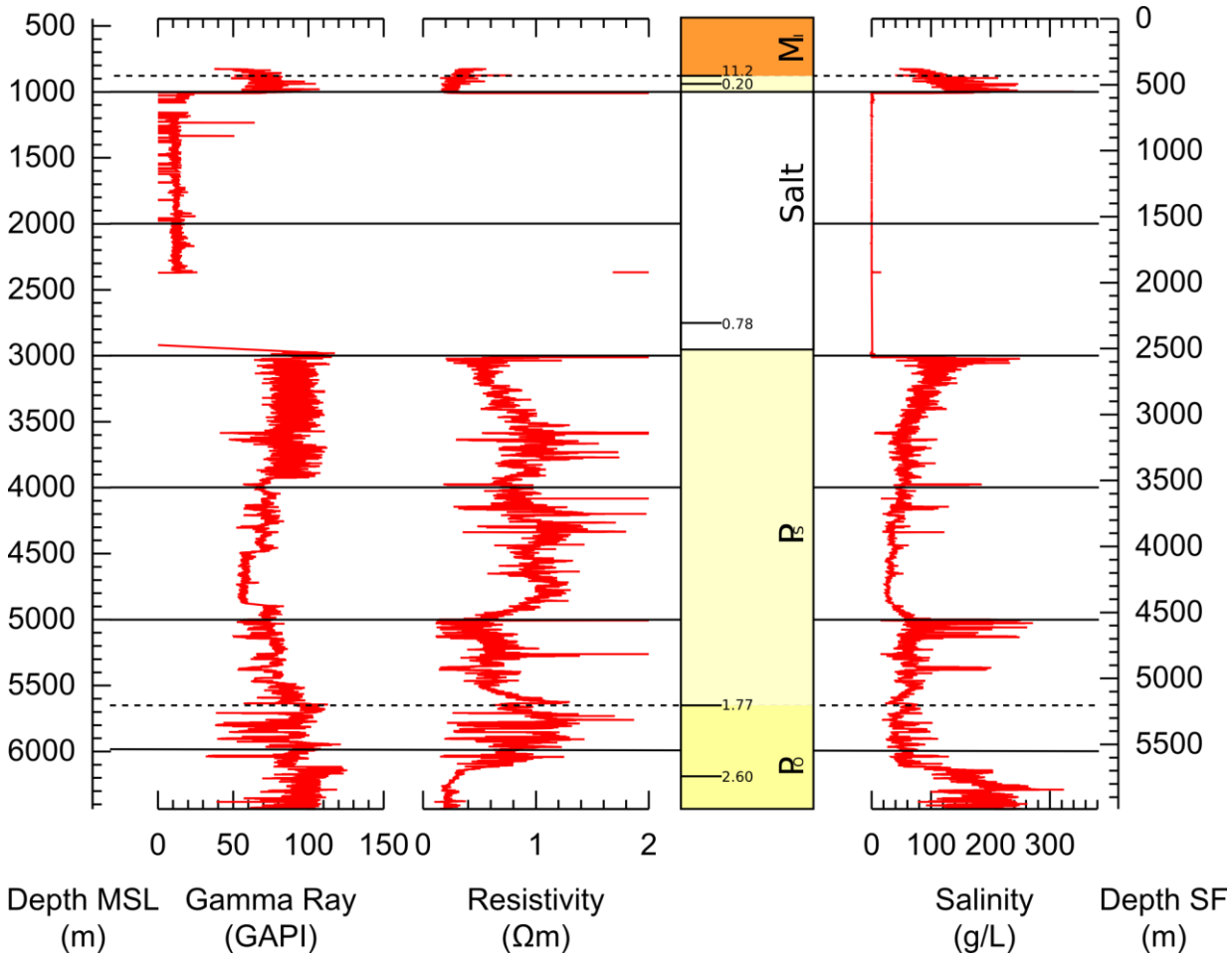

Green Canyon 98
Partners: Conoco Phillips
Two wells in this study
Age: 17 nearby wells: 5 from 53, 6 from 97, 3 from 98, 1 from 142, 2 from 143. Depth compiled from GC98-0, GC98-1, and 608115006300.

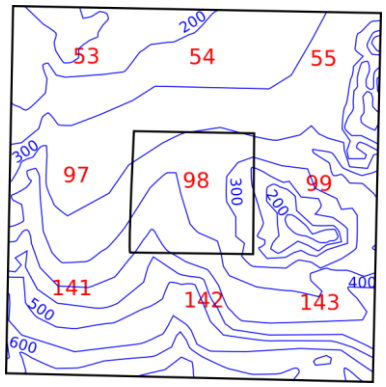

Shortname: GC98-0
Well API Number: 608115001500
Water Depth: 260m
Shale Point: 80 GAPI
Sand Point: 40 GAPI
Resistivity: ILD (Deep resistivity)
Salt Depth: 2350m from MSL

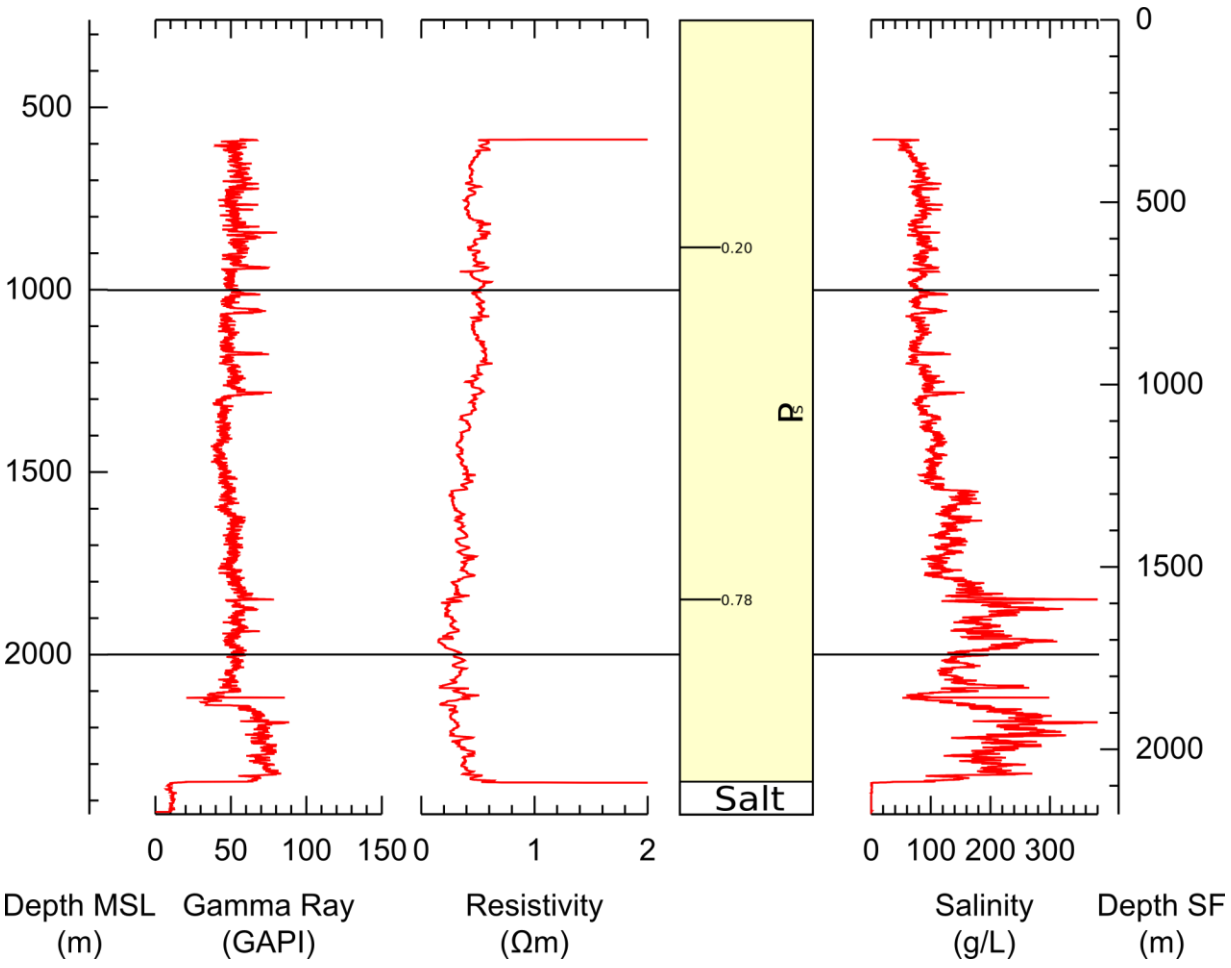

Shortname: GC98-1
Well API Number: 608115001501
Drill Date: 5/27/1984
Water Depth: 260m
Resistivity: No usable resistivity log
Salt Depth: 3168-3589m from MSL

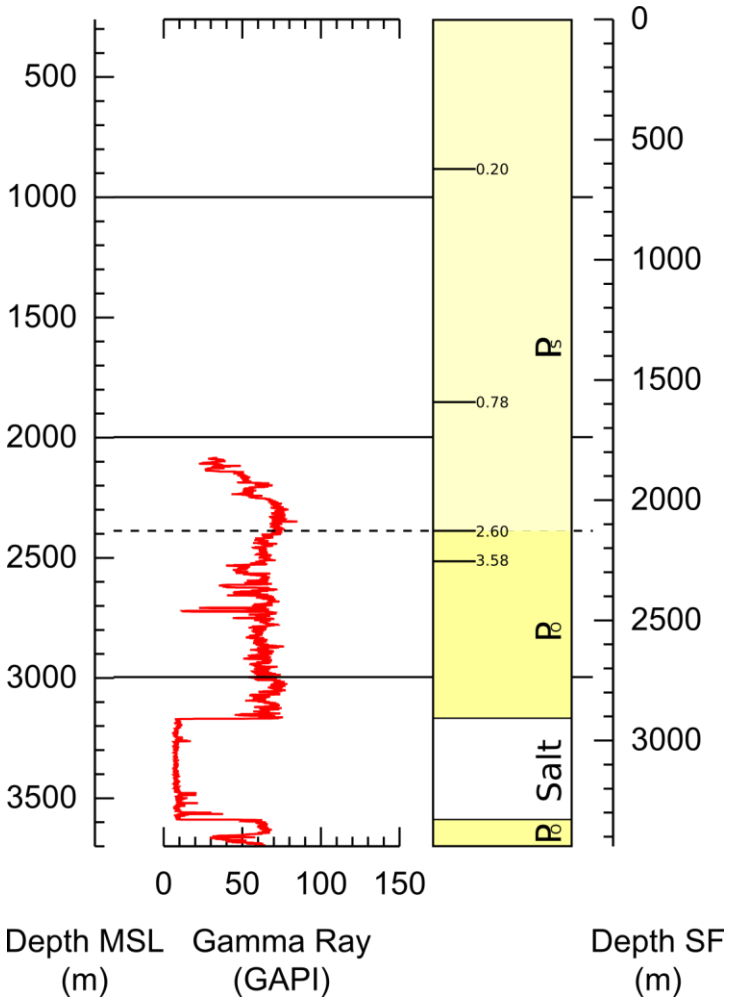

Green Canyon 184 (GB184)
Fieldname: Jolliet
Well API Number: 608115006200
Partners: Conoco Phillips
Drill Date: 9/8/1999
Water Depth: 536m
Shale Point: 80 GAPI
Sand Point: 30 GAPI
Resistivity: CIDPED + CIDPED (Conductivity) inverted
Age: 18 nearby records: 1 from 183, 11 from 184, 1 from 227, 5 from 228. Interpretation from 608115002800 from 228.
Salt Depth: Was not logged, assumed to be between 2412-2483m from MSL

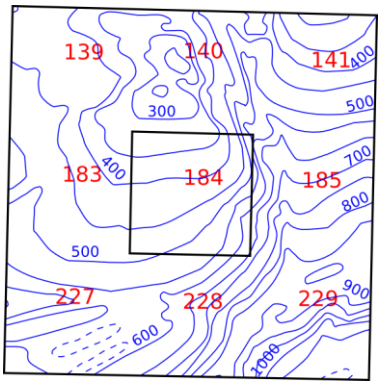

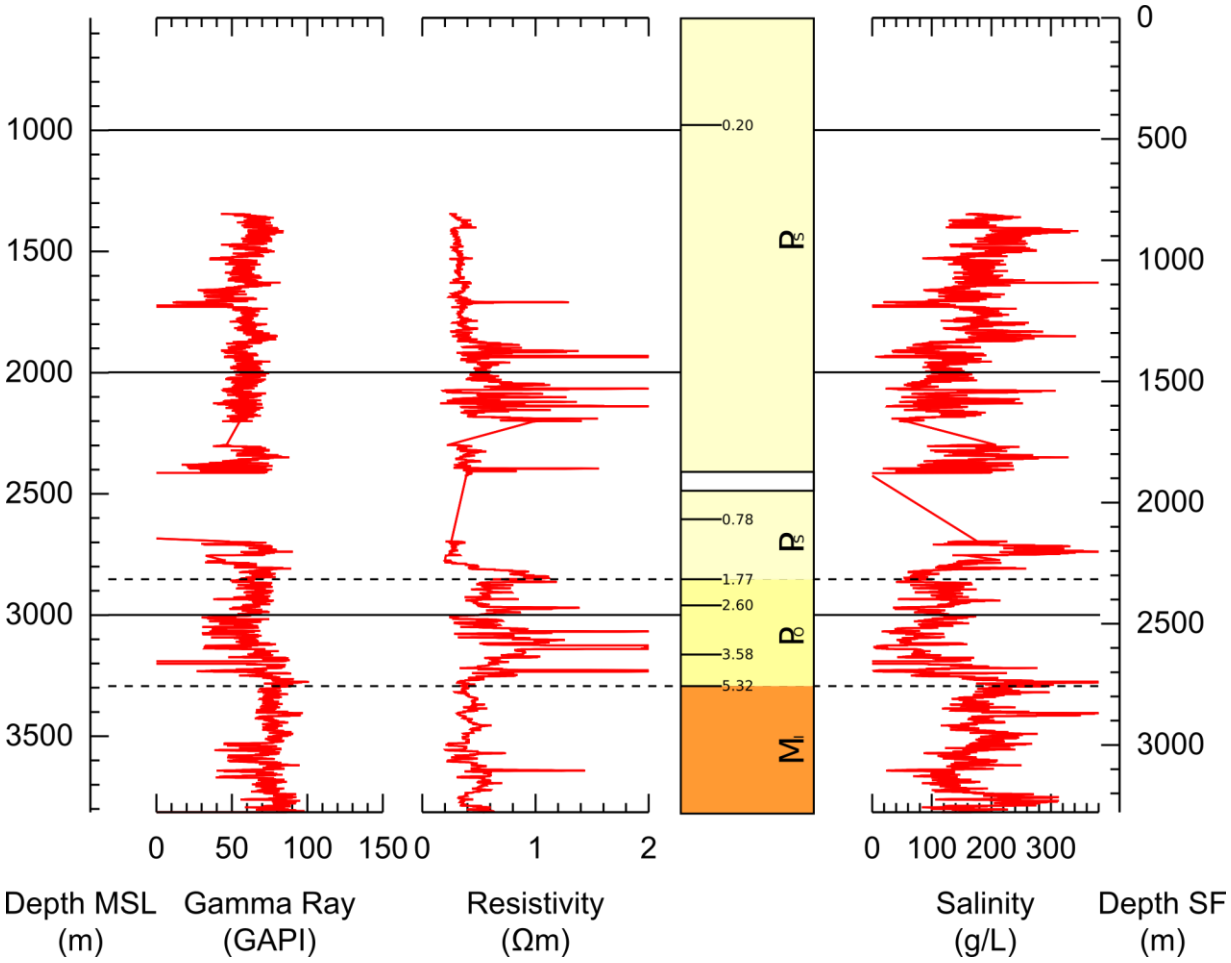

Green Canyon 563
Fieldname: K2
Partners: Eni Petroleum
Three wells in this study
Age: 11 nearby wells: 2 from 562, 3 from 563, 6 from 608

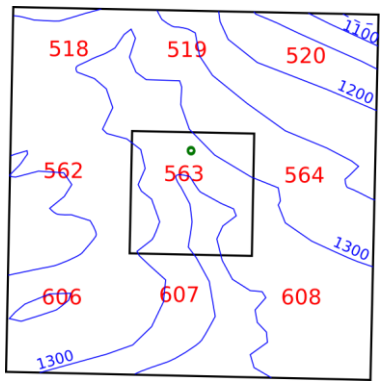

Shortname: GC563-0
Well API Number: 608114024900
Location: 27°25′14.0″N 90°13′18.8″W
Drill Date: 9/8/1999
Water Depth: 1263m
Shale Point: 120 GAPI
Sand Point: 50 GAPI
Resistivity: PSR (Phase Shift Resistivity)
Age: From this well.
Salt Depth: 5493-5534m from MSL, 5642-6426m from MSL

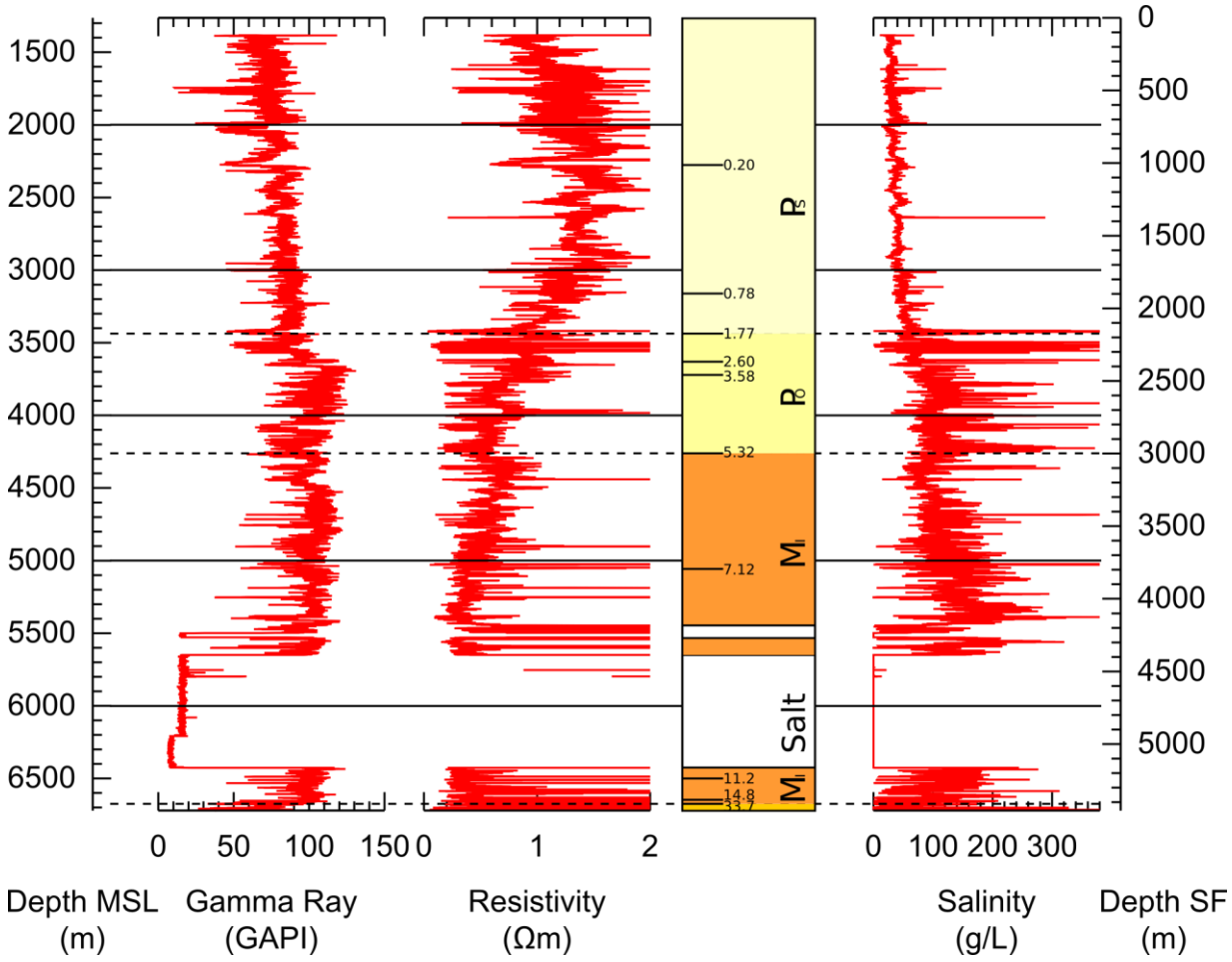

Shortname: GC563-1
Well API Number: 608114024901
Location: 27°25′14.4″N 90°13′18.8″W
Drill Date: 5/16/200
Water Depth: 1263m
Shale Point: 90 GAPI
Sand Point: 40 GAPI
Resistivity:
Age: From this well, and shallow ages are from GC563-0.
Salt Depth: 6185-6657m from MSL

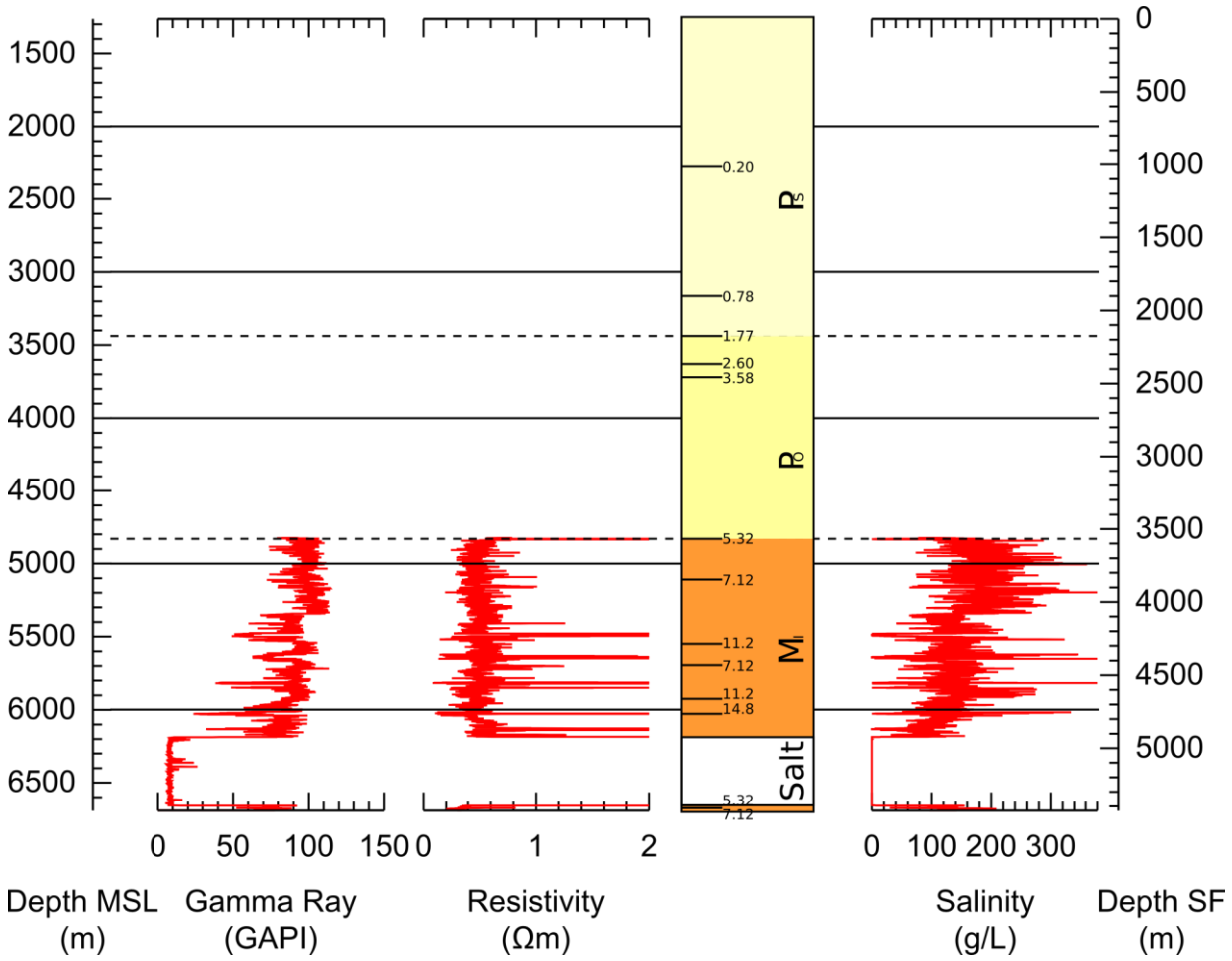

Shortname: GC563-2
Well API Number: 608114024902
Location: 27°25′14.5″N 90°13′18.8″W
Shale Point: 90 GAPI
Sand Point: 30 GAPI
Resistivity: P28H (ARC5 Phase Shift Resistivity 2)
Age: Same as GC563-1.
Salt Depth: 6129m from MSL

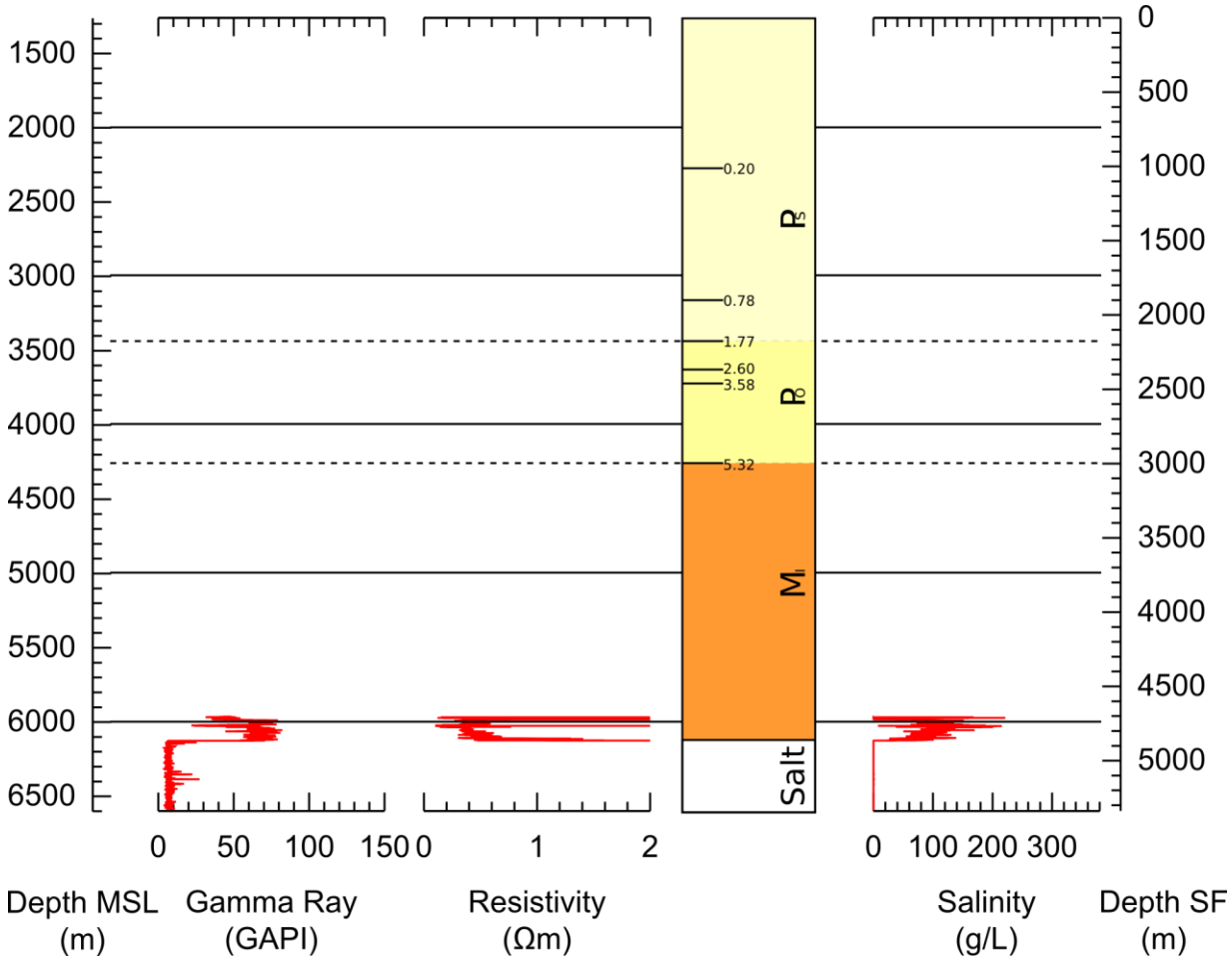

Mississippi Canyon 167 (MC167)
Fieldname: Mica
Well API Number: 608174056900
Location: 28°47′42.4″N 88°13′53.5″W
Partners: Exxon Mobil
Drill Date: 7/12/2001
Water Depth: 1328 m
Shale Point: 120 GAPI
Sand Point: 40 GAPI
Resistivity: CONDED (Conductivity) inverted
Age: From this well, (identified as in MC211 in paleoheaders).
Four total wells identified as MC211. No age data available above salt.
Salt: 1741-2893m from MSL

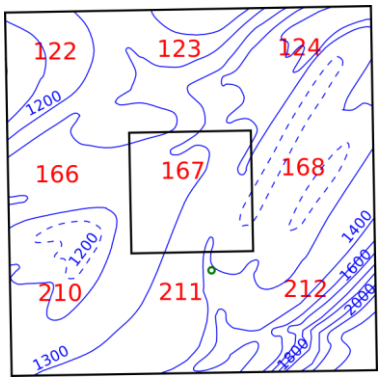

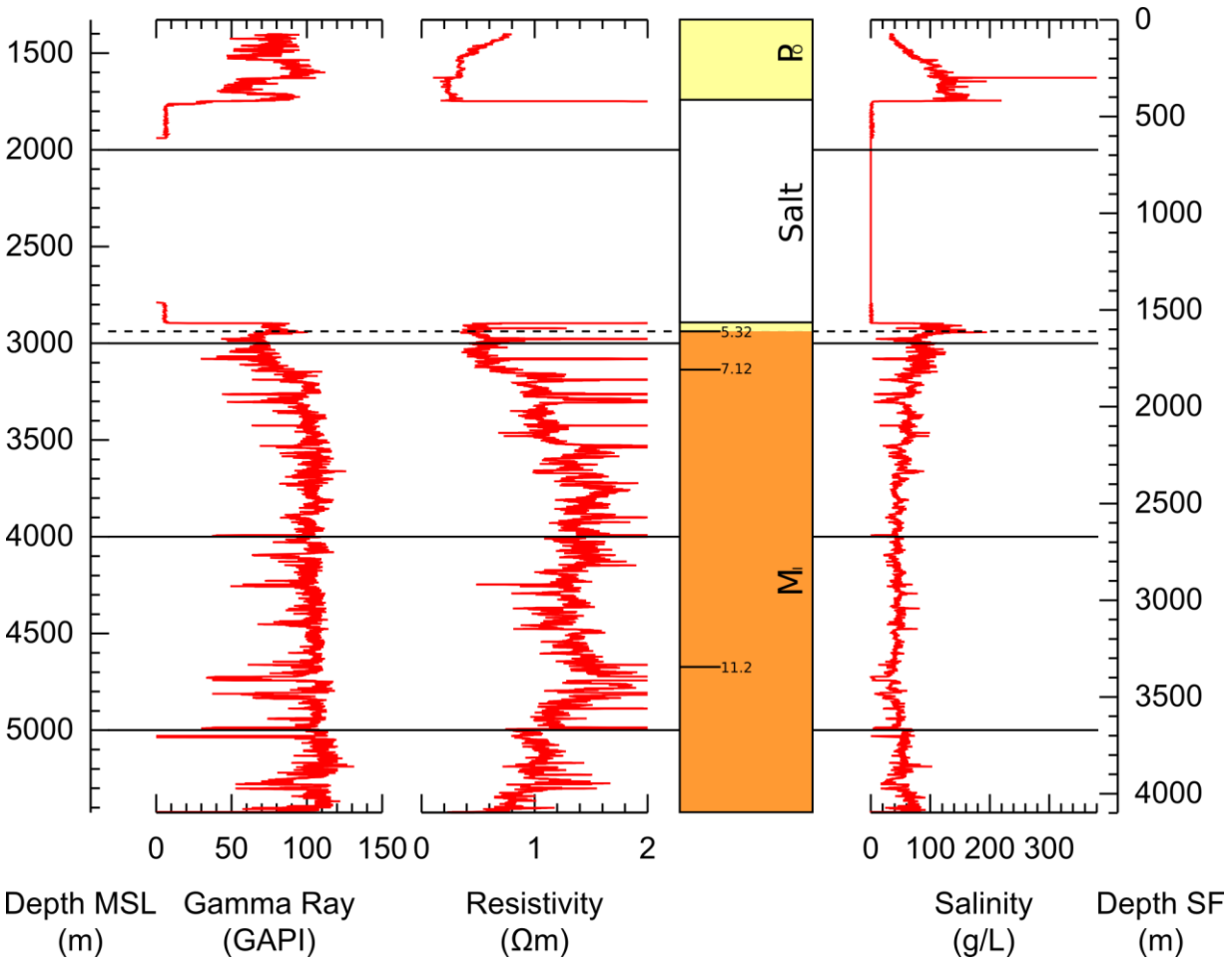

Mississippi Canyon 292
Fieldname: Gemini
Partners: Chevron
Two wells in this study
Age: 12 nearby wells: 2 from 247, 3 from 248, 1 from 291, 6 from 292. Ages interpreted from 608174083300 in MC292.

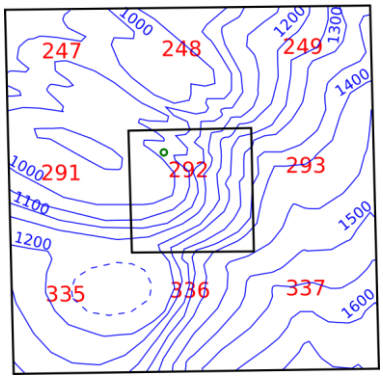

Shortname: MC292-0
Well API Number: 608174083200
Location: 28°42′12.6″N 88°35′44.2″W
Drill Date: 4/15/1999
Water Depth: 1060m
Shale Point: 120 GAPI
Sand Point: 40 GAPI
Resistivity: ATRED (Attenuation Resistivity) inverted
Salt Depth: 2092-3016m from MSL

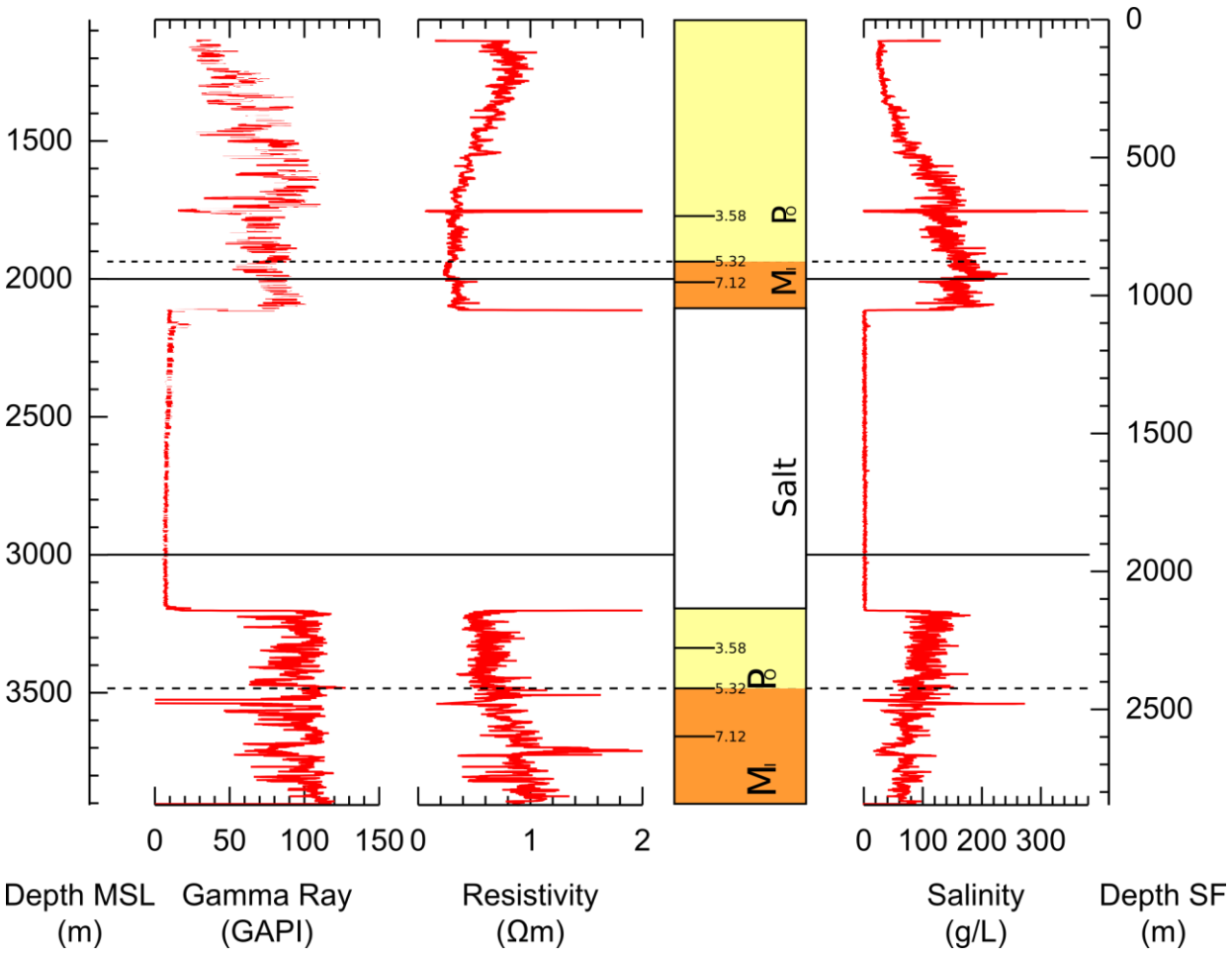

Shortname: MC292-1
Well API Number: 608174083201
Water depth: 1060m
Shale Point: 140 GAPI
Sand Point: 35 GAPI
Resistivity: AT90ED (90in Array Induction Resistivity)
Salt Depth: not in logged section, assumed to be 2092-3016m from MSL, logged in MC292-0

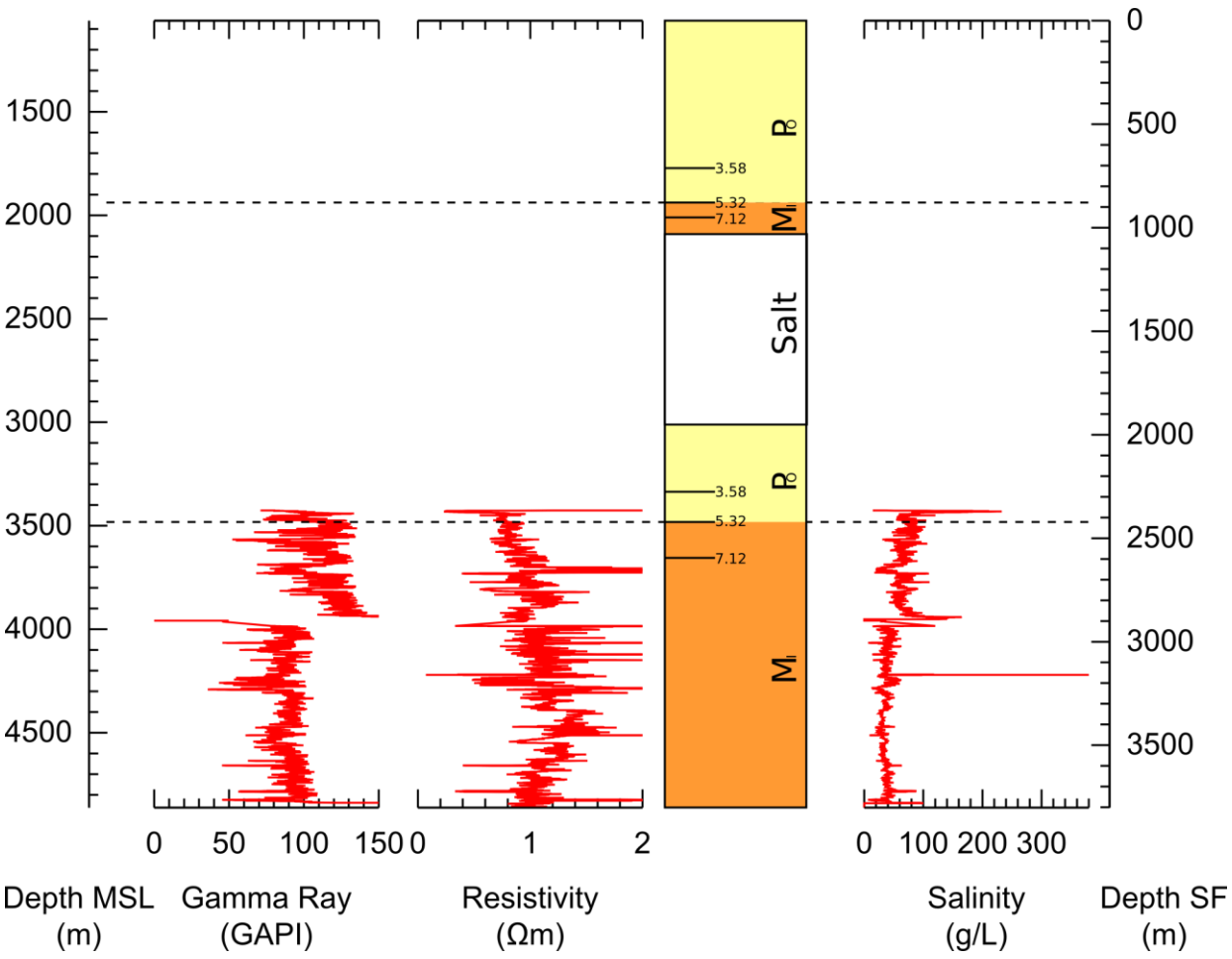

South Marsh Island 200 (SM 200)
Well API Number: 177084064600
Partners: Diamond Shamrock
Drill Date: 1/29/1986
Water Depth: 145m
Shale Point: 100 GAPI
Sand Point: 40 GAPI
Resistivity: ILD (Deep induction resistivity)
Age: From this well. 5 nearby wells: 2 from SM196, 1 from SM 198, 1 from GB80, 1 from GB82
Salt Depth: 2670-3111m from MSL

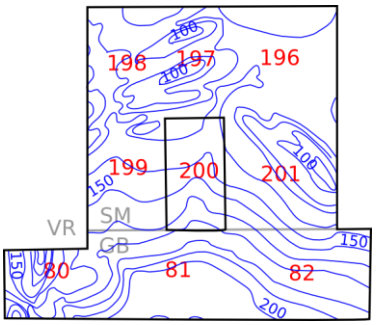

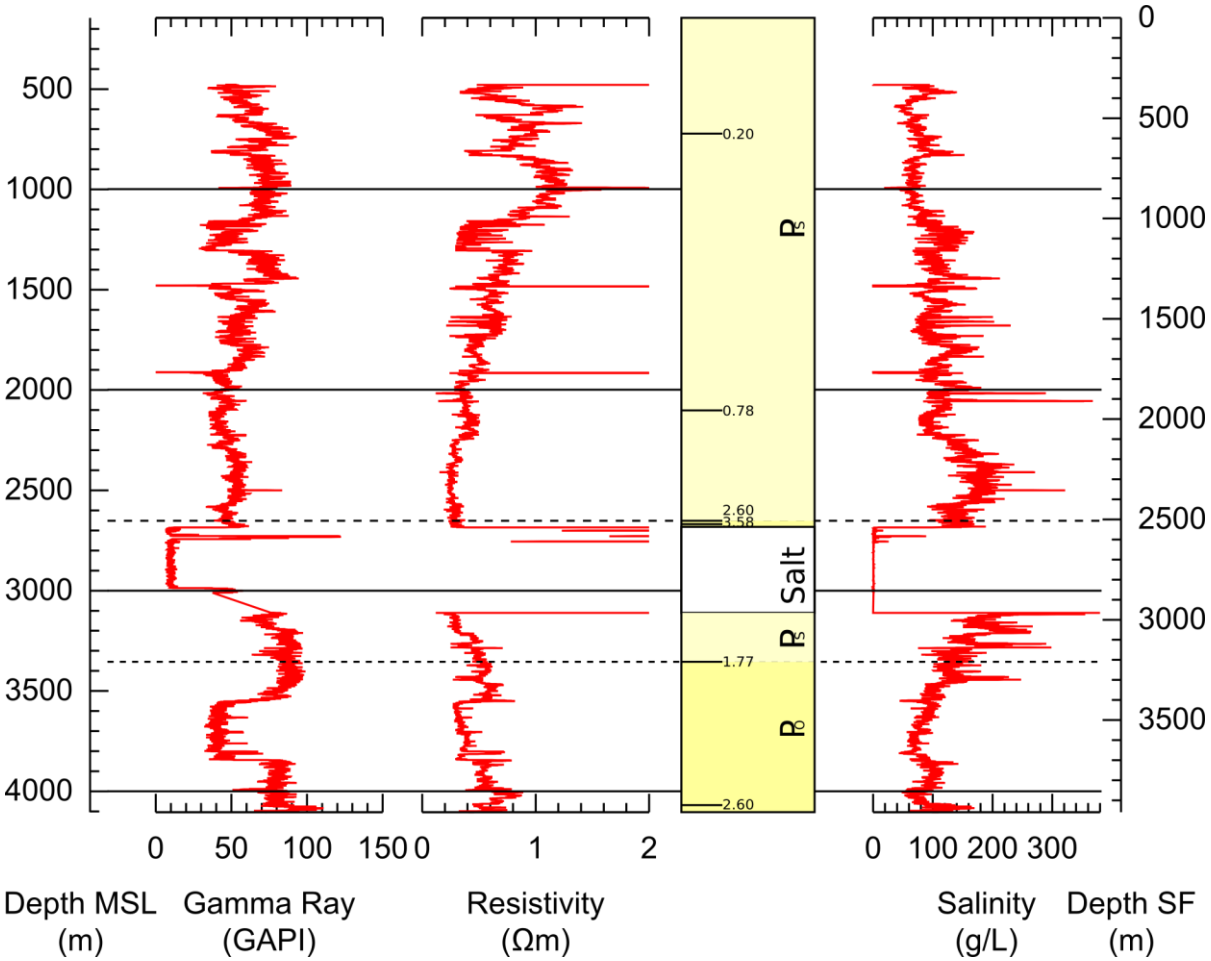

APPENDIX D: MODELING RESULTS

Included here are the biostratigraphic columns, and the best fit diffusion curves (green) both above and below salt. The results of the Basin2 modeling are also displayed (blue) and the calculated salinities (see Appendix C) are in black.

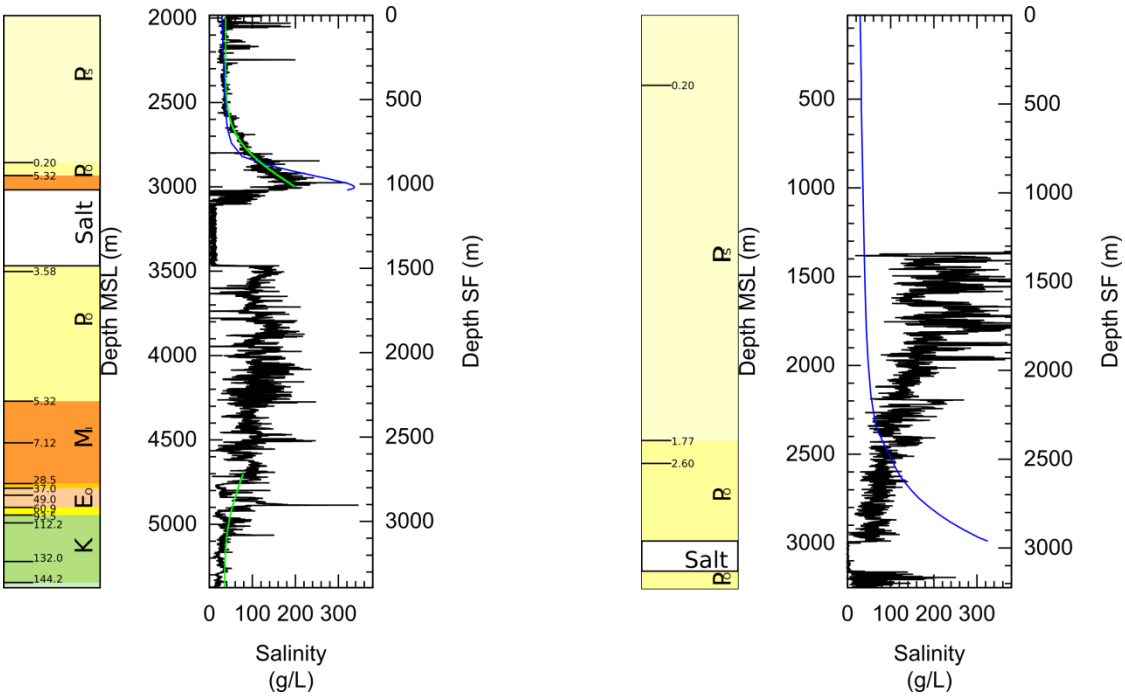

AT26 on left, EC185 on right.

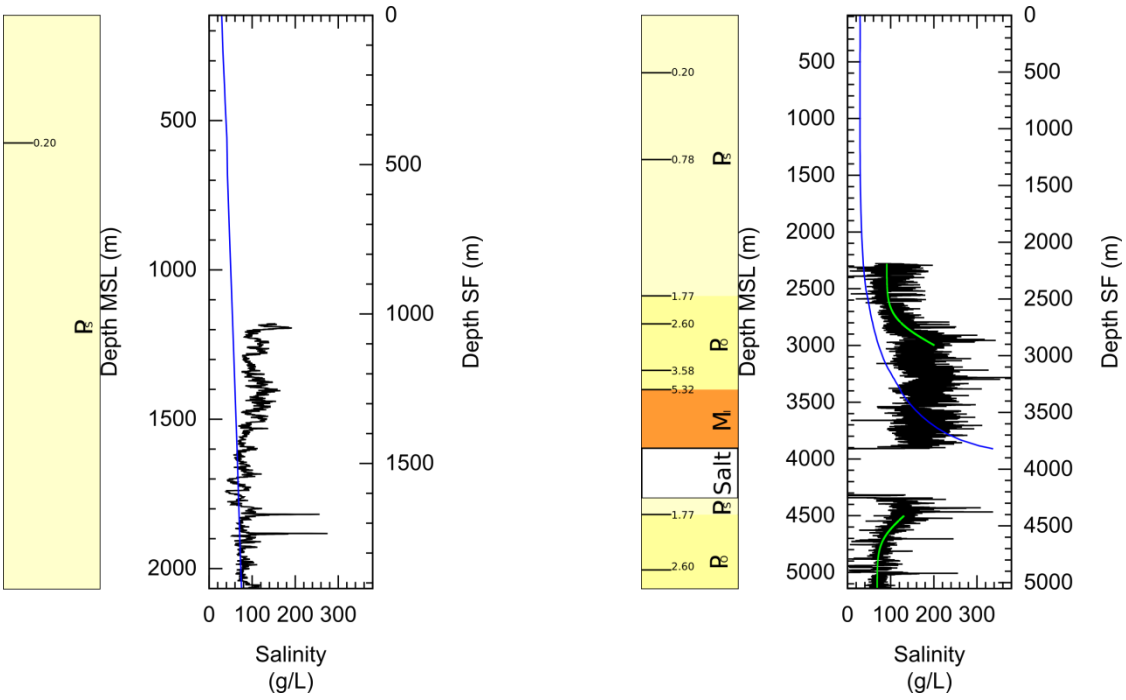

EI346 upper left, GB127 upper right, GB215-0 lower left, GB215-1 lower right.

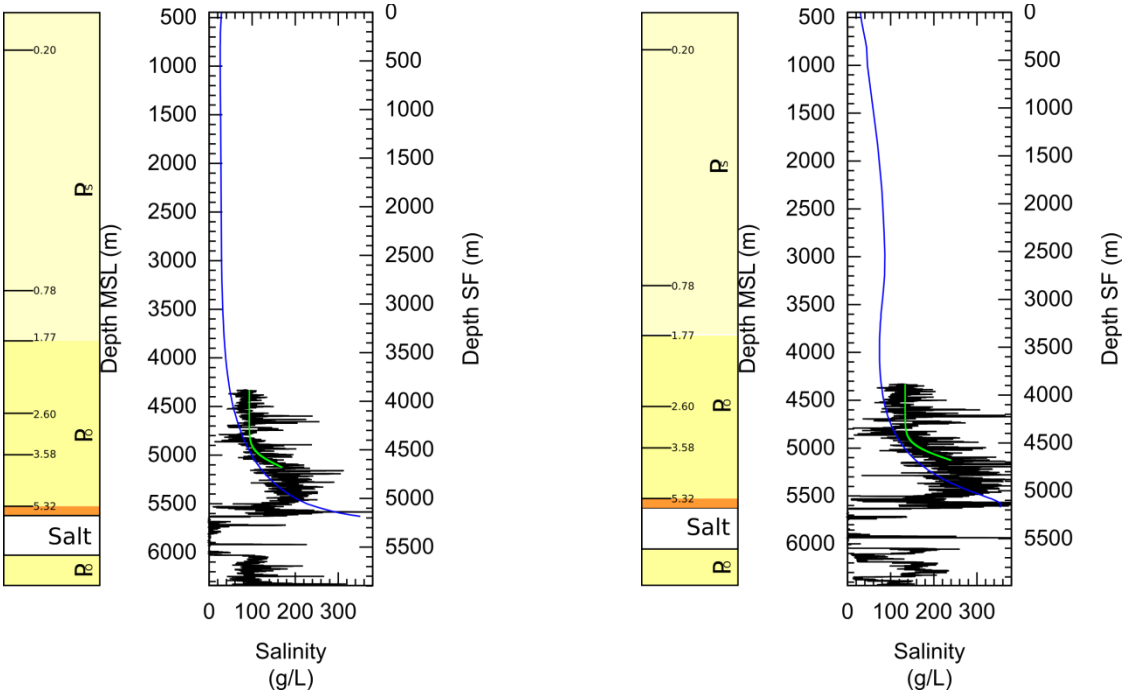

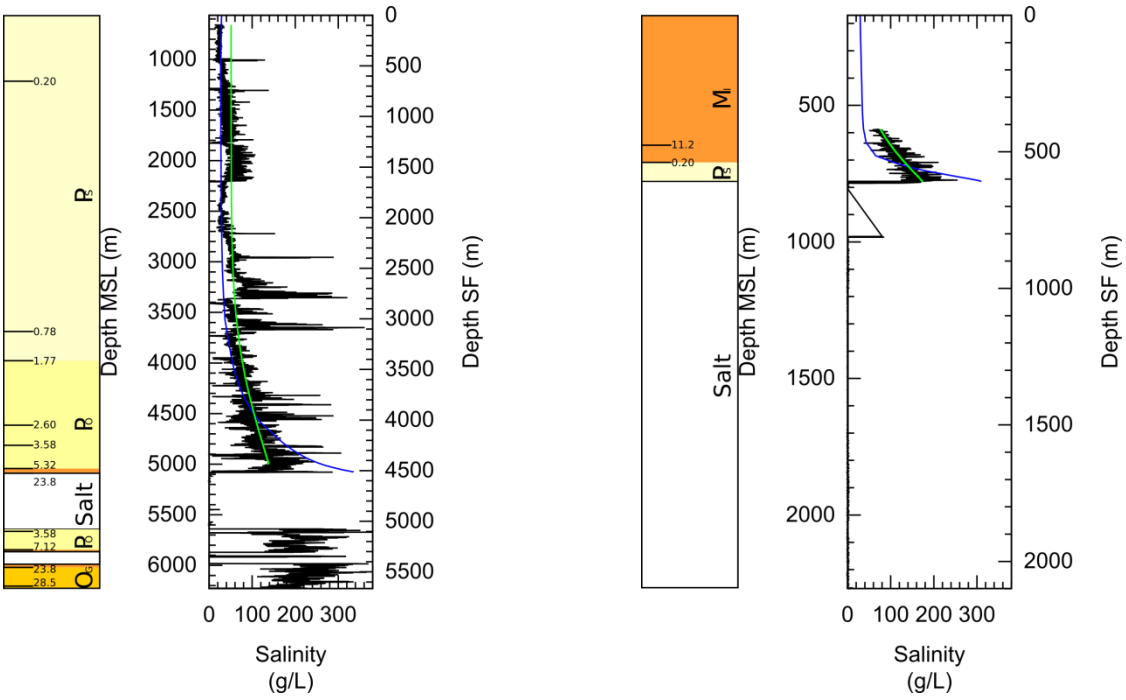

B253 upper left, GB272 upper right, GB272-1 lower left, GC98-0 lower right. GC98-1 not included.

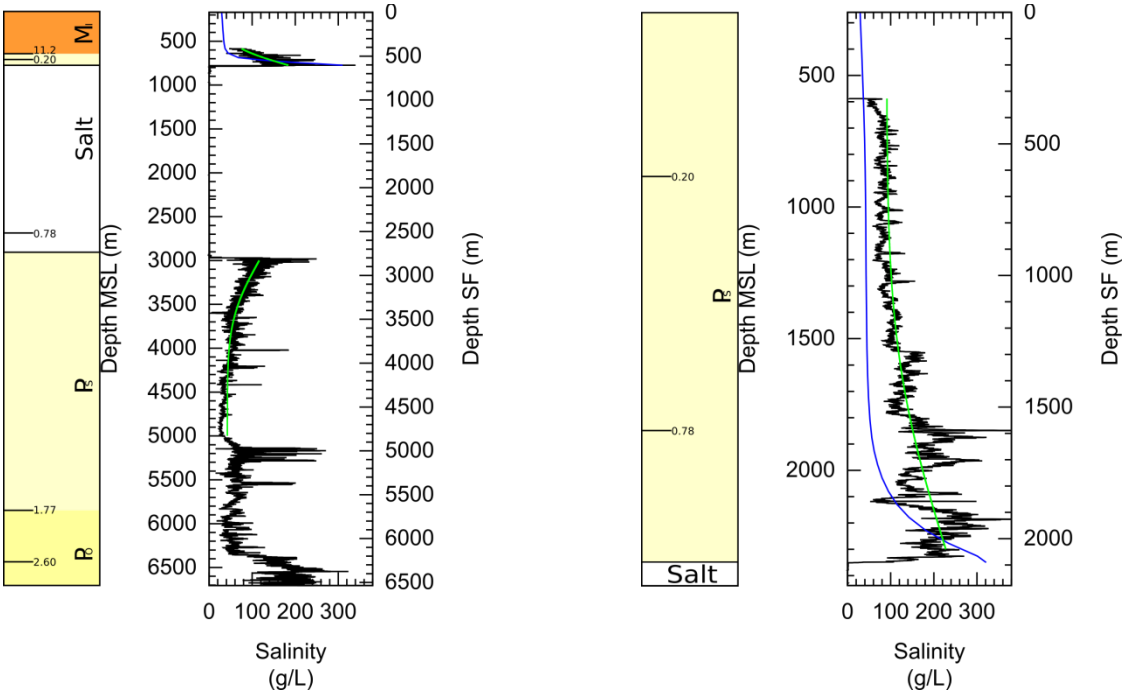

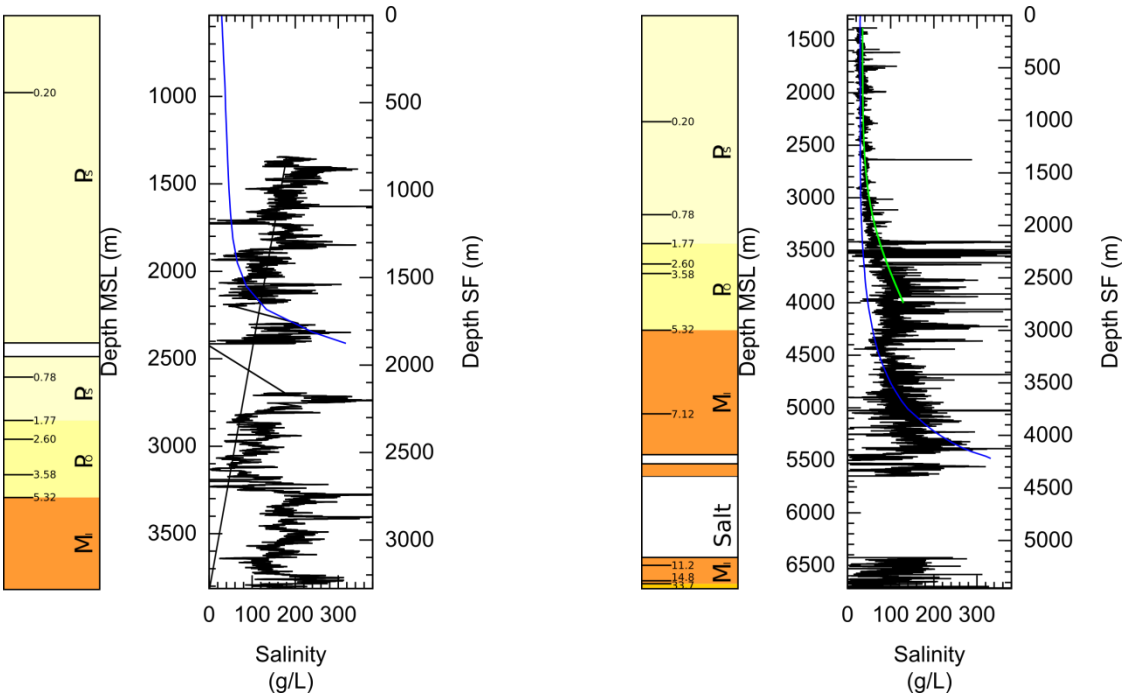

GC184 upper left, GC563-0 upper right, GC563-1 lower left, GC563-2 lower right.

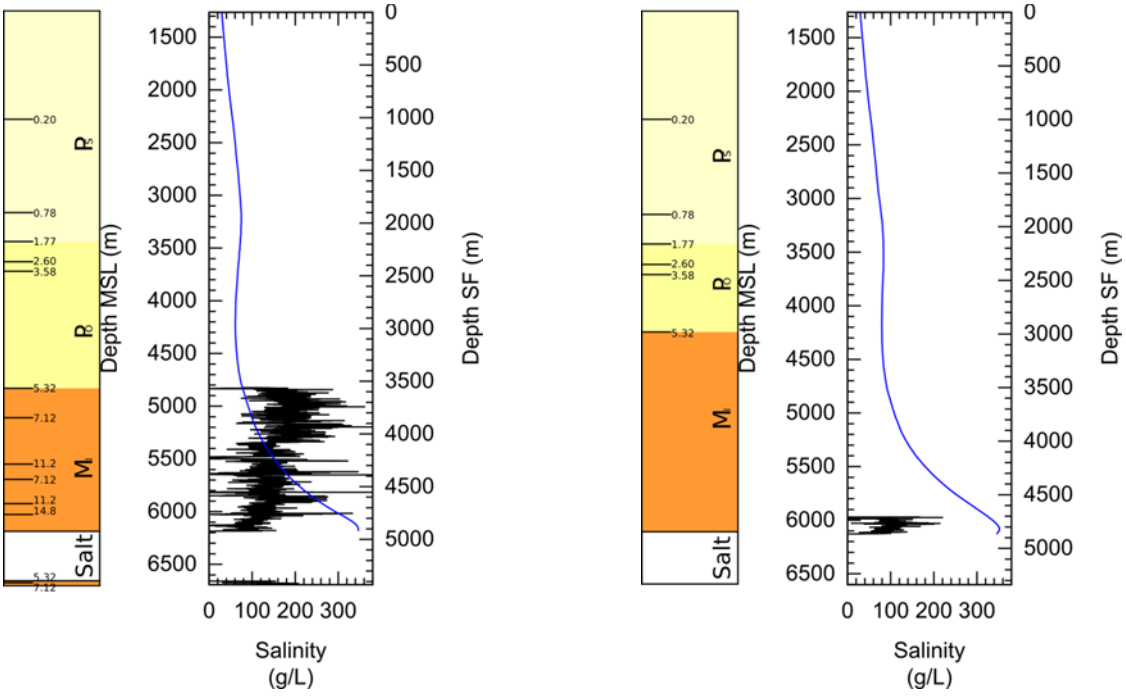

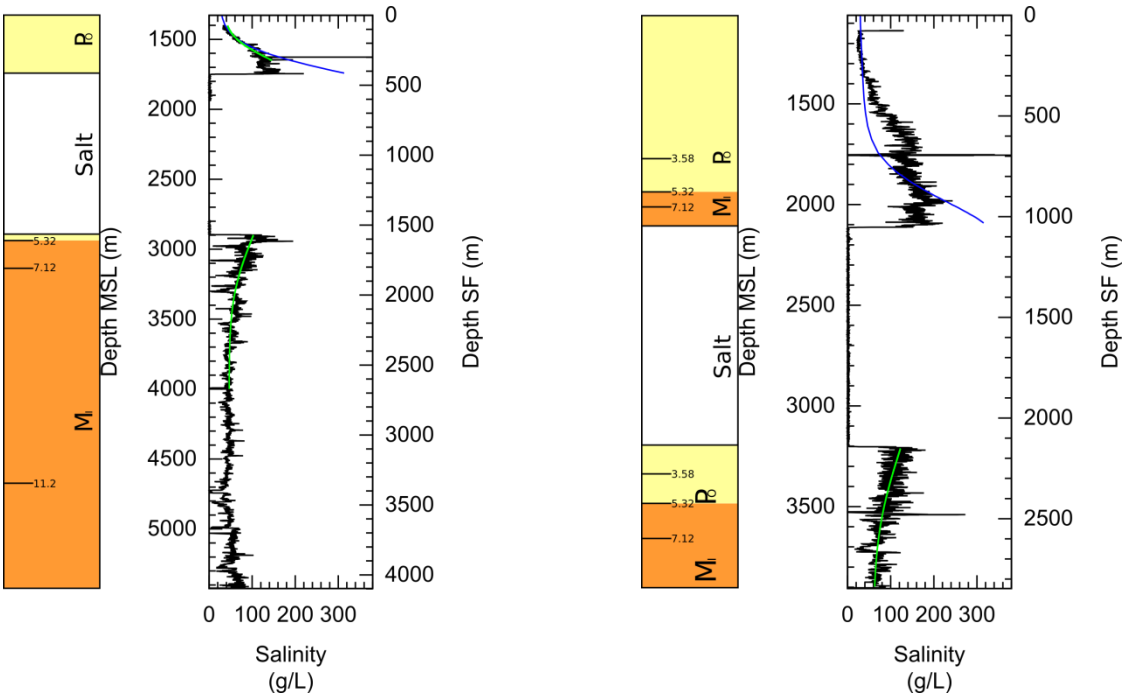

MC167 upper left, MC292-0 upper right, MC292-1 lower left, SM200 lower right.

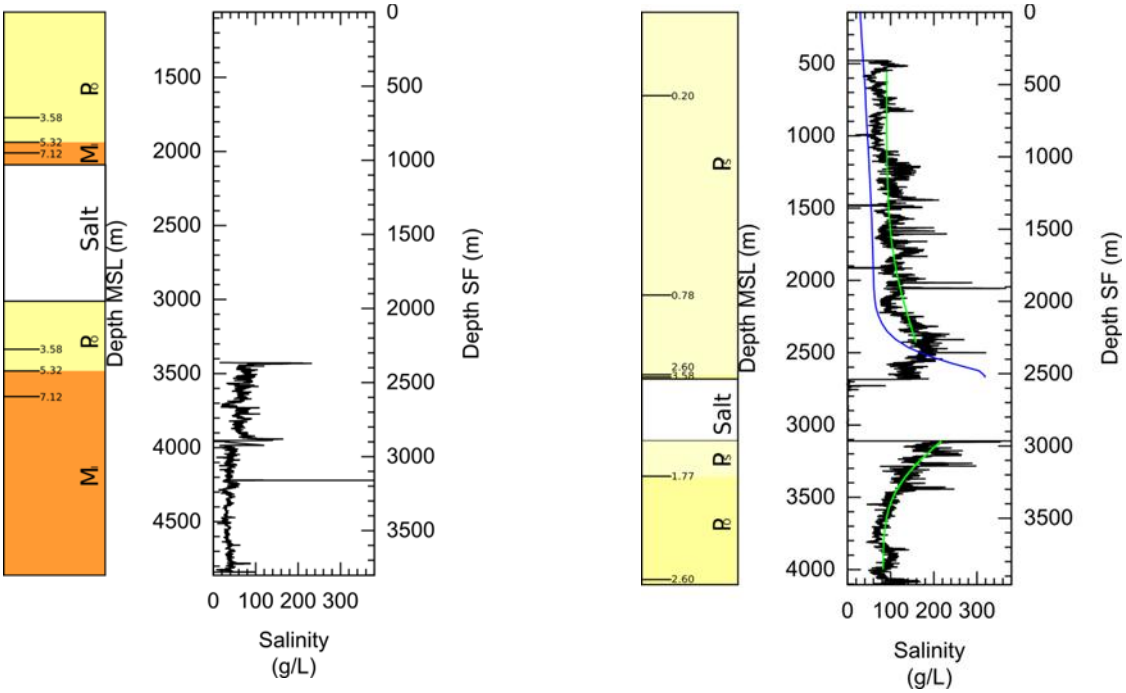

APPENDIX E: BINNING MODELING RESULTS

Included here are graphs showing the results of the binning modeling, with average salinities as black squares, and modeled salities as blue triangles.

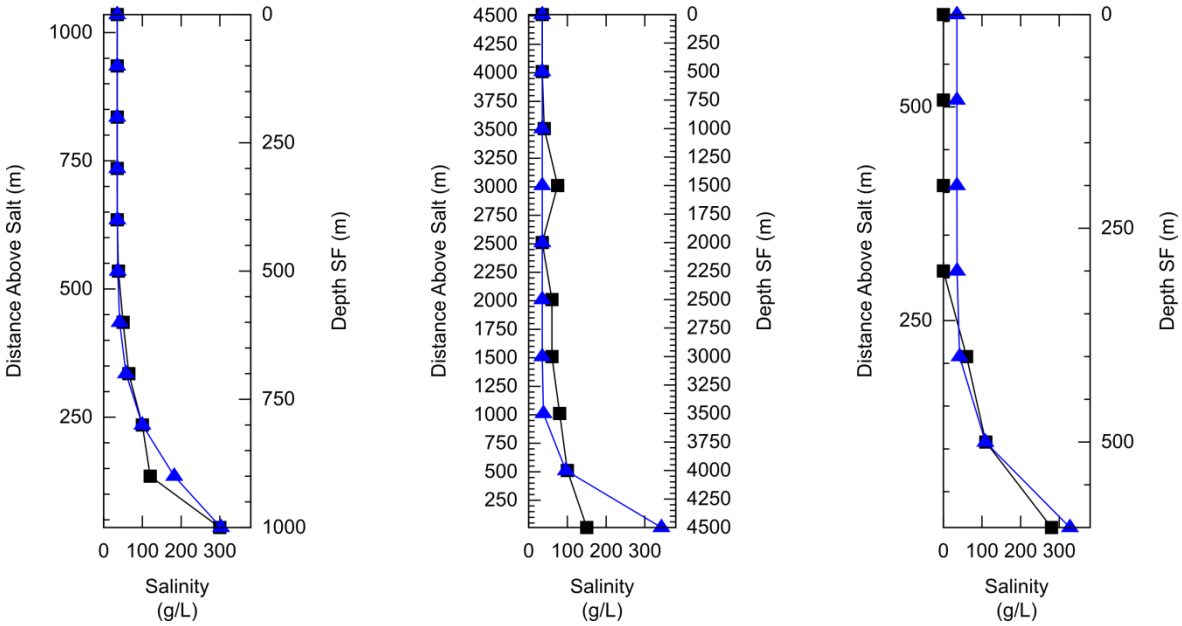

Above, from left: AT26, GB253, GB272-0

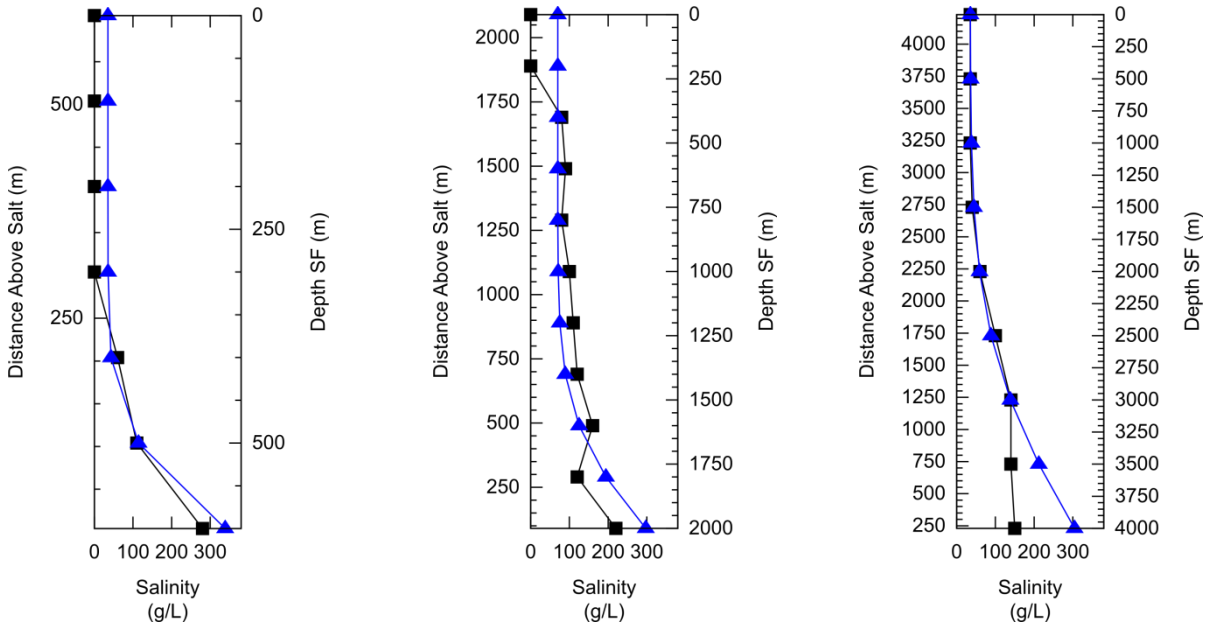

Above, from left: GB272-1, GC98-0, GC563; Lower, from left: MC167, SM200

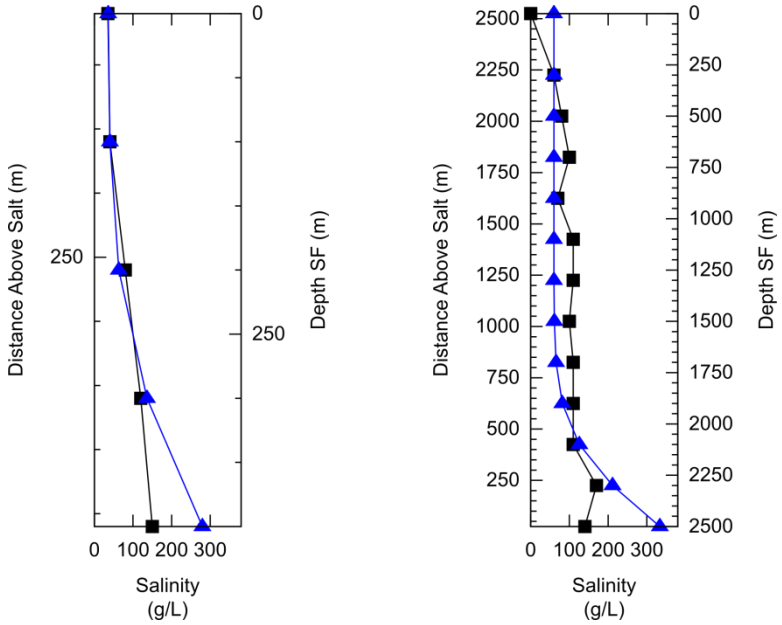

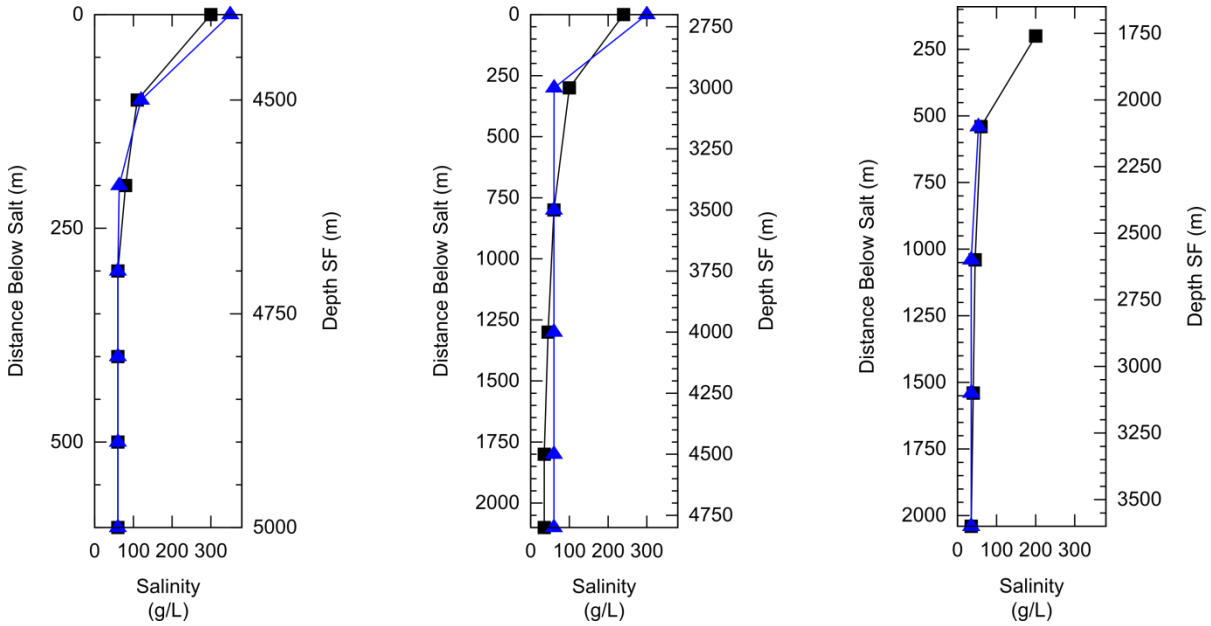

Above, from left: GB127, GB272-1,MC167; Lower, from left: MC167, SM200

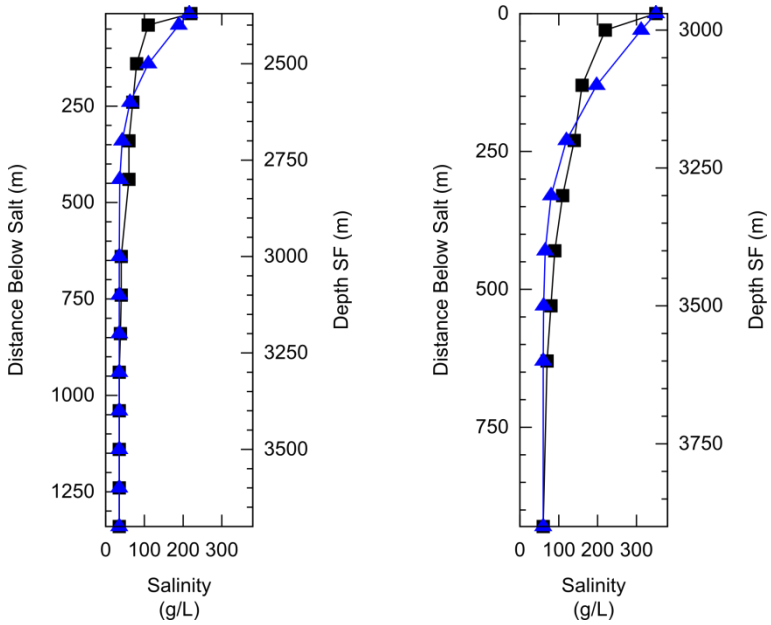

APPENDIX F: EXAMPLE BASIN2 INPUT FILE

The method used to determine the parameters for Basin2 modeling is described in the methods section. Included here is an example an input file for the site AT26 that lists all of the parameters used in the modeling in the study. In Basin2, comments which is text that is not interpreted, are indicated by having an number sign "#" in front of them.

```
passes = 5              #Indicates how many iterations are used for each time-step.
nx = 1                  #Forces a 1-Dimensional Model.
min_nodes = 10          #Minimum number of elements per stratigraphic unit.
water_depth = 1982.724 m    #Depth of water, calculated from the well log header.
start = -23.8 m.y.      #Simulation start time, calculated from the paleodata.

# The bottom unit in all cases was a 1 m thick layer held to halite saturation.
strat 'salt'
        t_dep = -23.8 m.y.
        thickness = 1 m
        X(ss) = 90%; X(sh) = 10%
strat 'Miocene'                 # Description of a unit of sediment.
        t_dep = -7.12 m.y.      # Age of the top of sediment unit from the paleodata.
        thickness = 82.776 m    # Thickness of sediment from paleodata.
        X(ss) = 0.488066; X(sh) = 0.511934  # Shale and sand composition from gamma ray log.
strat 'U. Miocene (Messinian)'
        t_dep = -5.32 m.y.
#       thickness = 27.432 m  # Uncorrected thickness of unit from paleodata (not used).
        thickness = 23.5 m      # Thickness of unit corrected to account for geopressuring.
        X(ss) = 0.527719; X(sh) =  0.472281
strat 'L. Pliocene (Zanclian)'
        t_dep = -3.58 m.y.
#       thickness = 27.432 m
```

```
        thickness = 24.5 m
        X(ss) = 0.759390; X(sh) = 0.240610
strat 'Plio-Pleistocene'
        t_dep = -0.2 m.y.
#       thickness = 22.86 m
        thickness = 20 m
        X(ss) = 0.688910; X(sh) = 0.311090
strat 'U. Pleistocene (Ionian)'
        t_dep = -0 m.y.
#       thickness = 874.776 m
        thickness = 840.5 m
        X(ss) =  0.723047; X(sh) = 0.276953
end_strat
surface_temp = 8 C              #From GC185 by MacDonald (2002).
temperature = conductive        #Sets the conductive temperature model.
flow = vertical                 #Description of fluid flow.

#Parameters describing and controlling how salinity propagates:
salinity = full; salt_flux = 0; surface_conc = 0.599 molal; bottom_conc = halite

#Parameters describing what data to output in text format:
tables = depth + concentration + cfc
```

VITA

Miles Alexander McCammon was born in Oakland, California, in September 1986, and is son of James and Joan McCammon. His interest in geology started at an early age, stemming from countless camping trips through the Mojave Desert and sleeping though the $6.7M_w$ Northridge earthquake while living in quake-affected Santa Clarita, California. In June of 2004, he graduated with honors from Colfax High School in Colfax, California, and entered University of California, Los Angeles, as a Regents Scholar that fall. As an undergraduate he worked as a lab assistant in the MegaSIMS lab, and conducted undergraduate research looking at lava thermometry of the Soufrière Volcanic Center, Saint Lucia. He received his Bachelor of Science in Geology from the University of California, Los Angeles, in June 2008. He then studied carbonaceous chondrites as part of the MISIP at ISEI in Japan. He entered graduate school at Louisiana State University in January of 2009.